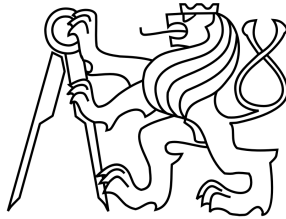


Czech Technical University in Prague
Faculty of Civil Engineering
Department of Mechanics



Master Thesis

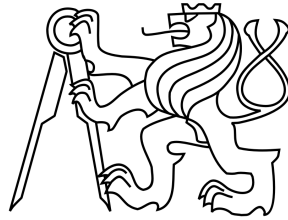
Wang tilings for real world material systems

Supervisor: Ing. Jan Novák, Ph.D.

Prague 2013

Martin Doškář

České vysoké učení technické v Praze
Fakulta stavební
Katedra mechaniky



Diplomová práce

Wangova dláždění pro reálné materiálové systémy

Vedoucí práce: Ing. Jan Novák, Ph.D.

Praha 2013

Martin Doškář



ZADÁNÍ DIPLOMOVÉ PRÁCE

studijní program: Stavební inženýrství
studijní obor: Konstrukce a dopravní stavby
akademický rok: 2013/2014

Jméno a příjmení diplomanta: Martin Doškář
Zadávající katedra: Katedra mechaniky
Vedoucí diplomové práce: Ing. Jan Novák, Ph.D.
Název diplomové práce: Wang tilings for real world material systems
Název diplomové práce
v anglickém jazyce: Wang tilings for real world material systems


Rámcový obsah diplomové práce: Úkolem diplomové práce je studium a aplikace Wangových
dláždění na kompresi mikrostruktur reálných materiálových systémů, implementace souvisejících
algoritmů v programu MATLAB a jejich využití v homogenizačních technikách.

Datum zadání diplomové práce: 18. 9. 2013 Termín odevzdání: 20. 12. 2013
(vyplňte poslední den výuky přísl. semestru)

Diplomovou práci lze zapsat, kromě oboru A, v letním i zimním semestru.

Pokud student neodevzdal diplomovou práci v určeném termínu, tuto skutečnost předem písemně zdůvodnil a omluva byla děkanem uznána, stanoví děkan studentovi náhradní termín odevzdání diplomové práce. Pokud se však student řádně neomluvil nebo omluva nebyla děkanem uznána, může si student zapsat diplomovou práci podruhé. Studentovi, který při opakovaném zápisu diplomovou práci neodevzdal v určeném termínu a tuto skutečnost řádně neomluvil nebo omluva nebyla děkanem uznána, se ukončuje studium podle § 56 zákona o VŠ č.111/1998 (SZŘ ČVUT čl 21, odst. 4).

Diplomant bere na vědomí, že je povinen vypracovat diplomovou práci samostatně, bez cizí pomoci, s výjimkou poskytnutých konzultací. Seznam použité literatury, jiných pramenů a jmen konzultantů je třeba uvést v diplomové práci.


.....
vedoucí diplomové práce


.....
vedoucí katedry

.....
diplomant

Zadání diplomové práce převzal dne: 23.9.2013

Formulář nutno vyhotovit ve 3 výtiscích – 1x katedra, 1x diplomant, 1x studijní odd. (zašle katedra)

Nejpozději do konce 2. týdne výuky v semestru odešle katedra 1 kopii zadání DP na studijní oddělení a provede zápis údajů týkajících se DP do databáze KOS.

DP zadává katedra nejpozději 1. týden semestru, v němž má student DP zapsanou.

(Směrnice děkana pro realizaci stud. programů a SZZ na FSv ČVUT čl. 5, odst. 7)

Abstract

In this thesis, the compression of a material microstructure by means of Wang tilings is investigated. This approach can be understood as an extension to the widely utilized Statistically Equivalent Periodic Unit Cell approach to modelling of heterogeneous materials. Substituting the single cell with multiple tiles allows to reduce the repetitive nature of periodic compressions.

The central idea of the concept of aperiodic tilings along with the smallest set of Wang tiles permitting only the strictly aperiodic tiling is outlined first. This part of the thesis also covers the concept of stochastic tile sets as well as the extension of the tiling concept to three dimensions by means of Wang cubes.

The subsequent part of the thesis is dedicated to the automatic tile morphology design based on the idea of fusing samples of the reference microstructure. Alternative fusion methods to the original Image Quilting algorithm are proposed and their capabilities assessed. With respect to the intended reduction of long-range order artefacts in the reconstructed microstructure a tile patch enhancement is introduced. A considerable part of the thesis is devoted to the sensitivity analysis of the input parameters of the automatic design with respect to the efforts of preserving microstructural information between reference and synthesized microstructures. Its proximity is quantified by means of spatial statistics, namely the two-point probability function and the two-point cluster function, which are both introduced in the first chapter.

The last part of the thesis presents an application of the tiling concept in homogenization procedures. Making use of the sensitivity analysis outputs the microstructure of the Alporas[®] aluminium foam is compressed within a set of Wang tiles. The microstructure is then modelled with a wired mesh consisting of beam elements defined on each tile. Employing the stochastic tiling algorithm allows to produce computational models of arbitrary sizes in a very efficient manner, thereby allowing to quickly investigate bounds to apparent material properties. Two numerical homogenization strategies are employed. The effect of the wired model geometry on the homogenized properties is discussed in order to compare results with other papers.

Keywords

Wang tilings, automatic tile design, microstructure compression and reconstruction, modelling of heterogeneous materials, numerical homogenization, Alporas[®] foam

Abstrakt

Tématem práce je komprese materiálové mikrostruktury založená na konceptu Wangova dláždění. Tuto kompresi lze chápat jako rozšíření způsobu modelování heterogenních materiálů využívajícího statisticky ekvivalentní periodickou buňku. Nahrazení jedné buňky sadou dlaždic umožňuje redukovat periodickou podstatu komprimované reprezentace.

Základní myšlenka aperiodického dláždění spolu s dosud nejmenší množinou Wangových dlaždic dovolující aperiodické dláždění roviny je popsána v první části práce. Zde je také uveden princip stochastického dláždění a jeho rozšíření do třetího rozměru ve formě Wangových krychlí.

Druhá část práce je věnována automatické tvorbě Wangových dlaždic založené na metodách syntézy vzorků referenční mikrostruktury. V rámci práce jsou zkoumány alternativní metody syntézy, jejichž vliv je dále kvantifikován. S ohledem na redukci periodicit je navrženo obohacení sady dlaždic ve formě dodatečné „záplaty“. Podstatnou součástí práce je citlivostní analýza vstupních parametrů automatické tvorby dlaždic, a to s ohledem na zachování výstižnosti komprimované mikrostruktury. Porovnání je založeno na statistických deskriptorech, jmenovitě dvou-bodové pravděpodobnostní funkci a dvou-bodové funkci agregátů, které jsou představeny v první kapitole.

Poslední část práce se věnuje aplikaci konceptu dláždění v homogenizačních úlohách. V rámci práce jsou představeny dvě numerické homogenizační metody vhodné pro diskretizovanou reprezentaci zkoumaného materiálu. S využitím optimálních parametrů získaných z citlivostní analýzy je mikrostruktura Alporas[®] hliníkové pěny komprimována do množiny Wangových dlaždic. Mikrostruktura je pak nahrazena prutovým modelem na úrovni jednotlivých dlaždic. S využitím stochastického dlaždicího algoritmu je pak možné efektivně vytvářet výpočetní domény libovolných velikostí, což umožňuje přesnější studii vhodné velikosti této domény ve smyslu její výstižnosti. Za účelem srovnání s dostupnými zdroji je zkoumán vliv geometrie prutového modelu na výsledné materiálové vlastosti.

Klíčová slova

Wangova dláždění, automatický návrh dlaždic, komprese a rekonstrukce mikrostruktury, modelování heterogenních materiálů, numerická homogenizace, Alporas[®] pěna

Statement of Honor

I hereby declare that all information in this document has been obtained and presented in accordance with academic rules and ethical conduct. I also declare that all sources of information and results which are not original to this thesis are cited and referenced.

Prague, 17th December 2013

Martin Doškář

Acknowledgement

First of all I would like to express my gratitude to my advisor, Ing. Jan Novák, Ph.D., for his advices, encouragement and time he spent with my supervision. My gratitude also belongs to doc. Ing. Jan Zeman, Ph.D., for many helpful suggestions and explanations.

I would also like to thank Ing. Anna Kučerová, Ph.D., for discussions on spatial statistics and my friend Bc. Jan Havelka for many fruitful talks regarding implementation issues and code improvements as well as for providing me with the code for the Lineal-path statistics.

Most importantly, I thank my family for their support and immense patience.

The financial support by the Czech Science Foundation, through the project No. 13–24027S, and the Grant Agency of the Czech Technical University in Prague, grant No. SGS 14/072/OHK1/1T/11, is gratefully acknowledged.

Contents

| | |
|---|-----------|
| Introduction | 1 |
| 1 Microstructure representation | 3 |
| 1.1 Statistical description of microstructure | 4 |
| 1.1.1 Two-point probability function | 5 |
| 1.1.2 Two-point cluster function | 5 |
| 1.1.3 Lineal path function | 7 |
| 1.1.4 Notes on numerical evaluation | 8 |
| 1.1.5 Interpreting higher order descriptors | 11 |
| 2 Wang tilings | 12 |
| 2.1 The concept of Wang Tiles | 12 |
| 2.1.1 Aperiodic Wang tiles sets | 13 |
| 2.1.2 Aperiodic sets of Kari and Culik | 14 |
| 2.1.3 Stochastic Wang tiles sets | 19 |
| 2.2 The concept of Wang Cubes | 20 |
| 3 Tile morphology design | 23 |
| 3.1 Automatic tile morphology design | 23 |
| 3.1.1 Image Quilting algorithm | 24 |
| 3.1.2 Labyrinth algorithm | 26 |
| 3.2 Patched tiles | 27 |
| 3.3 Reducing long-range orientation order artefacts | 28 |
| 3.4 Sensitivity study | 29 |
| 3.4.1 Optimal overlap | 30 |
| 3.4.2 Optimal tile edge length and set diversity | 34 |
| 4 Application of Wang tiling concept to material homogenization | 39 |
| 4.1 A brief introduction to homogenization | 39 |
| 4.2 Homogenization based on the local strain energy | 40 |
| 4.2.1 Strain energy of wired model | 40 |
| 4.2.2 Strain energy of homogeneous isotropic material | 41 |
| 4.2.3 Numerical implementation | 42 |
| 4.3 Homogenization based on the concept of macroscopic degrees of freedom | 43 |
| 4.3.1 Central idea | 43 |
| 4.3.2 Direct Stiffness method | 46 |

| | | |
|----------|---|-----------|
| 4.3.3 | Standard Finite Element method | 49 |
| 4.3.4 | Extracting isotropic elastic parameters | 50 |
| 5 | Homogenization of Alporas[®] closed-cell foam | 53 |
| 5.1 | Alporas [®] foam | 54 |
| 5.2 | Numerical homogenization | 55 |
| 5.3 | Results | 59 |
| 5.4 | Discussion and conclusions | 60 |
| | Summary | 62 |
| | A Isotropic stiffness matrices | a |
| | References | g |
| | List of Symbols | l |
| | List of Figures | n |
| | List of Tables | p |
| | List of Algorithms | q |

Introduction

Continuously improving knowledge on material behaviour walking in line with fast development of computational methods has allowed breathtaking structures to be designed. Designers effort is to create complex structures daring in sense of large dimensions, subtle load-bearing components and irregularity of shapes, all together in order to draw customers' attention. However this is in contradiction with nowadays emphasis on optimizing the production costs and the energy efficiency complying with worldwide race towards reducing the carbon dioxide footprint.

New materials exhibiting supreme thermo-mechanical properties, e.g. ultimate strength, high yield stress, desired Young's modulus or lower conductivity, are thus on demand in order to meet above mentioned socio-economic requirements [1]. From a wide range of possible scenarios composite materials may represent an appealing solution as their behaviour can be controlled by the optimal utilization of constituents' properties in the context of the geometry and applied loads.

Employing optimization techniques in design of material microstructures calls for a suitable model to couple macroscopic properties of a composite with the properties and spatial distribution of constituents. Optimization based on experimental testing of each microstructure realization would be enormously time consuming and expensive. A possible, less expensive, solution rests on mathematical modelling, numerical, analytical or empirical, and physical verification of a favourite composition. This approach is referred to as the Microstructure Sensitive Design [2]. Another related term the Simulation-based Engineering was proposed by The Blue Ribbon Panel on Simulation-Based Engineering Sciences which concluded that *in silico*¹ experimentation is a key factor in engineering and science of the 21st century and that employing simulations in general allows for faster design cycle and ensure the ability of U.S. industry to keep up with world competitors [3]. The later conclusion has a general validity for any country based on industrial society.

Moreover, The Blue Ribbon Panel named multi-scale modelling, i.e. "methods for computing macroscopic phenomena, such as material properties and manufacturing processes, in terms of subscale behaviour", as one of the top challenges that would allow "link models of different scales, such as models of micromechanics or even quantum mechanics to models of macroscale behaviour" [3]. The so called tyranny of scales has been identified as the principle obstacle in current simulation methods incorporating range of scales (both spatial and temporal).

¹in sense of computer aided

The impact of computer aided modelling of various physical phenomena in the multi-scale framework has been also emphasized by the Nobel Committee for Chemistry and the Royal Swedish Academy of Sciences. The 2013 Nobel Prize laureates in Chemistry, Martin Karplus, Michael Levitt and Arieh Warshel, were awarded “for the development of multi-scale models for complex chemical systems” [4]. The distinguished contribution lies in coupling classical physics with quantum mechanics in multi-scale framework. The work of the laureates allows to decompose large systems into three domains with different levels of accuracy governed by different theories: quantum physics at the level of electrons and atomic nuclei, classical physics at the scale of individual atoms and groups of atoms and the theory of dielectric continuum. This allows for modelling of highly complex systems such as biomolecules and is utilized e.g. in drugs development or solar cells designs [4, 5].

To place the topic of the present thesis in the context of aforementioned statements, incorporating a knowledge of underlying material microstructure into standard finite element analyses is of great interest. Widely utilized approach rests on the concept of Statistically Equivalent Periodic Unit Cell (SEPUC) [6], in which SEPUC of underlying microstructure represents an integration point in upper scale model. This approach is often called FE² method.

The tiling concept can be understood as an extension of the SEPUC approach. It has been proved that incorporating Wang tiles to compression of microstructures leads to substantial reduction of long-range order artefacts of reconstructed media, thereby overcoming the periodic nature of SEPUC [7]. Despite the fact that the tiling concept in this work is used only for compressing and reconstructing the microstructure, it may be utilized for the assembly of complex, microstructure-informed, enrichment functions in the Generalized Finite Element Methods [8]. Thus, the tiling approach can contribute to overcome the tyranny of scales.

In [7] textures of Wang tiles were designed by means of optimization procedures. In this work the automatic design of Wang tiles presented by Cohen [9] is investigated with respect to long range order artefacts. An idea of tile patch as [10] is implemented and its impact on the magnitude of long range order artefacts is reviewed. The original automatic design employs the Image Quilting Algorithm [11], which is very efficient but certain limitations. Therefore modifications of this algorithm are examined. As the automatic design inputs are numerous, a sensitivity analysis of those inputs with respect to microstructure descriptors is performed.

The present master thesis builds on the topic of the author’s bachelor thesis. In order to keep the exposition self-contained, some parts of the bachelor thesis are reintroduced and extended. The work is structured as follows. The first chapter discusses the question of microstructure representation and introduces descriptors for its quantification purposes. In the second chapter, the main idea of Wang tiling is presented. A construction of the smallest aperiodic sets of Wang tiles that has been discovered to this time is described in detail along with the stochastic non-periodic tiling. Chapter 3 covers the topic of tile morphology with emphasis on its automatic design. The fourth chapter introduces two homogenization strategies, that are then employed within the topics of chapter 5, in which the concept of tiling is applied to homogenization of elastic properties of Alporas[®] aluminium foam.

Chapter 1

Microstructure representation

Homogenization methods based on numerical modelling require a suitable computational model that captures the whole microstructural information. The existence of such a model is determined by the ergodicity of a medium under investigation.

Ergodic hypothesis. Assume a set \mathbb{A} of microstructure samples α with a probability of occurrence $p(\alpha)$ each occupying a domain Ω_α . Define the ensemble average $\overline{F(\mathbf{x})}$ of quantity $F(\mathbf{x}, \alpha)$ as

$$\overline{F(\mathbf{x})} = \int_{\mathbb{A}} F(\mathbf{x}, \alpha) p(\alpha) d\alpha \quad (1.1)$$

and the spatial average $\langle F(\mathbf{x}, \alpha) \rangle$ over a single media sample α

$$\langle F(\mathbf{x}, \alpha) \rangle = \frac{1}{|\Omega_\alpha|} \int_{\Omega_\alpha} F(\mathbf{x} + \mathbf{y}, \alpha) d\mathbf{y}. \quad (1.2)$$

Ergodic hypothesis assumes that the spatial average is independent of a choice of the representation α and is equal to the ensemble average $\overline{F(\mathbf{x})}$, i.e.

$$\overline{F(\mathbf{x})} = \langle F(\mathbf{x}, \alpha) \rangle, \quad \text{for } \forall \alpha \in \mathbb{A}, \quad (1.3)$$

if $|\Omega_\alpha| \rightarrow \infty$.

It has been shown [1] that in the case of a periodic medium the infinite domain can be substituted with a periodic part of the domain. For a generally non-periodic media the relation (1.3) may hold if the sample domain Ω_α is large enough to be representative in the sense of desired quantity $F(\mathbf{x}, \alpha)$ [1]. From this point onwards the microstructure is regarded ergodic.

Representative volume element. The notion of the Representative Volume Element (RVE) has been introduced to address the question of representativeness of a computational model/domain. Various definitions of the RVE exist, an overview of these definitions can be found in [6, 12]. In general, the RVE is such a domain whose apparent properties equal to the effective properties of a microstructure with

a defined precision. On the one hand the RVE has to be large enough to incorporate the whole variety of microstructure, on the other hand it has to be small enough to represent a material point in continuum mechanics, upper scale model [13]. The latter yields the condition of the clear separation of scales, necessary in multi-scale modelling approach.

The size of the RVE depends mainly on the distribution of constituents volume fraction, phase properties contrast, and on the phenomenon that is concerned. In other words, for the same microstructure the size of the RVE does not need to be the same for e.g. thermal conductivity and linear elasticity [13, 14, 15]. Especially in the case of the infinite contrast of phases properties the size of the RVE can easily become computationally infeasible [14].

To overcome this, a concept of the Statistical Volume Elements (SVEs) was proposed in [15]. Instead of considering a single RVE, a set of smaller samples is assumed and the effective property is obtained as an average over the set of these [2, 13, 15], recall (1.1). Another advantage of this approach is that calculations can be easily distributed among computational nodes and parallelized.

The concepts of the RVE and SVEs are always related to physical response of the microstructure. On the contrary, the presented Wang tiling approach involves only the spatial distribution of constituents, however, allows to efficiently produce RVEs of arbitrary size. So once the microstructure is compressed within the set of Wang tiles, analysis of the optimal size of the RVE can be easily performed for an arbitrary phenomenon. If the size of the RVE turns out to be too large anyway, the tiling approach can produce a set of the SVEs as well.

1.1 Statistical description of microstructure

The interior of Wang tiles is designed to morphologically resemble the reference microstructure. To achieve this task methods to quantify the microstructure morphology has to be introduced. The most common family of statistical descriptors is represented by correlation functions. Those can be further divided into auto-correlation and cross-correlation functions depending whether the correlation is determined for the same or different phases [2].

Define characteristic function $\chi_i(\mathbf{x})$ of the i -th phase as

$$\chi_i(\mathbf{x}) = \begin{cases} 1, & \text{for } \mathbf{x} \in \mathcal{D}_i, \\ 0, & \text{otherwise,} \end{cases} \quad (1.4)$$

where \mathcal{D}_i denotes a portion of domain Ω occupied with the i -th phase.

A definition of the general n -point probability function reads [6, 16]

$$S_{r_1, r_2, \dots, r_n}(\mathbf{x}_1, \mathbf{x}_2, \dots, \mathbf{x}_n) = \frac{1}{|\Omega|} \int_{\Omega} \prod_{i=1}^n \chi_{r_i}(\mathbf{x}_i) d\Omega. \quad (1.5)$$

The microstructure can be determinately described only if the infinite number of the n -point probability function is assumed [17]. Nevertheless, incorporating only

Table 1.1: Relation among two-point correlation function for binary media [6]

| | $S_{ii}(\mathbf{x})$ | $S_{ij}(\mathbf{x})$ | $S_{jj}(\mathbf{x})$ |
|----------------------|--|-------------------------------|--|
| $S_{ii}(\mathbf{x})$ | $S_{ii}(\mathbf{x})$ | $\phi_i - S_{ij}(\mathbf{x})$ | $\phi_i - \phi_j + S_{jj}(\mathbf{x})$ |
| $S_{ij}(\mathbf{x})$ | $\phi_i - S_{ii}(\mathbf{x})$ | $S_{ij}(\mathbf{x})$ | $\phi_j - S_{jj}(\mathbf{x})$ |
| $S_{jj}(\mathbf{x})$ | $\phi_j - \phi_i + S_{ii}(\mathbf{x})$ | $\phi_j - S_{ij}(\mathbf{x})$ | $S_{jj}(\mathbf{x})$ |

a limited set of those functions still yields very good results [18]. The most frequently utilized spatial descriptors are presented in this chapter.

1.1.1 Two-point probability function

As the investigated microstructure is assumed to be ergodic, the first order correlation function (i.e. $n = 1$) of a phase is a constant function and equals the volume fraction of the phase. Computing high-order n -point probability functions is not only cumbersome but it is also hard to visualize it and interpret [2], see Fig. 1.1. Therefore the most common descriptor is the two-point probability function.

If the assumption of homogeneous material is accepted, the expression (1.5) can be further simplified to

$$S_{ij}(\mathbf{x}_1, \mathbf{x}_2) = S_{ij}(\mathbf{x}_1 - \mathbf{x}_2) = S_{ij}(\mathbf{x}) = \frac{1}{|\Omega|} \int_{\Omega} \chi_i(\mathbf{y}) \chi_j(\mathbf{x} + \mathbf{y}) d\mathbf{y}. \quad (1.6)$$

In the case of a two-phase media with phases i and j and corresponding volume fractions ϕ_i and ϕ_j , respectively, a relation between the auto-correlation functions regarding each phase and the cross-correlation function is summarized in Tab. 1.1, see e.g. [6]. Because of the existence of these deterministic relations the auto-correlation and two-point probability functions are considered identical and denoted as $S_2(\mathbf{x})$.

Since $S_2(\mathbf{x})$ function may be qualified as giving the probability of finding two points at distance \mathbf{x} in the same phase. If $|\mathbf{x}| \rightarrow 0$ the two-point probability function degenerates to one-point probability function, hence it gives the phase volume fraction ϕ . If $|\mathbf{x}| \rightarrow \infty$ the states of the two points become uncorrelated and the value of $S_2(\mathbf{x})$ approaches ϕ^2 . The latter allows to define a coherence (also called correlation) length r_c as a characteristic of the material [2]

$$S_2(|\mathbf{x}| \geq r_c) \approx \phi^2. \quad (1.7)$$

1.1.2 Two-point cluster function

Previously introduced $S_2(\mathbf{x})$ function gives an appreciation of the long-range spatial distribution of phases, nevertheless it does not include information of inclusion clustering. As the connectivity of clusters has a great influence on properties such as conductivity or elastic stiffness [16], a statistics that would describe clustering is required.

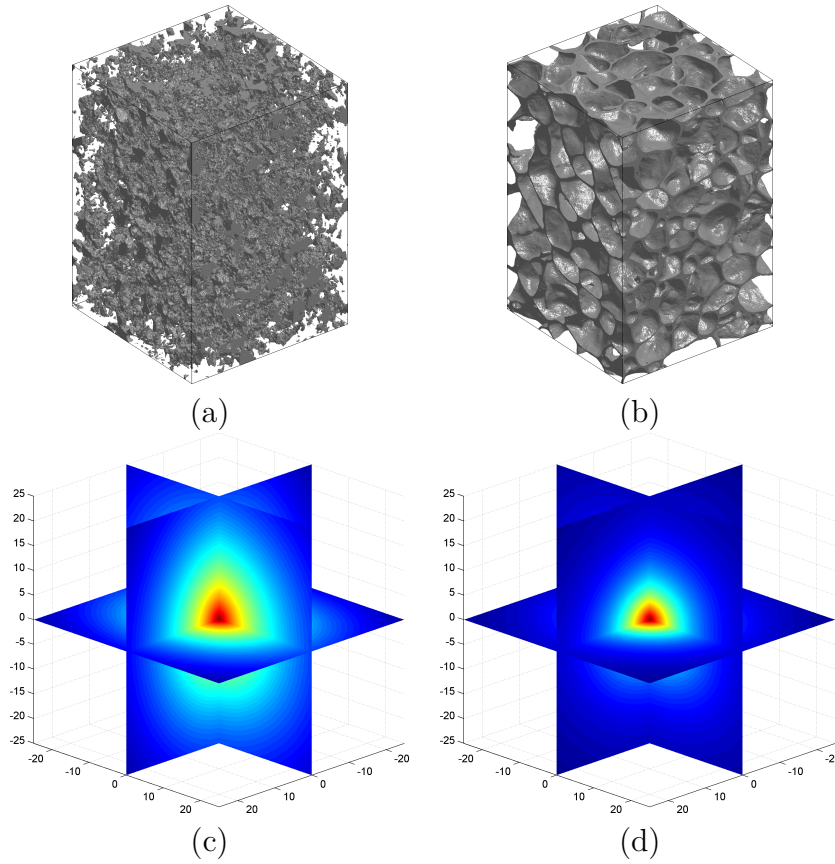


Figure 1.1: Visualization of raw micro CT-scan data and corresponding $S_2(\mathbf{x})$ statistics: (a) Sandstone pores, with courtesy of Adnan Sufian and Adrian R. Russel [19], (b) Alporas[®] foam with courtesy of Ondřej Jiroušek [20]

Torquato [16] defines a cluster as “a part of phase i which can be reached from a point in phase i without passing through phase j ”. Hence the domain of the i -th phase D_i can be decomposed into a disjoint set of n clusters $d_i^{(k)}$,

$$D_i = \bigcup_{k=1}^n d_i^{(k)}. \quad (1.8)$$

By analogy to (1.4), a cluster characteristic function can be defined as

$$\chi_i^{(k)}(\mathbf{x}) = \begin{cases} 1, & \text{for } \mathbf{x} \in d_i^{(k)}, \\ 0, & \text{otherwise.} \end{cases} \quad (1.9)$$

The expression for the two-point cluster function $C_{ii}(\mathbf{x})$ then reads as

$$C_{ii}(\mathbf{x}) = \frac{1}{n} \sum_{k=1}^n \frac{1}{|\Omega|} \int_{\Omega} \chi_i^{(k)}(\mathbf{y}) \chi_i^{(k)}(\mathbf{x} + \mathbf{y}) d\mathbf{y}. \quad (1.10)$$

Author is not aware of any universal relation between the $C_{ii}(\mathbf{x})$ functions for different phases as exists in the case of the $S_{ii}(\mathbf{x})$. Obviously no cross-correlation

cluster function can be defined, moreover in the case of two-phase medium with inclusions embedded in the matrix, two-point cluster function of the matrix phase matches $S_2(\mathbf{x})$ function of the matrix. Therefore if not stated otherwise, the two-point cluster function is assumed to be a function of the inclusion phase and is denoted $C_2(\mathbf{x})$.

The two-point cluster function $C_2(\mathbf{x})$ can be understood as a special case of $S_2(\mathbf{x})$ function as it gives the probability of finding the two points at distance \mathbf{x} not only in the same phase but also in the same cluster of that phase. $C_2(\mathbf{x})$ is thus a short-range order statistics that describes shapes of inclusions rather than their distribution within a domain. The superior nature of the $C_2(\mathbf{x})$ function when applied in microstructure reconstruction algorithms (especially when combined with $S_2(\mathbf{x})$) was reported e.g. in [18].

The limit case $|\mathbf{x}| \rightarrow 0$ of the $C_{ii}(\mathbf{x})$ yields the same result as for the $S_2(\mathbf{x})$ due to the definition (1.9). The reciprocal limit case $|\mathbf{x}| \rightarrow \infty$ is not unambiguous and depends on the nature of the composite (e.g. percolation properties). For the matrix phase, if distinguished, the infinity limit is of the same value as for the $S_2(\mathbf{x})$. On the other hand for the inclusion phase $C_2(|\mathbf{x}| \rightarrow \infty) = 0$.

Complementary to $C_2(\mathbf{x})$ a blocking function $B_2(\mathbf{x})$ giving the probability of the two points being in different clusters can be introduced with relation [16]

$$S_2(\mathbf{x}) = C_2(\mathbf{x}) + B_2(\mathbf{x}). \quad (1.11)$$

Note that to capture the connectedness of a cluster, investigating a planar cross-section through the material is not sufficient as the in-plane separated clusters can be connected in out of plane directions [21]. A complete three dimensional analysis is thus needed. However, C_2 function of a planar domain still provides meaningful description of inclusions shapes.

1.1.3 Lineal path function

Another information of the microstructure spatial composition can be revealed if the condition imposed formerly on the end points \mathbf{x}_1 and \mathbf{x}_2 is expanded on the whole line segment defined by the vector $(\mathbf{x}_2 - \mathbf{x}_1)$.

The lineal path characteristic function χ_i^L yields

$$\chi_i^L(\mathbf{x}_1, \mathbf{x}_2) = \begin{cases} 1, & \text{for } (\mathbf{x}_2 - \mathbf{x}_1) \subset \mathcal{D}_i, \\ 0, & \text{otherwise.} \end{cases} \quad (1.12)$$

The quantity describing the probability of finding a randomly thrown straight segment of a length $|\mathbf{x}|$ in the domain portion \mathcal{D}_i is called the lineal path function $L_2(\mathbf{x})$ [21] and for isotropic media can be calculated as

$$L_2(\mathbf{x}) = \frac{1}{|\Omega|} \int_{\Omega} \chi_i^L(\mathbf{y}, \mathbf{y} + \mathbf{x}) d\mathbf{y}. \quad (1.13)$$

1.1.4 Notes on numerical evaluation

Evaluation of the aforementioned spatial statistics is usually based on the digital discretization of material microstructures obtained by various displaying methods, image scanning, microtomography [19, 20] or backscattered electron imaging to name a few.

By making use of the convolution character of $S_2(\mathbf{x})$ function (1.6) the Fourier transform can be employed [6]. Then

$$S_2(\mathbf{x}) = \mathcal{F}_n^{-1} (\mathcal{F}_n(\chi_i(\mathbf{x}))\mathcal{F}_n^*(\chi_i(\mathbf{x}))) , \quad (1.14)$$

where \mathcal{F}_n denotes n-dimensional Fourier transform (incorporated in Matlab environment as the *fft*n function), \mathcal{F}_n^{-1} its inverse and * stands for complex conjugate.

The lineal path function $L_2(\mathbf{x})$ (1.12), however, does not exhibit the convolution nature. Its computation is thus cumbersome. The computation can be profitably distributed among GP- Graphic Processor units utilizing the CUDA programming library so as to maximally reduce computational overhead [22].

In order to compute $C_2(\mathbf{x})$ function, an algorithm that identifies inclusions is required. The Image Processing Toolbox function *bwconncomp* included in Matlab environment, that finds connected components, can be applied [23]. However, since more flexible version of $C_2(\mathbf{x})$ computation that allows for a quick update was desired for the optimization purposes, a procedure based on flood-fill algorithm (also utilized in *bwconncomp* function) was programmed, see Algorithm 1.1.

The algorithm scans the binary image and assigns pixels (i, j) that belong to \mathcal{D}_i to clusters $d_i^{(k)}$, recall Eq. (1.8). When an unsigned pixel (i, j) , i.e. a pixel that does not belong to any previously defined clusters $d_i^{(j)}, \forall j \leq k$, is found, a new cluster $d_i^{(k+1)}$ is defined and the (i, j) pixel is attributed to it. The four-pixel neighbourhood of the (i, j) pixel is then searched through and a set \mathcal{S} of yet unsigned pixels (a, b) is defined. All pixels from \mathcal{S} are attributed to the latter cluster $d_i^{(k+1)}$ and a new set \mathcal{S}_n of unique pixels from the four-pixel neighbourhood of $\forall (a, b) \in \mathcal{S}$ is determined, this process is repeated until an empty set \mathcal{S}_n is reached, which means that the whole cluster $d_i^{(k+1)}$ has been identified. The algorithm then scans for another unsigned pixel (i, j) until all the pixels are attributed to clusters.

Once all the inclusions are identified, individual $S_2(\mathbf{x})$ functions are calculated for separate inclusions of the given phase and $C_2(\mathbf{x})$ is determined as their mean values.

In the case of swapping states of two pixels in an optimization proceduress, e.g. simulated annealing [22], there is no need to search for all inclusions again, it is enough to check the connectivity around the changed pixel and recalculate $S_2(\mathbf{x})$ only for the affected inclusions [16].

For the microstructure comparison purposes all the descriptors but $L_2(\mathbf{x})$ were implemented into a Matlab program. The program has its own graphic user interface, Fig. 1.4, and exploits the Image Processing Toolbox of Matlab environment, namely *regionprops* function computing various measures of each identified inclusion. It allows to import microstructure images, convert them into binary media with prescribed thresholds, clear incidental image faults, calculate scalar spatial

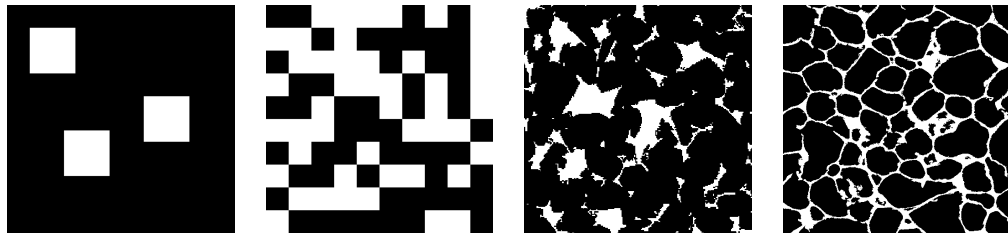


Figure 1.2: Reference microstructures

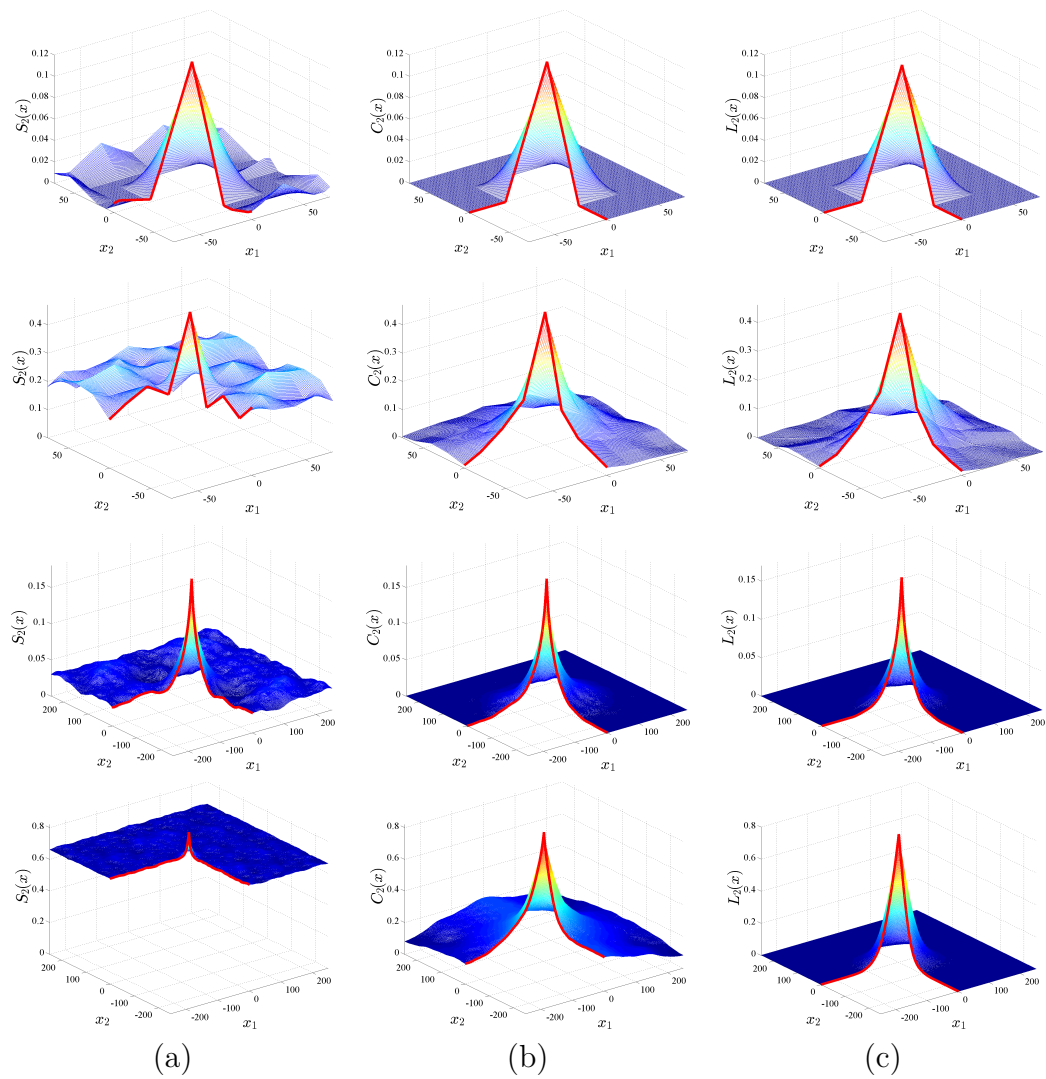


Figure 1.3: Spatial statistics of the reference microstructures from Fig. 1.2 : (a) $S_2(\mathbf{x})$, (b) $C_2(\mathbf{x})$, (c) $L_2(\mathbf{x})$

Algorithm 1.1 Flood-fill algorithm

```

 $k \leftarrow 0$ 
for  $\forall (i, j) \in \mathcal{D}_i$  do
  if  $(i, j) \notin d_i^{(k)}, \forall j \leq k \vee (i, j) \in \mathcal{D}_i$  then
     $k \leftarrow k + 1$ 
     $d_i^{(k)} \leftarrow \{(i, j)\}$ 
     $\mathcal{S} = \{(a, b); |(a, b) - (i, j)| \leq 1 \vee (a, b) \notin d_i^{(j)}, \forall j \leq k \vee (a, b) \in \mathcal{D}_i\}$ 
    while  $\mathcal{S} \neq \emptyset$  do
       $\mathcal{S}_n \leftarrow \emptyset$ 
       $d_i^{(k)} \leftarrow d_i^{(k)} \cup \mathcal{S}$ 
      for  $\forall (a, b) \in \mathcal{S}$  do
         $\mathcal{S}^\ell \leftarrow \{(c, d); |(c, d) - (a, b)| \leq 1 \vee (c, d) \notin d_i^{(j)}, \forall j \leq k \vee (c, d) \in \mathcal{D}_i\}$ 
         $\mathcal{S}_n \leftarrow \mathcal{S}_n \cup (\mathcal{S}^\ell - (\mathcal{S}_n \cap \mathcal{S}^\ell))$ 
      end for
       $\mathcal{S} \leftarrow \mathcal{S}_n$ 
    end while
  end if
end for

```

statistics (such as the volume fraction, mean area of inclusions, equivalent diameter etc.) and higher order descriptors. The outputs are both ASCII and graphical.

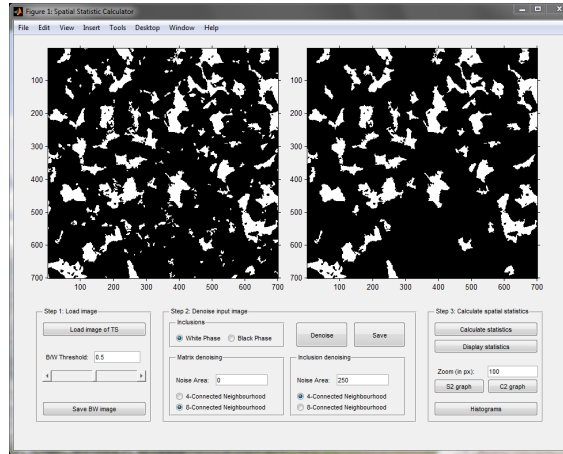


Figure 1.4: Matlab GUI program for spatial statistics computations

1.1.5 Interpreting higher order descriptors

Illustrative examples of the previously introduced microstructure descriptors are shown in Fig. 1.3.

The information stored within each particular descriptor comes from definitions made in the previous section. However some information is more visible if the descriptors are compared as in the following list.

- For a phase, $C_2(\mathbf{x})$ function converges to $S_2(\mathbf{x})$ if the microstructure specimen is fully percolated by this phase.
- As mentioned, $C_2(\mathbf{x})$ approaches $S_2(\mathbf{x})$ for the matrix phase of particulate media, on the other hand $L_2(\mathbf{x})$ function may still involve a short-range information of the matrix composition, namely, in a short-range inter-inclusion zones.
- The difference between $S_2(\mathbf{x})$ and $C_2(\mathbf{x})$ may indicate how densely inclusions are gathered, Fig. 1.5.
- In the case of convex inclusions $C_2(\mathbf{x})$ and $L_2(\mathbf{x})$ are the same, thus a difference between the two functions indicates a level of convexity.

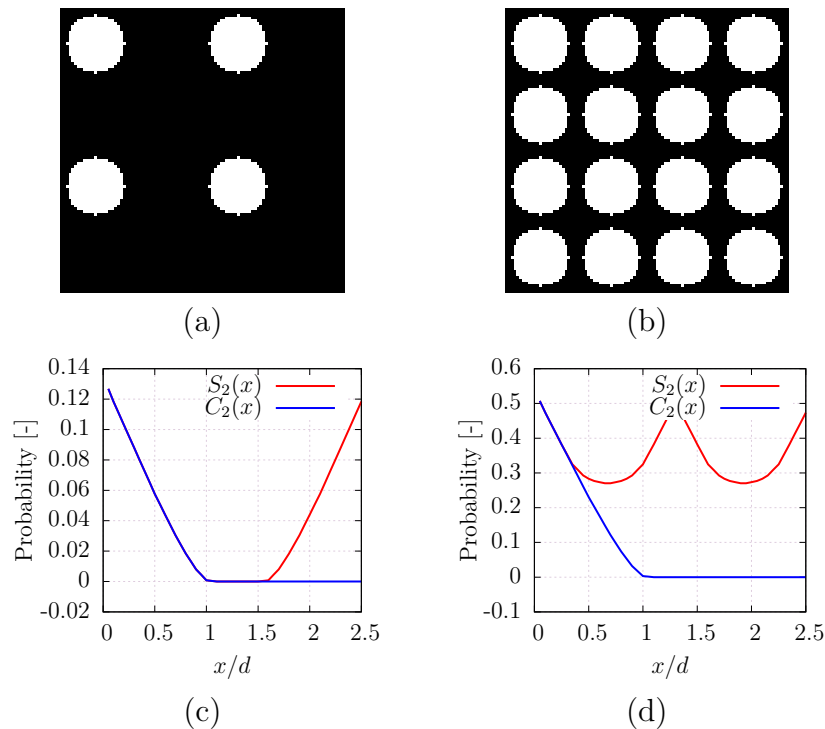


Figure 1.5: Comparison of $S_2(\mathbf{x})$ and $C_2(\mathbf{x})$ graphs for (a) loosely and (b) densely packed inclusions

Chapter 2

Wang tilings

A tiling has been present since the first human dwellings that were supposed not only to shelter against the climate appeared. The main purpose of tiling was to please the aesthetic feelings. e.g. ancient mosaics, decorative pavements or wall ornaments. In the course of time the patterns and shapes have become more sophisticated, however periodic patterns have prevailed [24].

Historically tiling were in the focus of artists and architects. The first documented mathematical research on tiling is attributed to Johannes Kepler and his book *Harmonice Mundi* [24]. A comprehensive survey on tiling and the mathematical background can be found in classical reference [24] by Grünbaum and Shephard. Since the nineties of the 20th century the interest in tiling, especially in aperiodic tiling, has increased as the possible application in physics - namely crystallography [25, 26], and biology - modelling of DNA assembly [27, 28], emerged.

The focus of this chapter is limited to the tiling made of Wang Tiles. Their practical application first appeared in Computer Graphics [9, 29]. The main feature that makes it attractive is its ability to produce non-periodic naturally looking textures at a low computational and storage cost. From the perspective of Materials Engineering the appealing features are similar to those of Computer Graphics, the efficient way of generating microstructured domains of arbitrary sizes [7]. Moreover, an application of the tiling concept in Generalized Finite Elements Method has been also proposed [8].

2.1 The concept of Wang Tiles

The idea of Wang tiles is related to the Entscheidungs problem proposed by David Hilbert, which poses a challenge of proving any mathematical statement with fundamental axioms of logic, i.e. looking for a general algorithm that can decide whether the statement is valid or not [30]. The capability of a general computing machine to model any algorithmizable problem was revealed by Alan Turing in [31, 32]. He associated the Entscheidungs problem with the question whether a general Turing machine with rules corresponding to the axioms and the investigated statement will eventually stop or will compute infinitely long. He called this

the Halting problem. He proved that there is no general solution to this question and hence a specific machine cannot be decided to halt or run forever.

The contribution of Hao Wang, whom the Wang tiles are named in honor of, lies in further relating the Halting problem to the Domino problem, a task to decide whether the given set of square tetraminoe-like tiles with codes assigned to the tiles edges can tile the infinite plane while matching codes on adjacent edges. He showed that any Turing machine can be turned into the set of specific tiles and therefore there is no general procedure that can decide if the given set is capable of tiling the infinite plane [33]. Still he showed that certain statements of the AEA¹ class of logic statements, that can be directly converted into the domino problem, can be advantageously proved by means of the solution of infinite tiling [34].

Wang based proving the AEA problem on a fundamental conjecture that if the infinite plane is to be tiled then it has to be tiled periodically, therefore a periodic part of the plane must exist. But he was aware that the conjecture had not been proven, he stated that if the conjecture is wrong, the procedure is only semi decisive proof, i.e. it cannot serve as a disproof.

2.1.1 Aperiodic Wang tiles sets

The Wang's fundamental conjecture that only the periodic tiling allows for an infinite tiled plane was disapproved by Wang's student Robert Berger, who in [35] published a set containing 20 426 tiles that is capable of tiling infinite domain strictly aperiodically. He reduced the necessary number of distinct tiles to 104 in his thesis. The design of these sets was based on superimposing different periodic tilings one over each other. In the same manner Knuth redesigned the Berger's 104 set reducing it to 92 tiles. Another attempts to reduce the number of tiles continued with Läuchi's 40 tiles (1966, unpublished till 1975), Robinson's set of 52 tiles (1967) and 32 tiles (1971), see [24] and references therein for further details.

Meanwhile, Robert Penrose realized that his kite and dart aperiodic tiling can be converted to a Wang tiling. He recognized that polygons appearing in his tiling can be transformed into squares in a regular grid, which resulted in a set containing 34 tiles. Another refinement was done in cooperation with Robinson, they found out that 32 tiles out of the former 34 were enough to tile the plane aperiodically. Gröbbaum and Shephard pointed out that originating with the Penrose rhombs instead of the Penrose kites and darts would have resulted in the set of 24 tiles. In 1997 Robinson realized another possible transition, from in that time known aperiodic tiling of the non-square Amman prototiles introduced by Robert Amman [36], to 32 Wang tiles. Robert Amman himself came up with an idea to combine the Amman bars with his prototiles leading to 16 tiles.

In 1997 Jarrko Kari came with an utterly different approach to designing aperiodic Wang tiles sets. He noticed the affinity of the Mealy machine [37] and the Wang tiles. On the basis of this observation he designed a set of 14 tiles as a sequential machine that multiplies a balanced representation of a real number by a certain

¹Statements that contain two universal \forall and one existential \exists quantifiers.

rational number. Following his idea Karel Čulík managed to reduced the set to 13 tiles with additional trick [38].

The author is not aware of smaller aperiodic set of Wang tiles. Kari and Culik in [39] proposed that only 12 tiles from the original set of 13 may be able to tile the whole plane aperiodically, but confess that with the computational power of that time it was not possible to prove their preliminary conjectures. In 2012 Demain et al. [40] presented a single polygonal tile that can substitute any tile set and model of any Turing machine. However, the tile is allowed to rotate and reflect and tiles the domain with small gaps in the tiling, which does not suit the Materials Engineering applications.

2.1.2 Aperiodic sets of Kari and Culik

The aperiodic tile sets of Kari and Culik are discussed in this section. The section summarizes outcomes of Kari and Culik presented in [41, 38, 39].

Let assume a tile set T and a tiling as the mapping $f : \mathbb{Z}^2 \rightarrow T$. The tiling is called periodic iff $\exists(\vartheta, \zeta) \in \mathbb{Z}^2 \setminus \{(0, 0)\}; f(x + \vartheta, y + \zeta) = f(x, y); \forall(x, y) \in \mathbb{Z}^2$. Moreover, Kari stated in [41] that if the tiling consisting of tiles from T is periodic with period (ϑ, ζ) , then it is also doubly periodic with periods $(\vartheta, 0)$ and $(0, \zeta)$, i.e. $f(x, y) = f(x + \vartheta, y) = f(x, y + \zeta)$. The tile set T is called aperiodic iff (i) it can produce valid tilings and (ii) none of these valid tilings is periodic.

Beatty sequence. Define $\lfloor \alpha \rfloor$ as the integer part of an arbitrary real number α . Beatty sequence $A(\alpha)$ [42, 43] is thus a sequence of $A(\alpha)_i$'s defined as

$$A(\alpha)_i = \lfloor i \cdot \alpha \rfloor, \quad \forall i \in \mathbb{Z}. \quad (2.1)$$

Alternatively, the Beatty sequence $A(\alpha)$ of any arbitrary real number α is a sequence of $i\alpha$'s rounded towards the nearest lower integer. An illustrative example can be

$$A(2.25)_{i=1\dots 5} = \{2, 4, 6, 9, 11\}.$$

Balanced representation. Balanced representation $B(\alpha)$ of any real number α is defined as the sequence of differences between two consecutive members of the Beatty sequence [41],

$$B(\alpha)_i = A(\alpha)_i - A(\alpha)_{i-1}. \quad (2.2)$$

Note that if $\alpha \notin \mathbb{Z}$ the balanced representation $B(\alpha)$ contains only integers k and $k+1$ such that $k < \alpha < k+1$ and obviously $B(\alpha)_i = \alpha$ for $\forall i \in \mathbb{Z}$ iff $\alpha \in \mathbb{Z}$. Also note that the arithmetic average of n consecutive members of $B(\alpha)$ does not differ from α more then by one and approaches the value of α with $n \rightarrow \infty$ [41, 38]. Moreover balanced representation of a rational number $\alpha \in \mathbb{Q}$ is a bi-infinite² periodic sequence [39], see example

$$B(2.25) = \dots 2, 2, 2, 3, 2, 2, 2, 3 \dots$$

²From any element of the sequence, there is a finite sequence to the left and to the right from this element.

Mealy machine. A Mealy machine is a concept of sequential machine from the theory of computation introduced by Mealy in [37] that denotes a deterministic finite-state automaton with defined initial and final state. The output of each iteration of the machine is determined by the state of the machine at the beginning of each iteration and by the input symbol (or symbols).

Since the tiling is assumed to be bi-infinite, no initial and final states are to be defined hence the Mealy machine M without initial and final state is a 4-tuple³ $M = (K, \Sigma, \Delta, \gamma)$, where K is the finite set of states, Σ is the set of admissible inputs, Δ is the set of admissible outputs, and γ contains transitions between the states from K . The transitions $(s, a, t, b) \in \gamma$ are such that $s, t \in K$, $a \in \Sigma$ and $b \in \Delta$ [39]. Sequential machine can be visualized by a labelled directed graph with initial and final state nodes and transitions as in Fig. 2.1 (a).

We say that a two bi-infinite sequences x and y are in relation defined with the Mealy machine M if $x_i \in \Sigma$, $y_i \in \Delta$ and $(s_{i-1}, x_i, s_i, y_i) \in \gamma$ for $\forall i \in \mathbb{Z}$.

Kari [41] constructed the sequential machine M so that it represents multiplication of balanced representation of α by a rational number $q = \frac{n}{m}$; $m \in \mathbb{Z} \setminus 0$; $n \in \mathbb{Z}$. It means that input and output codes Σ and Δ , respectively, contain integers of $B(\alpha)$ and $B(q\alpha)$ and the states K are defined as

$$K = \{q\lfloor i\alpha \rfloor - \lfloor qi\alpha \rfloor\}, \quad \forall i \in \mathbb{Z}. \quad (2.3)$$

Since the following inequality holds for an arbitrary real number r (and therefore also for $r = i\alpha$)

$$q\lfloor r \rfloor - 1 \leq qr - 1 < \lfloor qr \rfloor \leq qr < q(\lfloor r \rfloor + 1), \quad (2.4)$$

the bounds on values of states K yields

$$-q < \underbrace{q\lfloor r \rfloor - \lfloor qr \rfloor}_K < 1. \quad (2.5)$$

As the difference $q\lfloor r \rfloor - \lfloor qr \rfloor$ is always an integer multiple of $\frac{1}{m}$ the states of the sequential machine M are

$$K = \left\{ -\frac{n-1}{m}, -\frac{n-2}{m}, \dots, \frac{m-2}{m}, \frac{m-1}{m} \right\}. \quad (2.6)$$

Relation between tile set and sequential machine. Each tile from the set represents a single transition from γ of the Mealy machine M_q . Codes on vertical edges of tiles represent states K , horizontal codes denote input letters and output letters⁴ which belong to Σ and Δ , respectively. The machine should also be bi-infinite in order to cover up the infinite two dimensional domain, hence $\Sigma = \Delta$ ⁵.

³Originally, the initial and the final state are also part of the definition and the Mealy Machine is defined with 6-tuple.

⁴In theory of computation a and b are considered letters of alphabet Σ and Δ

⁵Outputs form one iteration of the machine can be inputs for the next iteration.

The sequential machine M_q is designed to perform multiplication by a rational number q over bi-infinite sequence provided by a balanced representation $B(\alpha)$, thus every tile has a multiplicative character defined as

$$qa + s = b + t, \quad (2.7)$$

where q is constant for all tiles of the given M_q .

To make the tiling structure more explicit, if the tile set is equal to a sequential machine M_q , rows in the tiling correspond to one iteration of M_q . If the tile set consists of more sequential machines, one row always contains tiles only from a subset related to one Mealy machine. Thus the codes on the upper edges represent a sequence $B(\alpha)$ while the codes on the bottom are sequence of $B(q\alpha)$. The vertical edges represent an imbalance between $q\lfloor i\alpha \rfloor$ and $\lfloor q\alpha \rfloor$, see (2.3) and (2.7). This implies that positions of tiles placed in one row are governed by the choice of real number α that defines sequences $B(\alpha)$ and $B(q\alpha)$.

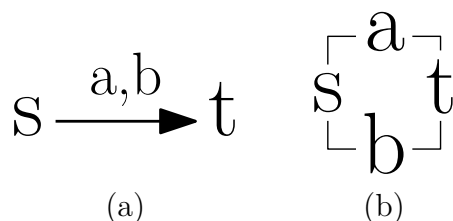


Figure 2.1: Illustration of (a) transition from γ of Mealy machine and (b) corresponding Wang tile

The set of Kari's 14 tiles. Based on the previous knowledge Kari designed his set of tiles as a union of two distinct Mealy machines M_2 and $M_{2/3}$. M_2 operates over $B(\alpha)$ with $\alpha \in [\frac{1}{2}, 1]$ and computes $B(2\alpha)$ with input alphabet $\Sigma_2 = \{0, 1\}$ and output alphabet $\Delta_2 = \{1, 2\}$. $M_{2/3}$ operates over $B(\alpha)$ with $\alpha \in [1, 2]$ and computes $B(\frac{2}{3}\alpha)$ with input alphabet $\Sigma_{2/3} = \{1, 2\}$ and output alphabet $\Delta_{2/3} = \{0, 1, 2\}$ [41]. Thus after the iteration of M_2 at least one but at maximum two iterations of $M_{2/3}$ follow. The illustration of the Mealy machines and the tile set are depicted in Fig. 2.2, the state of value 0 for $M_{2/3}$ is denoted with prime to distinguish it from the state 0 of the machine M_2 .

The set of Culik's 13 tiles. Culik [38] modified the previous set by considering the inverse values of the multipliers (in the case of $M_{2/3}$ he took only the inverse of the denominator of the fraction), i.e. he assumed M_3 and $M_{1/2}$. Moreover he added an additional condition that the $M_{1/2}$ machine can be employed maximally in two following iterations. Therefore, M_3 with $\Sigma_3 = \{0, 1\}$ and $\Delta_3 = \{1, 2\}$ is employed if $\alpha \in [\frac{1}{3}, \frac{2}{3}]$. If $\alpha \in [\frac{2}{3}, 2]$ the $M_{1/2}$ machine is utilized.

The additional conditions on the input and output alphabets has to be imposed in spite of the additional condition. After iteration of the M_3 machine $\alpha \in [1, 2]$ and the output alphabet Δ_3 equals input alphabet $\Sigma_{1/2}^{\alpha \in [1, 2]} = \{1, 2\}$. If $\alpha \in [1, \frac{4}{3}]$

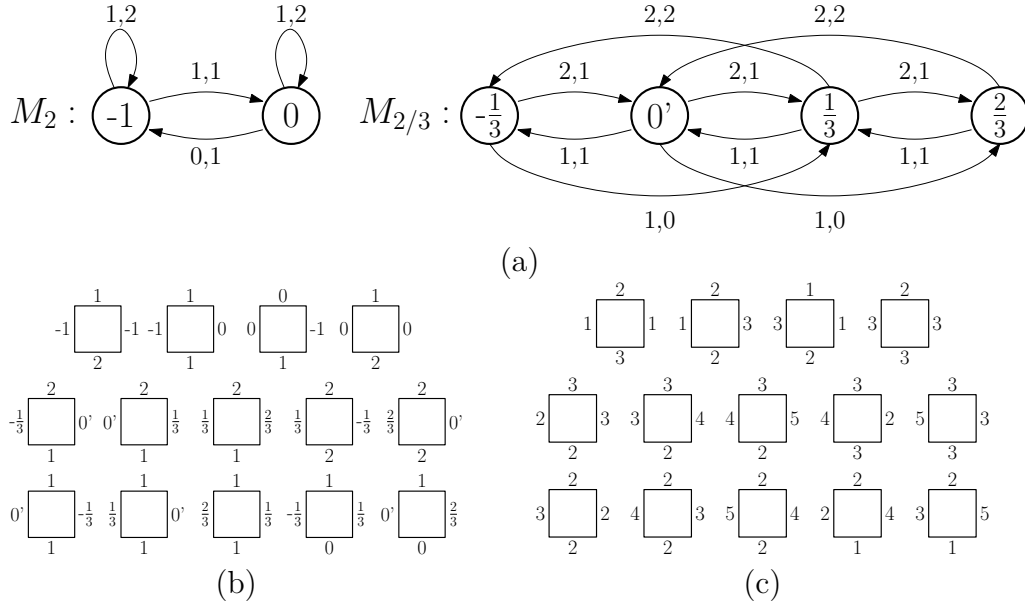


Figure 2.2: Illustration of Kari's set of 14 tiles: (a) Mealy machines, (b) Kari's Wang tiles, (c) indexed tiles (integer edge codes)

only one iteration of $M_{1/2}$ follows and therefore $\Delta_{1/2}^{\alpha \in [1, \frac{4}{3}]} = \{0, 1\}$. If $\alpha \in [\frac{4}{3}, 2]$ an iteration of $M_{1/2}$ machine will be performed twice (after one iteration $\alpha \in [\frac{2}{3}, 1]$) with $\Delta_{1/2}^{\alpha \in [\frac{4}{3}, 2]} = \{0', 1\} = \Sigma_{1/2}^{\alpha \in [\frac{2}{3}, 1]} = \{0, 1\}$ and $\Delta_{1/2}^{\alpha \in [\frac{2}{3}, 1]} = \{0, 1\}$.

The corresponding Mealy machines and Wang tiles are shown in Fig. 2.3.

Proof of validity. The proof of validity of the presented tile sets is straightforward and arises from the nature of Mealy machines that are at the heart of the set design. As the corresponding Mealy machines are bi-infinite and may perform the underlying calculation on bi-infinite sequences, an infinite plane can be tiled with those sets. The first condition can be also expressed as ensuring that the value of α can not get out of the definition range of the united Mealy machines.

Proof of aperiodicity. Recall again the definition of periodicity of a tiling. The tiling is said to be periodic iff $\exists(\vartheta, \zeta) \in \mathbb{Z}^2 \setminus \{(0, 0)\}; f(x + \vartheta, y + \zeta) = f(x, y); \forall(x, y) \in \mathbb{Z}^2$. If the tiling is periodic with period (ϑ, ζ) , it is also periodic with $(\vartheta, 0)$ and $(0, \zeta)$ periods. The nomenclature of the tile edges from Fig. 2.1 (c) is recalled. The left code of the tile at position (i, j) is denoted as $s_{(i,j)}$, the upper code $a_{(i,j)}$, the right code $t_{(i,j)}$ and finally the bottom code $b_{(i,j)}$.

Assume, that the tiling is periodic with period (ϑ, ζ) . Due to the multiplicative nature of tile,

$$qa_{(i,j)} + s_{(i,j)} = b_{(i,j)} + t_{(i,j)}, \quad (2.8)$$

and the condition on congruent edges, i.e. $t_{(i,j)} = s_{(i+1,j)}$, along with the fact that only tiles with the same q are present in a row give rise to the relation between the sum of the values on the upper edges and the sum of the bottom codes' values

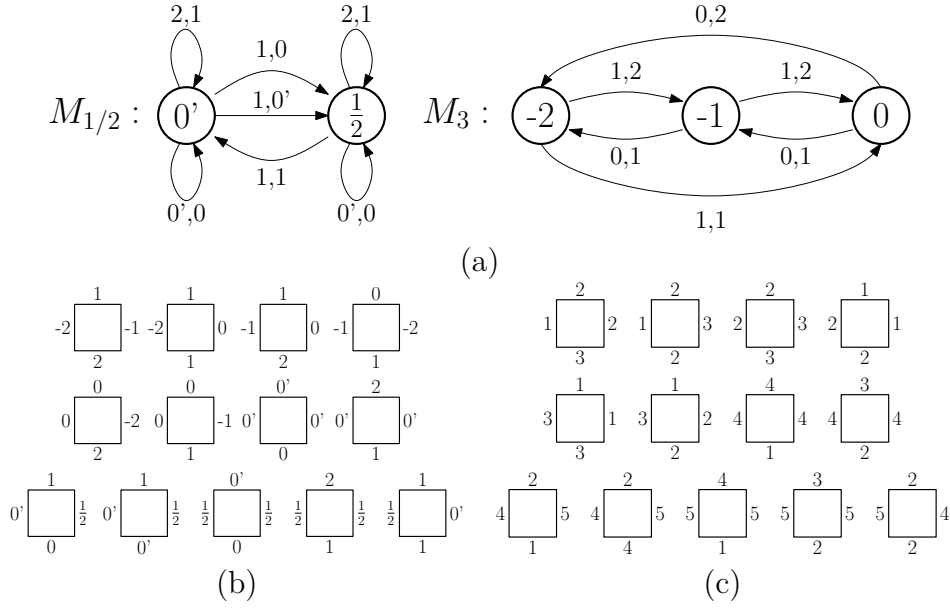


Figure 2.3: Illustration of Culik's set of 13 tiles: (a) Mealy machines, (b) Culik's Wang tiles, (c) indexed tiles (integer edge codes)

over the periodic sequence of length ϑ which reads as

$$q \sum_{i=k+1}^{k+\vartheta} a_{(i,j)} = \sum_{i=k+1}^{k+\vartheta} b_{(i,j)}, \quad \forall i, j, k \in \mathbb{Z}. \tag{2.9}$$

Let the sum of the upper codes values over the periodic sequence in row i be denoted \hat{a}_i .

From the former equation yields $\hat{a}_{i+1} = q\hat{a}_i$. Since the tiling is assumed periodic, after ζ iterations the upper edge codes repeat, i.e. $a_{(i,j)} = a_{(i,j+\zeta)}$ for $\forall i, j \in \mathbb{Z}$. Thus $\hat{a}_i = \hat{a}_{i+\zeta}$ which yields

$$\hat{a}_{i+\zeta} = q^\zeta \hat{a}_i. \tag{2.10}$$

Therefore if the tiling is periodic then the following equation must hold

$$q^\zeta = 1. \tag{2.11}$$

Moreover in ζ iterations m iterations of the first Mealy machine and n iterations of the second occur with $n + m = \zeta$. Hence in the case of the Kari's set the condition expressed in (2.11) results in $(2)^m (\frac{2}{3})^n = 1$, in the case of Culik's set the condition reads $(3)^m (\frac{1}{2})^n = 1$. Both conditions can be rewritten in the form $2^\iota = 3^\kappa$. Since an arbitrary non-zero integer power of 2 is always even and 3 to the power of an arbitrary non-zero integer is always odd, no combination of ι and κ that would satisfy the condition exists. Therefore no tiling is periodic.

Getting back to the definition, T is called aperiodic iff (i) it can produce valid tilings and (ii) none of these valid tilings is periodic. Both of these conditions were proven in the previous paragraphs, hence the tile sets of Kari and Culik are aperiodic.

Tiling a plane with the aperiodic sets of Kari and Culik. A procedure of tiling a plane with the tiles of Kari and Culik is briefly described in this paragraph. Randomly choose real number α from the domain of either tile set. Compute balanced representation of α containing c members, where c is the number of columns in desired tiling. Accordingly to the rules of the tiling, α determinates value of q , multiply α with the appropriate q and compute balanced representation of $q\alpha$. Now, determine the vertical codes $s_{(i,j)} = qA_{i-1}(\alpha) - A_{i-1}(q\alpha)$ and $t_{(i,j)} = qA_i(\alpha) - A_i(q\alpha)$. Match the generated codes with individual tiles and place them in the appropriate positions. Take $\alpha = q\alpha$ and repeat the procedure for the next row

2.1.3 Stochastic Wang tiles sets

The study of aperiodic sets is an interesting branch of mathematics, nevertheless the Wang tiles as a concept have the potential even in a not strictly aperiodic setting. As was mentioned in the introduction to this chapter, an appealing feature of the tiling concept when applied in Computer Graphics is its ability to produce naturally looking non-repetitive patterns [9]. For these purposes the condition on exact aperiodicity in the sense of definition from the previous section is pointlessly strict and the tile sets that are stochastic are sufficient.

In the language of Computer Graphics, the edges of a Wang tile are usually referred to according to the cardinal directions, i.e. W, N, E and S, Fig. 2.4. All the conditions imposed on the tiles presented at the beginning of this chapter are preserved. That means that the tiles are square pieces with codes assigned to their edges and only valid tiling, where the codes in adjacent edges match, is assumed.

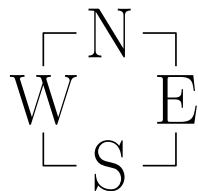


Figure 2.4: Edge nomenclature of stochastic Wang tiles

The nomenclature for the stochastic Wang tiles sets, proposed in [7], is as follows

$$Wn^t/n_1^c - n_2^c,$$

where n^t denotes number of tiles in the set and n_1^c and n_2^c stand for the number of distinct codes on vertical and horizontal edges, respectively.

In the process of creating the tiling, the stochastic tiling algorithm introduced by Cohen [9] can be utilized. The algorithm works as follows. First of all, an empty grid of a desired size is created. One tile from the set is randomly chosen and placed in the upper left corner of the grid, i.t. at the position $(1, 1)$. Then the grid is filled up in column-by-column, row-by-row order. At each step, the edge constraints given by the previously placed tiles are determined. Subsequently a tile randomly chosen from the subset of tiles that satisfy the edge constraints is placed. One step in

the stochastic tiling algorithm is depicted in Fig. 2.5 (b), in the highlighted position tiles number 2 or 5 can be placed.

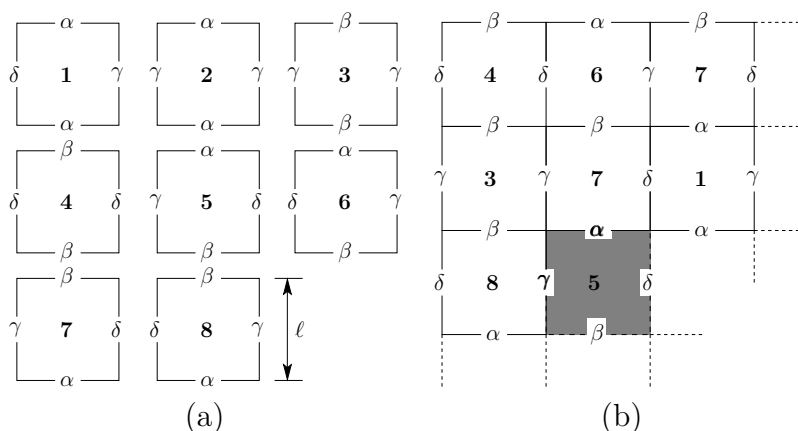


Figure 2.5: Illustration of: (a) Wang tile set W8/2-2, (b) one loop of the stochastic tiling algorithm

Such a procedure allows to produce periodic valid tiling if at least a single tile for every admissible combination of N and W codes is present in the set. The set is called stochastic if at each step of the tiling algorithm at least two tiles can be placed. The minimal number of tiles for the stochastic set is thus defined as $n^t = 2n_1^c n_2^c$. If the tiles are fully determined by the codes, i.e. each code combination represents one unique tile, the maximum number of tiles is $n^t = (n_1^c)^2 (n_2^c)^2$. Such sets are usually called full or complete sets.

Stochastic sets are assumed in this work further on, as they give more freedom in the choice of the number of tiles and codes. Moreover the aperiodic sets of Kari and Culik have always only two different horizontal codes in a row, therefore they are not very suitable for the automated tile design presented in the following chapter.

2.2 The concept of Wang Cubes

Logical extension of the concept of Wang tiles into three dimension has been mentioned already in the paper by Wang [34]. The aperiodic set of Wang cubes was proposed by Culik [44], applications of the stochastic Wang Cubes in Computer Graphics were reported in [45, 46].

The extension is rather straightforward. Wang cubes are the basic elements of the tiling instead of Wang tiles. The tiling is therefore a mapping $f : \mathbb{Z}^3 \rightarrow T$, where T is the set of Wang Cubes. A code is assigned to each of the six faces of the cube and all codes on adjacent faces match each other in valid tiling. The faces can be referred to as W-west, E-east, N-north, S-south, F-front, B-back as depicted in Fig. 2.6.

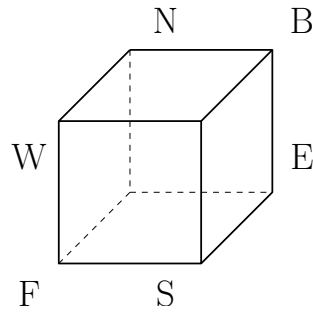


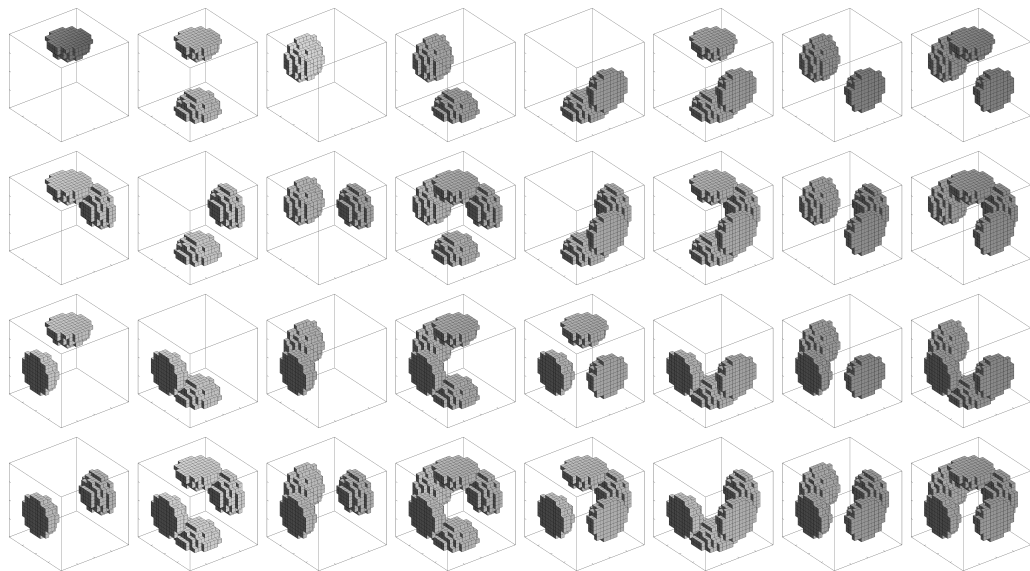
Figure 2.6: Edge nomenclature of stochastic Wang cubes

For the stochastic set the previous nomenclature can be extended as

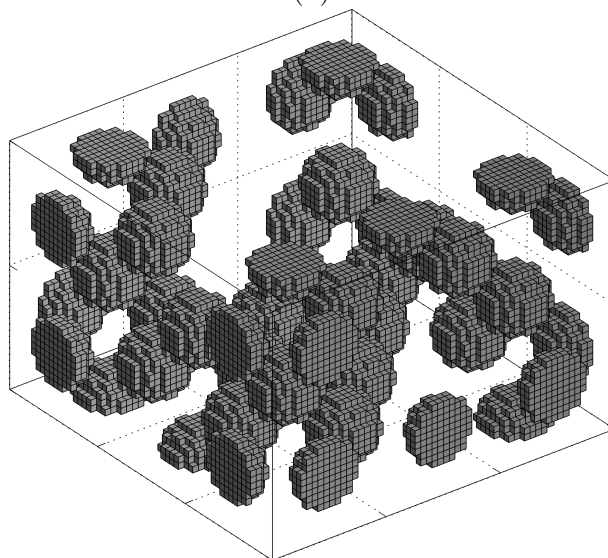
$$Wn^t/n_1^c - n_2^c - n_3^c,$$

where n^t denotes number of Wang cubes and n_1^c, n_2^c and n_3^c stand for number of distinct codes on lateral, horizontal and front-back faces, respectively. The original Cohen's tiling algorithm can be easily expanded by one dimension. Similar to the stochastic tile set, the stochastic cube set should contain at least 2 cubes for each admissible WNF combination, i.e. it contains at least $2n_1^c n_2^c n_3^c$ cubes. A complete Wang cube set consists of $(n_1^c)^2 (n_2^c)^2 (n_3^c)^2$ distinct cubes.

Example of a Wang Cubes set and a spatial tiling generated with the set W32/2-2-2 is shown in Fig. 2.7.



(a)



(b)

Figure 2.7: Example of Wang Cubes: (a) Wang cube set W32/2-2-2, (b) stochastic spatial tiling $3 \times 3 \times 2$ cubes

Chapter 3

Tile morphology design

As mentioned in the previous chapter, the concept of tiling is of a vital interest in Computer Graphics namely for its ability to create homogeneous and naturally looking patterns without visible repetitive artefacts, e.g. [9]. This inspired the current research dealing with a possible utilization of the tiling concept in the area of Materials Engineering. Since the tiling concept itself is only a process of gathering pieces matching certain rules, microstructural information represented by the tile morphology has to be attributed to each tile in order to apply this concept in microstructure compression and reconstruction techniques .

The key issue in the tile morphology design is to ensure the continuity of the information across the congruent edges. This can be achieved in several ways. For instance, the tile morphology can be manually designed or optimized to meet the features of the reference microstructure. While the first is viable only for very simple microstructures or patterns, the optimization methods seem to be general, see [7]. Nevertheless such an approach is computationally expensive and nearly infeasible in the case of high resolution tiles.

This chapter investigates an alternative approach allowing for the automatic tile morphology design introduced by Cohen et al. in [9], which is based on fusing samples of the reference microstructure. Two modifications of the original Image Quilting algorithm [11] are presented and their limitations are discussed. Moreover a number of edge codes is discussed with respect to reducing long-range order artefacts in terms of secondary peaks of $S_2(\mathbf{x})$ statistics. It is compared against the prediction given in [7]. Finally a sensitivity study of input parameters of the automatic design procedure is performed on four microstructures (both artificial and natural materials) in the last section of this chapter.

3.1 Automatic tile morphology design

Cohen et al. presented a very efficient method of automatic Wang tiles' morphology design that exploits samples of reference microstructure. Thereby producing tilings that resemble the original microstructure [9]. The procedure works as follows.

From the specimen of the reference microstructure, as many equi-sized samples as the number of distinct edge codes in the set are excised. Each tile is created as a diamond shaped cut out of the partially overlapping samples, so called r-samples, that are placed accordingly to the edge codes of the tile to be produced, see Fig. 3.1. The samples are fused in the overlapping region seamlessly. The continuity of the microstructural morphology across the adjacent margins is ensured with the diagonal cuts in the r-samples. The edge length l of the final tile is thus derived from the dimension h of the r-samples and the width of the overlap region p as

$$l = \lceil \sqrt{2}(h - p) \rceil, \quad (3.1)$$

where $\lceil \cdot \rceil$ denotes rounding up to the nearest integer (as the discretized representation by means of pixels is assumed).

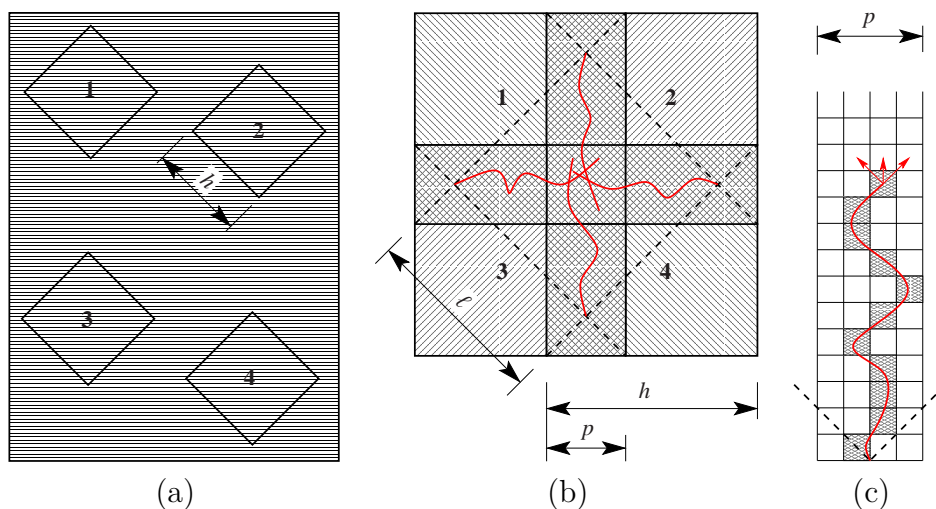


Figure 3.1: Automatic tile design: (a) extraction of edge-code samples of side h from reference specimen (so called r-samples), (b) Wang tile of size l created as diamond-shaped cut from partially overlapping samples, (c) illustration of Image Quilting algorithm in overlap p

A similar methodology was introduced also for the Wang cubes [46] making use of a 3D cutting technique proposed by Kwatra et al. [47].

3.1.1 Image Quilting algorithm

The automatic design rests on procedures that allow fusing the r-samples seamlessly, i.e. without any visual artefacts, in the given overlap region. The original automatic design is based on the Image Quilting algorithm proposed by Efros et al. [11]. It is designed to find the continuous path in the region that minimizes the sum of the differences in the coincident pixel values along the path.

Let assume two samples A and B of height h and width p that entirely overlap each other. The pixel value error $e(i, j)$ is defined as

$$e(i, j) = [A(i, j) - B(i, j)]^2 \quad \forall (i, j) \in h \times p. \quad (3.2)$$

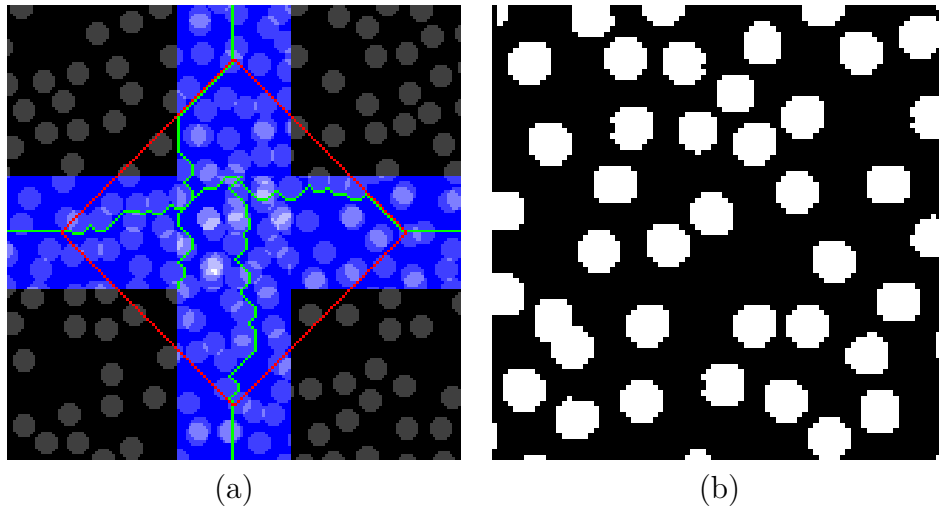


Figure 3.2: Example of: (a) raw data resulting from Image Quilting Algorithm, (b) resulting tile

For each pixel a cumulative error $E(i, j)$ can be calculated as

$$E(i, j) = e(i, j) + \max \{E(i-1, j-1), E(i-1, j), E(i-1, j+1)\} . \quad (3.3)$$

The quilting path is then determined by the lowest cumulative error. The minimal value of E in the bottom row is found and saved, the procedure moves one row up and searches for the minimal value of E within the adjacent pixels to the previously found one. It repeats until the first (top) row is reached, see Algorithm 3.1.

Algorithm 3.1 Image Quilting algorithm

```

for all  $(i, j) \in [1, h] \times [1, p]$  do
     $e(i, j) \leftarrow [A(i, j) - B(i, j)]^2$ 
end for
for all  $(i, j) \in [1, h] \times [1, p]$  do
     $E(i, j) \leftarrow e(i, j) + \max \{E(i-1, j-1), E(i-1, j), E(i-1, j+1)\}$ 
end for
 $i \leftarrow h$ 
 $t(i) \leftarrow j_0, E(i, j_0) = \min \{E(i, j), j \in [1, p]\}$ 
while  $i > 1$  do
     $i \leftarrow i - 1$ 
     $t(i) \leftarrow j_0, E(i, j_0) = \min \{E(i, j), j \in \{t(i+1) - 1, t(i+1), t(i+1) + 1\}\}$ 
end while

```

The path should originate from the vertex of the designed tile, see Fig. 3.1(b). This can be achieved by imposing additional penalty to pixels outside the future tile, for more details consult with the author's bachelor thesis [48].

The simplicity of the algorithm is redeemed with the limitation that the path propagates only diagonally or directly upwards, depicted in Fig. 3.1(c). Moreover, the algorithm does not distinguish whether the path runs through inclusions or

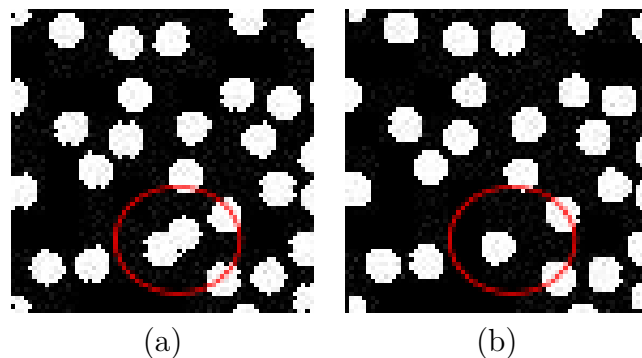


Figure 3.3: Effect of preservation of inclusions' shape due to modified Image Quilting algorithm: (a) original algorithm, (b) modified algorithm

through a matrix phase, therefore it does not preserve shapes of inclusions. This disadvantage, tackled namely in the case of binary media, can be partially eliminated by modifying the definition of the pixel value error in the following manner

$$e(i, j) = \begin{cases} 0, & \text{for } A(i, j) \in \mathcal{D}_m \vee B(i, j) \in \mathcal{D}_m, \\ 1, & \text{for } A(i, j) \notin \mathcal{D}_m \wedge B(i, j) \notin \mathcal{D}_m, \end{cases} \quad (3.4)$$

where \mathcal{D}_m denotes the part of the overlap region occupied with the matrix phase. The result of the modification, in particular that the path prefers the matrix phase, is shown in Fig. 3.3.

3.1.2 Labyrinth algorithm

Modifying the quilting algorithm helps to preserve the shapes, however the quilting path still propagates only upwards. To overcome this limitation an alternative approach to finding a quilting path based on the idea of solving a maze was investigated. Let us assume two overlapping samples of a microstructure that exhibits a strong inclusion-matrix character, i.e. fully percolated medium. A binary error distribution can be calculated making use of Eq. (3.4). The task of the labyrinth algorithm is then to find a continuous path that connects the top and the bottom edge of the error image and such that it is entirely comprised in its zero-part. In other words, it runs only through the matrix phase in the both samples.

One of the basic rules for solving a maze is either the left or the right hand rule. At the starting point, the preferred side is adopted. Then at each labyrinth junction the the algorithm chooses the preferred side. If the chosen way turns out to be a dead-end, the path returns to the last junction and chooses the way next to the previously selected one. Following this procedure, the algorithm either finds the path within a maze or returns to the origin if there is no admissible solution. This algorithm is very easy to implement, however the procedure usually yields a cumbersome quilting path.

In order to find the shortest path the Flood-fill algorithm, see Algorithm 1.1, can be utilized with certain modification. The procedure is based on the idea of water spreading from the origin through the maze. At the beginning, all zero pixels of

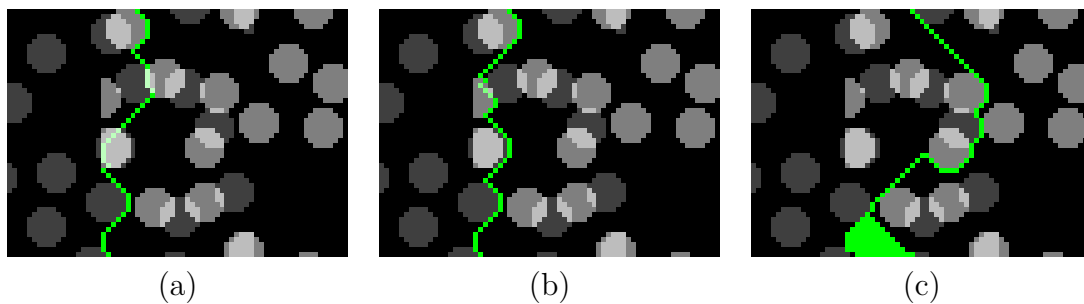


Figure 3.4: Comparison of image fusion algorithms: (a) original Image Quilting algorithm IQA, (b) modified Image Quilting IQM, (c) Labyrinth algorithm LA (quilting path can run arbitrarily through highlighted area)

the error distribution that belong to the chosen boundary are detected and labelled with value $k = 1$. At each following step k all pixels marked $k - 1$, i.e. marked in the previous step, are identified. All zero pixels of the error distribution that i) fall within one-pixel neighbourhood¹ of the identified pixels and ii) that has not yet been signed, are marked with k . The algorithm proceeds until every zero pixel of the error distribution is marked. Thus in the end, the number of steps in which water can reach the point from the initial pixels is attributed to every zero pixel. The quilting path is then again determined by the lowest values. More explicitly, the lowest attributed value is found at the edge opposite to the initial. The quilting path then follows the lowest values of adjacent pixels until it reaches the initial edge.

An advantage of the Labyrinth algorithm rests in its ability to find the quilting path of arbitrary shape. On the other hand an obvious disadvantage of the method is the narrow definition of the error distribution. Unlike the modified Quilting Algorithm it can not handle cases in which no interconnected path through the matrix phases of in both overlapping samples exists. This limitation dominates for microstructures with higher density of inclusions, not to mention dense packings.

3.2 Patched tiles

Tiling reduces the long-range order artefacts, however the rate of the reduction is affine to the number of r-samples involved in the tile set design [7]. In the automatic design the entire microstructural information stored in tiles arises from the edge samples. Even if the minimal stochastic set is assumed, the number of tiles n^t within the set increases with the second power of the number of distinct edge code samples n^c , $n^t = 2n_1^c n_2^c$. This results in relatively large tile sets to reduce parasitic long-range orientation orders, which may be in a contradiction with the intended application in Materials Engineering due to a computational deficiency. On the grounds of this, the aperiodic sets of Culik and Kari in combination with the automatic tile design have a limited ability to reduce the long-range order artefacts

¹Unlike the four-point neighbourhood for the inclusions detection, the eight-point neighbourhood is considered within the Labyrinth algorithm.

²Equal numbers of vertical and horizontal codes are assumed

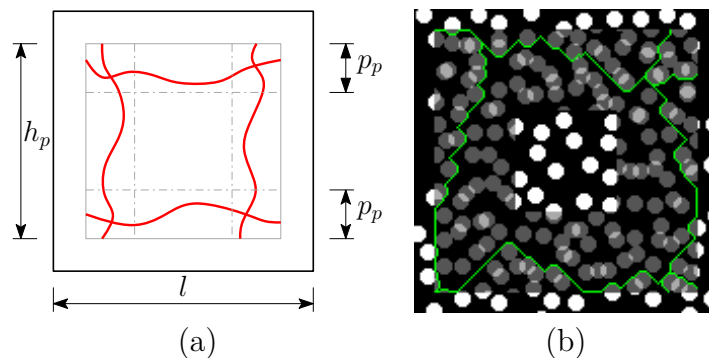


Figure 3.5: Illustration of patching procedure: (a) scheme, (b) raw data with highlighted overlap and quilting paths

as only two distinct edge codes are present in one row. This arises from the fact, that the balanced representation of an arbitrary real number consists always of two integers.

For this reason, additional microstructural information is attached to each tile by means of a square patch, Fig. 3.6. A similar approach was adopted by Somol and Haindl [10]. Except the edge code samples there is also a number of unique patch samples taken from the reference specimen. Number of those patches corresponds with the number of tiles n^t . The patch is then placed at the centre of the tile and fused with the tile image. The appearance of the final tile is governed by the patch dimension h_p with respect to the length of tile l and width of the overlap region p_p . Any of the quilting path algorithms previously presented can be used.

On the one hand, the presented procedure increases demands on the specimen of the reference microstructure that has to be large enough to embody sufficient information, on the other hand the reduction of the repetitiveness is significantly enhanced.

3.3 Reducing long-range orientation order artefacts

The reduction of the periodic nature of the reconstructed image, that has been stated in many articles from the Computer Graphics community, e.g. [9, 29], was, however, only qualified. In [7], the reduction was quantified by means of values of secondary extremes in $S_2(\mathbf{x})$ statistics.

The following formula for predicting the magnitude of secondary $S_2(\mathbf{x})$ extremes was introduced by Novák et al. in [7]

$$\hat{S}_2^P \approx \frac{\Phi^t}{n^t} [\Phi + (n^t - 1)\Phi^2] + \max_i \left\{ \frac{\Phi^e}{n_i^c} [\Phi + (n_i^c - 1)\Phi^2] \right\}, \quad (3.5)$$

where Φ^t and Φ^e denote the volume fraction of the tile interior and the tile edges, respectively, $\Phi^t = 1 - \Phi^e$, Φ is the volume fraction of phase for which $S_2(\mathbf{x})$ statistics

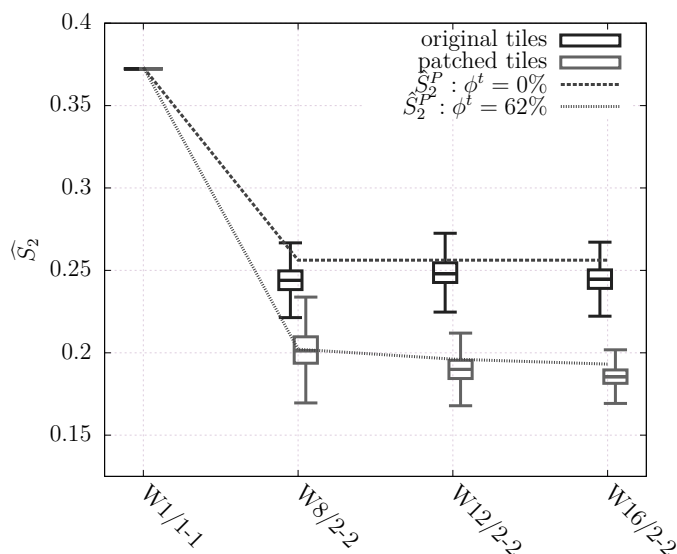


Figure 3.6: Comparison of secondary extremes in S_2 statistics obtained from 10 realizations of 10×10 tiling with prediction \hat{S}_2^P

is calculated, n^t stands for the number of distinct tiles in the set and n_i^c denotes the number of different edge codes in i -th direction.

While in the case of the optimization process adopted in [7] the actual ratio between the tile interior and the area associated with edges can not be rigorously determined, in the case of the patched tiles the ratio of the patch area is straightforward. Recall again, that in the case of unpatched tiles all the microstructural information is attributed solely to edges.

The comparison between the actual reduction of secondary peaks in $S_2(\mathbf{x})$ statistics and prediction (3.5) is depicted in Fig. 3.6.

3.4 Sensitivity study

Performance of the automatic tile design process presented in this chapter depends on many variables, see Fig. 3.8. In this section, an example of a sensitivity analysis, that allows to identify the optimal values of input parameters, is outlined. Such an analysis should be an integral part of each microstructure compression techniques of the automatic design of Wang tiles.

The analysis is performed on four different microstructures, Target Systems, see Fig. 3.7. In particular, microstructures consisting of equi-sized non-permeable [7] and permeable disks, referred to as hard disks (H-disks) and soft disks (S-disks), respectively, are considered. The third microstructure represents distribution of voids in a sandstone. Since the single cross-section of the sandstone specimen, Fig. 1.1(a), turned out not to contain sufficient information, an ensemble of cross-sections is taken as the reference microstructure. The last investigated microstructure is a planar scan of the Alporas[®] aluminium foam. The microstructures are characterized by means of morphometrics, Tab. 3.1, obtained by making use of the programmed

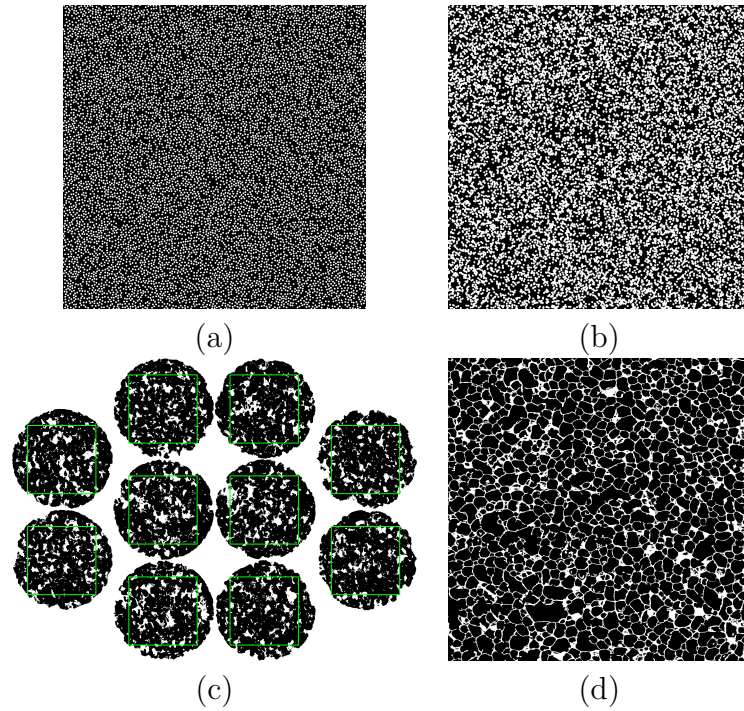


Figure 3.7: Reference microstructures for sensitivity analysis: (a) H-disks, (b) S-disks, (c) sandstone, (d) Alporas[®]

GUI, Fig. 1.4, that employs the Image Processing Toolbox of Matlab environment [23]. The inclusion aspect ratio is calculated as the ratio between major and minor axis length, i.e. the more the inclusion shape is circular, the closer to one it is. Inclusion dimensions are also described with respect to the coordinate system by mean size of the smallest rectangular box that bounds the inclusion.

The analysis is performed in two steps, the first part investigates the optimal overlap and image fusing methods, while the second part examines the impact of the number of edge codes and dimensions of the input samples. The tiling outcomes are quantified in terms of the phase volume fraction and spatial statistics presented in Chapter 1. For the sake of simplicity, the patched tiles were excluded from the analysis as it would result in additional variables.

3.4.1 Optimal overlap

The aim of this section is to find the optimal width p_o of the overlap region in which the two samples are fused. The three image fusing techniques presented in this chapter are considered, namely they are Image Quilting algorithm (IQA), modified Image Quilting algorithm (IQM) and Labyrinth algorithm (LA). For each material a pair of square samples is randomly taken out of the reference microstructure. The two samples are placed side by side overlapping by one pixel. The overlap is then gradually increased to ten times b_x , for each width the latter described quantities are computed. The process is repeated hundred times.

Table 3.1: Morphometrics of Target Systems

| | | | H-disks | S-disks | Sandstone | Alporas [®] |
|-----------------------------------|--------------------|----------|---------|---------|-----------|----------------------|
| Inclusions volume fraction ϕ | [%] | σ | 26.875 | 40.243 | 18.90 | 79.17 |
| | | μ | - | - | 1.70 | - |
| Inclusion area | [px ²] | σ | 51.861 | 169.780 | 426.007 | 1670.303 |
| | | μ | 1.777 | 252.139 | 1243.045 | 5727.649 |
| Equivalent diameter | [px] | σ | 8.125 | 12.363 | 15.281 | 24.515 |
| | | μ | 0.151 | 7.958 | 17.504 | 39.070 |
| Major axis length | [px] | σ | 8.183 | 18.271 | 25.418 | 34.674 |
| | | μ | 0.165 | 16.482 | 32.955 | 61.314 |
| Minor axis length | [px] | σ | 8.154 | 10.931 | 12.991 | 21.007 |
| | | μ | 0.249 | 7.835 | 16.807 | 35.400 |
| Inclusion aspect ratio | [-] | σ | 1.005 | 1.572 | 2.027 | 1.758 |
| | | μ | 0.057 | 0.619 | 0.810 | 0.957 |
| Bounding box b_x | [px] | σ | 7.989 | 14.952 | 19.656 | 30.591 |
| | | μ | 0.194 | 13.016 | 25.585 | 54.275 |
| Bounding box b_y | [px] | σ | 7.987 | 14.810 | 21.482 | 27.654 |
| | | μ | 0.228 | 12.809 | 29.459 | 47.288 |

The total cumulative error E^{IQA} of IQA is plotted against the overlap width p normalized with respect to the bounding box size b_x , Fig. 3.9(a). The same graph is plotted for the IQM algorithm in Fig. 3.9(b). Note that IQM error definition is modified, see Eq. (3.4). In order to compare both algorithms the total cumulative error E^{IQM} is a posteriori computed in the same way as E^{IQA} . For H-disks E^{IQA} falls to zero at the overlap width equal to five or six times the b_x , for the other microstructures the error remains significantly higher even at larger overlap widths. Moreover, in the case of S-disks and Alporas[®] there is no significant improvement in the error after the width of five times the b_x is reached. The very same observation can be done in the case of IQM. Although IQM seems to be useless from the current comparison viewpoint, its significance will arise in a later discussion.

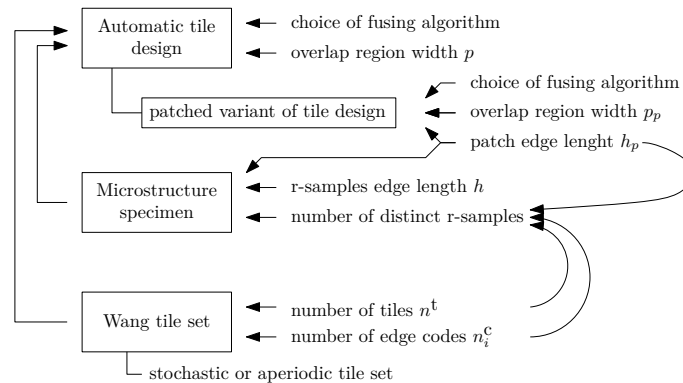


Figure 3.8: Scheme of input variables in automatic tile morphology design (including patched tile variant)

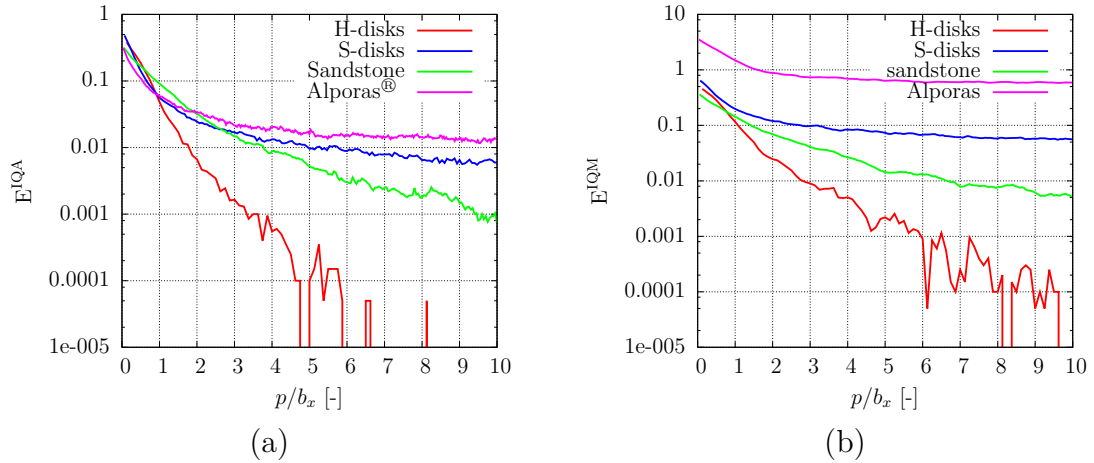


Figure 3.9: Overlap error: (a) IQA, (b) IQM

Since the Labyrinth algorithm either finds a zero error quilting path or fails, its applicability is thus namely determined by the existence of an admissible path. In Fig. 3.10 the probability of a successful LA performance is plotted. It can be seen from Fig. 3.10 that the H-disks microstructure yields probability near one at p/b_x . The same behaviour of the Alporas® foam is due to different definition of the error image, instead of Eq. (3.4), the error is assumed zero if at least one pixel belongs to the ligament phase and one otherwise. This results in a quilting path that propagates within the ligaments. The worst performance of LA is achieved in the case of S-disks, the probability starts to approach one at the overlap width near 50 times the b_x . This is caused by the higher inclusion density.

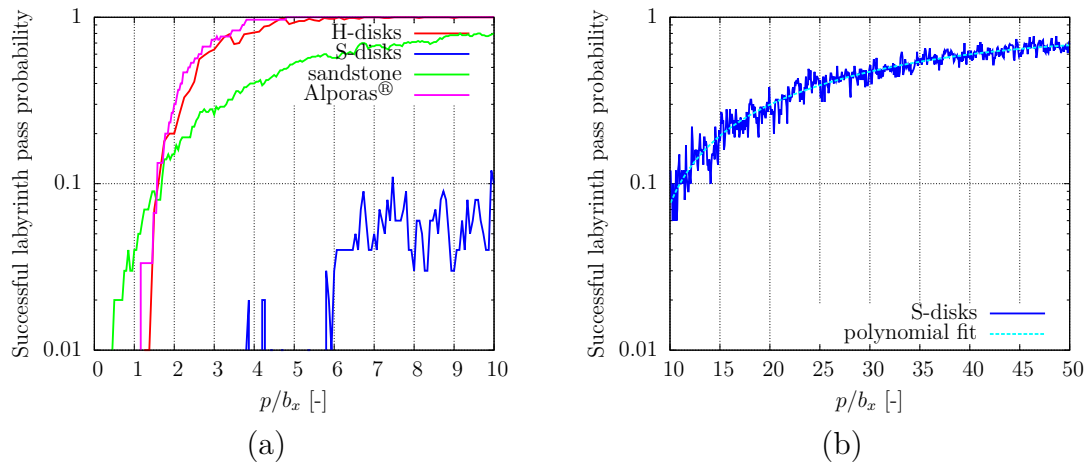


Figure 3.10: Probability of Labyrinth algorithm success through overlap region (polynomial fit: $y = -4.2515 \cdot 10^{-8}x^4 + 5.3486 \cdot 10^{-6}x^3 - 4.6924 \cdot 10^{-4}x^2 + 0.0333x - 0.2159$)

In Fig. 3.11 the fusing algorithms are compared by means of the normalized deviation of inclusion phase volume fraction from that of the target system. The error is defines as

$$E^\phi = |\phi - \phi_{TS}|. \quad (3.6)$$

Recall again that the error was computed for hundred realizations. The thick solid line in Fig. 3.11 depicts the mean value of E^ϕ , dashed thinner lines define the interval $[\sigma - \mu, \sigma + \mu]$ where μ denotes the standard deviation. Data for the LA algorithms are displayed only for overlap sizes for which the algorithm succeeded at least ones. From the curves in Fig. 3.11 no superior algorithm can be identified. The plotted curves exhibit convergence character beyond $p/b_x \approx 5$. In the case of Alporas[®] foam, IQM gives better results even for lower overlap widths. The scatter of values in Fig. 3.11(b) for LA is due to the limited ability of the algorithm to find a quilting path through S-disks. Relatively higher errors for the sandstone microstructures are caused by the variance in the input data, see Tab. 3.1.

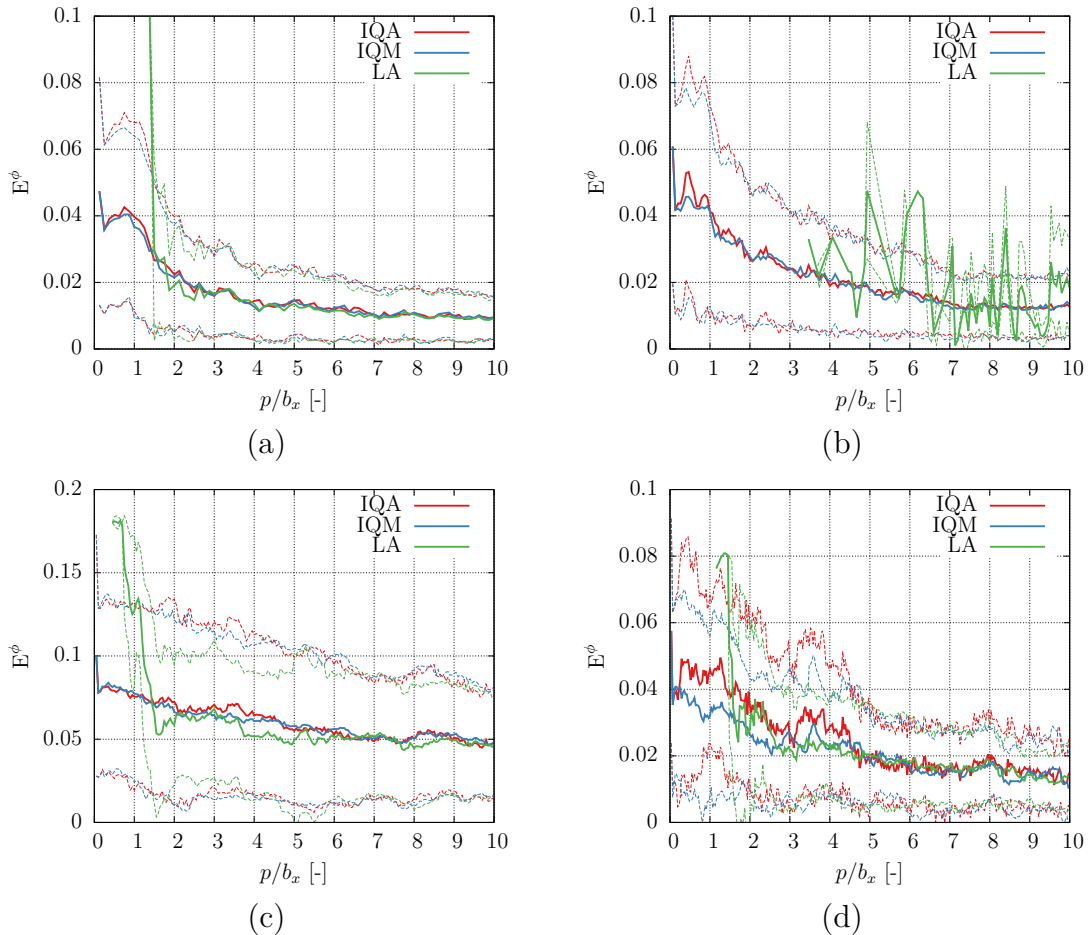


Figure 3.11: Deviation of inclusion phase volume fraction of synthesized microstructures from individual target systems: (a) H-disks, (b) S-disks, (c) sandstone, (d) Alporas[®]

A similar survey was done regarding the shape of inclusions in the fused images.

A suitable statistics that describes the overall shape of inclusions is the two-point cluster function $C_2(\mathbf{x})$, see Section 1.1.2. In order to exclude the influence of the inexact inclusion volume fraction on $C_2(\mathbf{x})$ a normalized variant $\widehat{C}_2(\mathbf{x})$ of $C_2(\mathbf{x})$ was employed. The $\widehat{C}_2(\mathbf{x})$ is scaled so that the maximal value equals one. This statistics was evaluated on 5×5 tiling since inclusions may occur on tiles edges and hence the full shape is revealed only within the tiling. For the very same reason incomplete inclusions taking place at the boundary of the tiling were filtered out. The relative error $E^{\widehat{C}_2}$ was computed as

$$E^{\widehat{C}_2} = \frac{\int_{\Omega} |\widehat{C}_2(\mathbf{x}) - \widehat{C}_{2TS}(\mathbf{x})| d\mathbf{x}}{\int_{\Omega} \widehat{C}_{2TS}(\mathbf{x}) d\mathbf{x}}. \quad (3.7)$$

By means of this metric the introduction of the Modified Image Quilting algorithm and the Labyrinth algorithm is justified. Conclusions based on a visual perception in Fig. 3.3 are quantified in Fig. 3.12(a). Both algorithms, IQM and LA, outperform the original IQA in preserving inclusion shapes. However this holds only for the case of a medium with identical inclusions. For the remaining microstructures all the algorithms are equivalent.

With respect to the above figures the optimal value p_o of the overlap region seems to be circa five or six times the mean inclusion characteristic length measured in the direction of the overlap width. Beyond this width, the additional cost of the improvement is not out-weighted by the additional improvement. The absolute values of p_o are stated in Tab. 3.2. These values are taken as the inputs for the next step of the analysis. Conclusion regarding the fusing algorithms is that for all cases but the microstructure consisting of identical inclusions the Labyrinth algorithm brings no advantage over the remaining two. The original and modified Image Quilting algorithms seem to be equivalent for all cases except the H-disk microstructure.

Table 3.2: Optimal values of overlap width p and tile dimension l

| | | H-disks | S-disks | Sandstone | Alporas [®] |
|-----------|------|---------|---------|-----------|----------------------|
| p_o/b_x | [-] | 5 | 5 | 6 | 6 |
| p_o | [px] | 40 | 75 | 120 | 180 |
| l_o | [px] | 227 | 248 | 255 | 312 |
| h_o | [px] | 200 | 250 | 300 | 400 |

3.4.2 Optimal tile edge length and set diversity

The second part of the analysis investigates the impact of the number of distinct microstructure samples taken out of the reference specimen and their edge length h . The number of r-samples is given by the number of edge codes. The sample edge length h along with the overlap width p then governs the final size l of the automatically designed tile, recall Eq. (3.1). The overlap width is constant arising from the previous part, the modified Image Quilting algorithm was employed for the sample fusion.

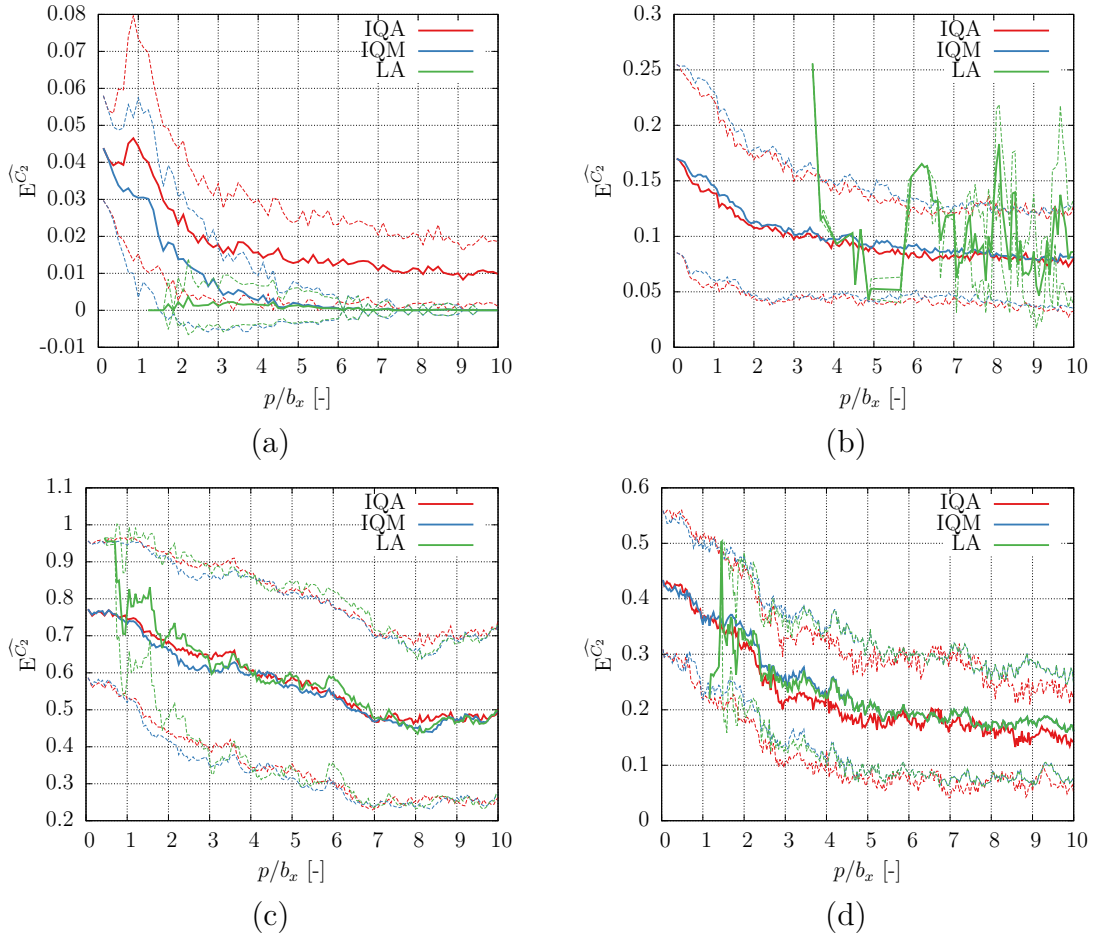


Figure 3.12: Shape error by means of $\widehat{C}_2(\mathbf{x})$: (a) H-disks, (b) S-disks, (c) sandstone, (d) Alporas[®]

For each reference microstructure various tile dimensions l are considered. At first, for each l a number of complete tile sets is generated, consisting of 2, 3, 4 and 5 edge codes on horizontal and vertical edges. From these sets the minimal stochastic subsets are taken such that the subset's inclusion volume fraction matches the target system's one as closely as possible. For each tile set the spatila statistics are computed for a tiling consisting of 5×5 tiles. By analogy to the first part of the sensitivity analysis a hundred tiling realizations were generated but for the two-point cluster function, for which only the first five were used to reduce the computational cost.

The volume fraction deviation Eq.(3.6) for different tile sets is plotted against the tile edge length l in Fig. 3.13. It can be deduced from the graphs that the scatter in the volume fraction decreases with increasing number of tiles within the set and the size of input samples. This confirms the natural expectation of the compression behaviour. Thus desired degree of deviation can be achieved either with increasing the sample edge length or by incorporating more tiles into the set.

The tile edge length l seems to have a negligible impact on reducing the secondary

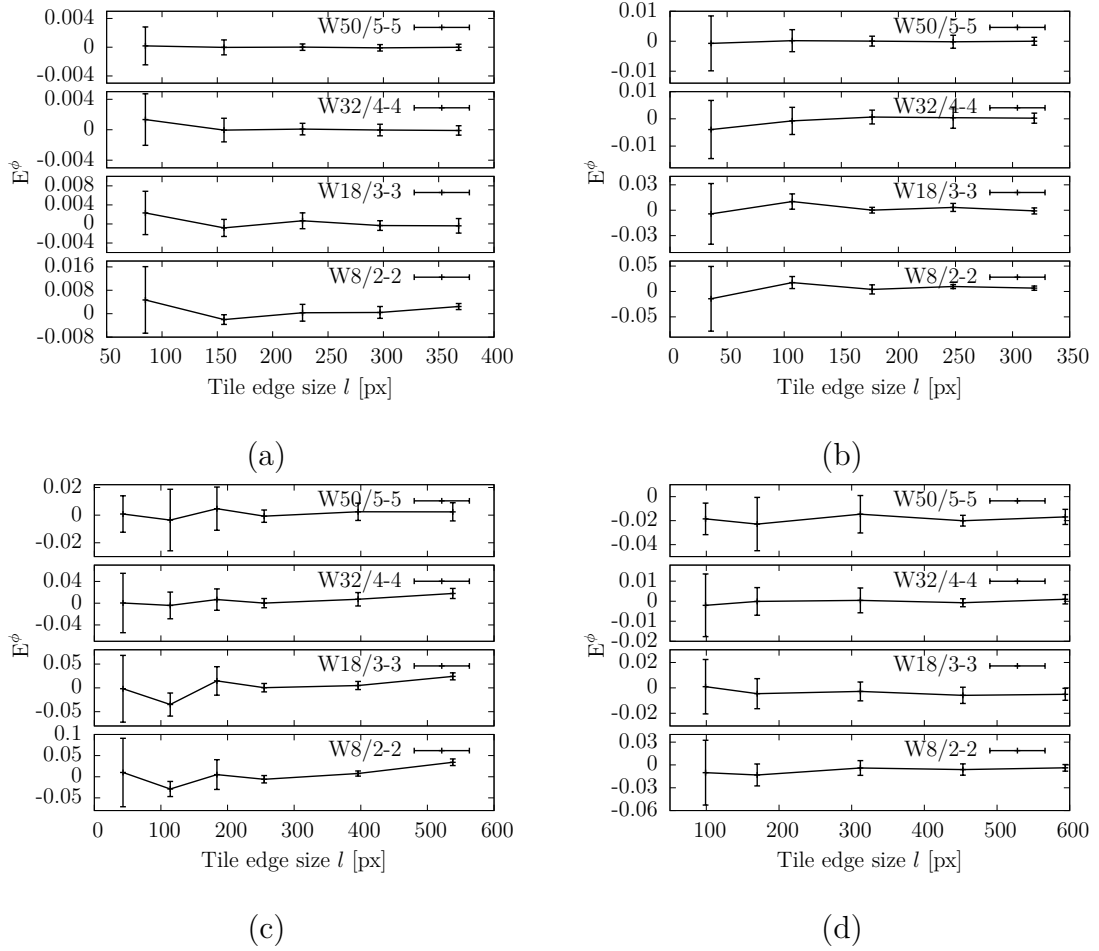


Figure 3.13: Relative error of inclusion phase volume fraction: (a) H-disks, (b) S-disks, (c) sandstone, (d) Alporas[®]

extremes of the two-point probability function, the reduction is governed dominantly by the number of distinct r -samples. In Fig. 3.14 the reduction is compared with the prediction given by Eq. (3.5). The secondary peaks were determined in the same manner as in Section 3.3. Despite some local discrepancies due to a misfit in the volume fraction or local periodicities the overall trend complies with the prediction for all microstructures.

Fig. 3.15 depicts the relationship between the shape error $E^{\widehat{C}_2}$ defined in the previous section and the tile edge length l for the optimal stochastic sets. The graphs indicate a presence of a threshold beyond which only slight improvement is observed.

Optimal values of l resulting from the analysis are provided in Tab. 3.2 along with the corresponding r -samples dimension h . However, these values may vary depending on the desired accuracy. In certain cases minimal tile dimensions can be desired resulting in higher number of tiles, in other cases the larger tiles can be accepted in return for smaller sets. Therefore the values should not be understood as a general rule and a similar sensitivity analysis should be performed any time a microstructure is to be compressed in Wang tiles making use of the automatic design.

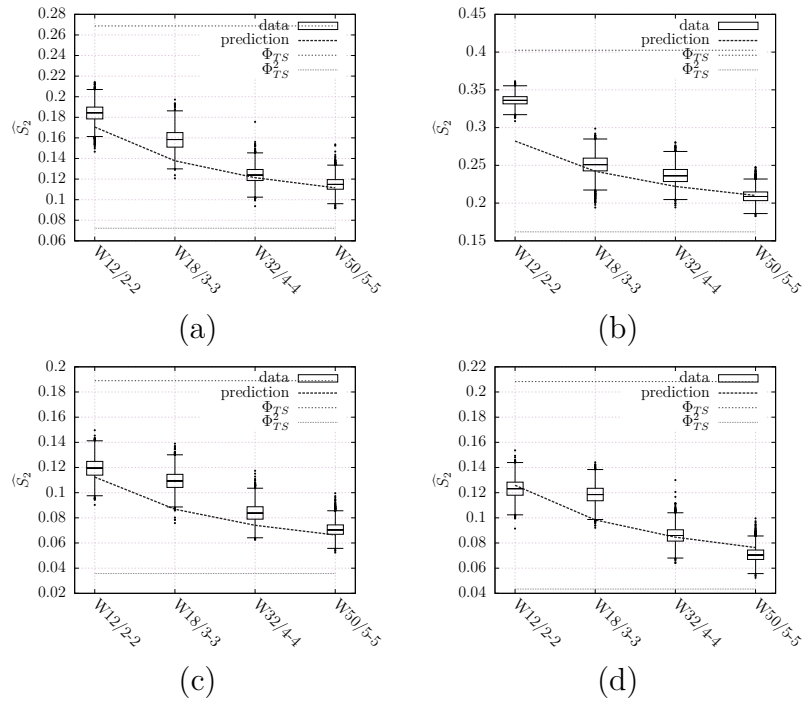


Figure 3.14: Comparison of reduction in secondary extremes \widehat{S}_2 and prediction (3.5): (a) H-disks, (b) S-disks, (c) sandstone, (d) Alporas[®]

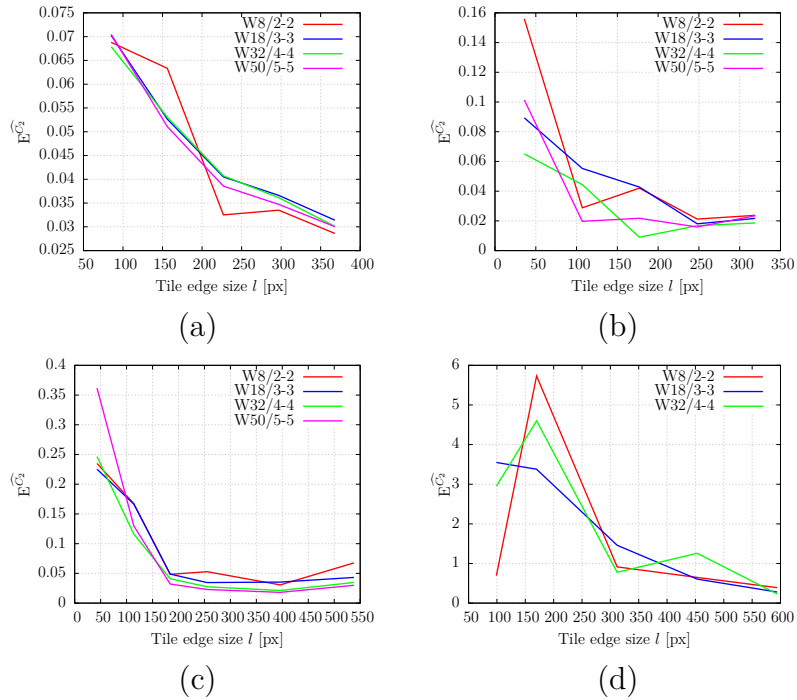


Figure 3.15: Shape error by means of \widehat{E}_{C_2} : (a) H-disks, (b) S-disks, (c) sandstone, (d) Alporas[®]

Examples of the reconstructed microstructures arising from the optimal tile sets are shown in Fig. 3.16. The compressed system W32/4-4 with $l = 312\text{px}$ of the Alporas[®] presents also the input for the Chapter 5, see Fig. 5.1.

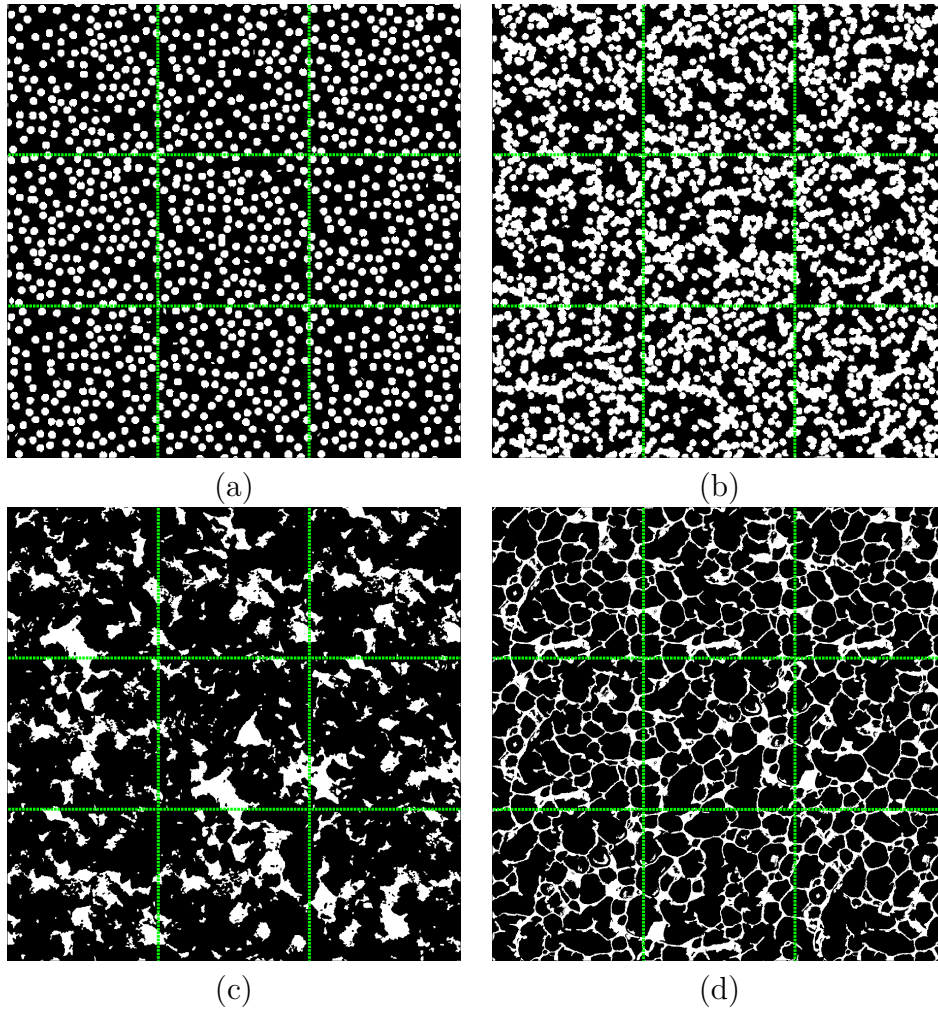


Figure 3.16: Examples of reconstructed microstructures in 3×3 tiling: (a) H-disks, (b) S-disks, (c) sandstone, (d) Alporas[®]

Chapter 4

Application of Wang tiling concept to material homogenization

Two approaches to numerical homogenization based on discrete representation of microstructure are presented in this chapter. An application of the two techniques to the Alporas[®] aluminium foam is the subject of Chapter 5. However, with respect to the representation of the foam microstructure in form of beams, the present homogenization procedures are derived specifically for the Stiffness Method. Nevertheless, the Stiffness Method can be understood as a special case of the Finite Element Method (FEM) with specific choice of basis functions. Thereby the subject of this chapter is applicable in any finite element formulation.

To simplify the exposition, the focus is on linear elasticity. In this thesis the tiling concept is used for an efficient generation of large number of stochastic homogenization models (RVEs). However, it is worthwhile to note that it could have a potential to improve numerical homogenization techniques also in terms of less computational overhead, namely by taking the fact that the RVEs are made up of repetitive patterns into account. From a broader context tiling-based models benefit from a link with domain decomposition methods, performed on a limited number of domains (tiles), which would result in both memory and computer time savings.

4.1 A brief introduction to homogenization

In homogenization theory we deal with the obstacle of substituting a spatially varying heterogeneous material consisting of phases of different thermo-mechanical properties with the equivalent averages defined as

$$\langle \mathbf{f} \rangle = \frac{1}{|\Omega|} \int_{\Omega} \mathbf{f}(\mathbf{x}) \, d\mathbf{x}. \quad (4.1)$$

A macroscopic uniform strain \mathbf{E} applied to an RVE domain results in the local strain $\boldsymbol{\varepsilon}(\mathbf{x})$ and the local stress field $\boldsymbol{\sigma}(\mathbf{x})$. The two fields are, in the case of linear elasticity, coupled by the Hooke's Law

$$\boldsymbol{\sigma}(\mathbf{x}) = \mathbf{D}(\mathbf{x}) : \boldsymbol{\varepsilon}(\mathbf{x}). \quad (4.2)$$

The homogenization process substitutes the material stiffness tensor $\mathbf{D}(\mathbf{x})$ with the spatially invariant tensor \mathbf{D}_{hom} such that

$$\boldsymbol{\Sigma} = \langle \boldsymbol{\sigma}(\mathbf{x}) \rangle = \langle \mathbf{D}(\mathbf{x}) : \boldsymbol{\varepsilon}(\mathbf{x}) \rangle = \mathbf{D}_{hom} : \langle \boldsymbol{\varepsilon}(\mathbf{x}) \rangle = \mathbf{D}_{hom} : \mathbf{E}. \quad (4.3)$$

It yields Hill's lemma [49] coupling the macroscopic (overall) and the microscopic (local) density of the elastic strain energy v in the form

$$\langle v \rangle = \left\langle \frac{1}{2} \boldsymbol{\varepsilon}(\mathbf{x}) : \boldsymbol{\sigma}(\mathbf{x}) \right\rangle = \frac{1}{2} \langle \boldsymbol{\varepsilon}(\mathbf{x}) \rangle : \langle \boldsymbol{\sigma}(\mathbf{x}) \rangle = \frac{1}{2} \mathbf{E} : \boldsymbol{\Sigma}. \quad (4.4)$$

4.2 Homogenization based on the local strain energy

The first of the presented homogenization methods makes use of a natural requirement on the strain energy arising from Hill's lemma (4.4). Integrating the latter equation of the energy density gives rise to the relation between the macroscopic strain energy and the integral of local fields over the domain Ω . In other words, the strain energy Υ stored in a heterogeneous material subjected to macroscopic loads must be equivalent to the energy stored in a homogeneous material of the same volume and subjected to the same excitation.

Thus, making use of the constitutive equation (4.2) and taking into account that $\boldsymbol{\Sigma}$ and \mathbf{E} are constant in Ω yields

$$\Upsilon = \frac{1}{2} \mathbf{E} : \mathbf{D}_{hom} : \mathbf{E} \int_{\Omega} 1 \, d\mathbf{x} = \int_{\Omega} \frac{1}{2} \boldsymbol{\varepsilon}(\mathbf{x}) : \boldsymbol{\sigma}(\mathbf{x}) \, d\mathbf{x}. \quad (4.5)$$

4.2.1 Strain energy of wired model

As was mentioned above the intended application of the both homogenization methods is to provide the overall properties from the beam representation of the microstructure. Local strain energy would be therefore in terms of axial beam displacements and internal forces.

Adopting the Timoshenko beam theory, the only stresses taking place at the cross-section are the axial stress σ_{xx} and the transversal shear stress τ_{xz} . Hence, the formula for elastic strain energy of a deformed beam yields

$$\Upsilon = \int_{\Omega} \frac{1}{2} \sigma_{ij} \varepsilon_{ij} \, d\Omega = \int_{\Omega} \frac{1}{2} \sigma_{xx} \varepsilon_{xx} + \tau_{xz} \gamma_{xz} \, d\Omega. \quad (4.6)$$

The latter equation rewritten in terms of internal forces [50] thus yields

$$\Upsilon = \frac{1}{2} \sum_i^n \int_{L_i} \left(\frac{N^2(x)}{E_i A_i} + \frac{V^2(x)}{G_i k_i A_i} + \frac{M^2(x)}{E_i I_i} \right) dx, \quad (4.7)$$

where E stands for the Young's modulus of the beam material, A denotes the area of the cross-section, I is the moment of inertia. The internal forces are denoted as

follows: $N(x)$ is the axial force, $M(x)$ denotes a bending moment around the y axis and $V(x)$ stands for a shear force. Parameter k is energy-consistent correction due to a constant approximation of τ_{xz} across the beam cross-section.

Since the external load is applied only at nodes and the beams are assumed prismatic, normal and shear forces are constant along the length of the beam and a bending moment is linear. Integrating the above equation, it can be rewritten in terms of local nodal forces (denoted with subscripts $_1$ and $_2$)

$$\Upsilon = \frac{1}{2} \sum_i^n \left(\frac{1}{E_i A_i} (N_1^2 L_i) + \frac{1}{E_i k_i A_i} (V_1^2 L_i) + \frac{1}{3 E_i I_i} L_i (M_1^2 + M_1 M_2 + M_2^2) \right). \quad (4.8)$$

The total elastic energy stored within the RVE wired model can be thus computed as the sum of energy contributions stored within each beam.

4.2.2 Strain energy of homogeneous isotropic material

Recall the equation for the strain energy of a linear elastic homogeneous body in the form

$$\Upsilon = \int_{\Omega} \frac{1}{2} \boldsymbol{\varepsilon}(\mathbf{x}) : \mathbf{D} : \boldsymbol{\varepsilon}(\mathbf{x}) \, d\mathbf{x}. \quad (4.9)$$

In the case of the isotropic material the elastic stiffness tensor \mathbf{D} can be expressed in terms of bulk and shear moduli as

$$\mathbf{D} = 3K\mathbf{I}_V + 2G\mathbf{I}_D, \quad (4.10)$$

with projection tensors defined as

$$\mathbf{I}_V = \frac{1}{3} \mathbf{1} \otimes \mathbf{1}, \quad (4.11)$$

$$I_{ijkl}^V = \frac{1}{3} \delta_{ij} \delta_{kl}, \quad (4.12)$$

$$I_{ijkl}^S = \frac{1}{2} (\delta_{ik} \delta_{jl} + \delta_{il} \delta_{jk}), \quad (4.13)$$

$$\mathbf{I}_D = \mathbf{I}_S - \mathbf{I}_V. \quad (4.14)$$

The symmetric deformation tensor $\boldsymbol{\varepsilon}$ can be decomposed into a volumetric $\boldsymbol{\varepsilon}_V$ and a deviatoric $\boldsymbol{\varepsilon}_D$ part making use of the property (4.14) of the projection tensors as

$$\boldsymbol{\varepsilon} = \mathbf{I}_S : \boldsymbol{\varepsilon} = (\mathbf{I}_V + \mathbf{I}_D) : \boldsymbol{\varepsilon} = \mathbf{I}_V : \boldsymbol{\varepsilon} + \mathbf{I}_D : \boldsymbol{\varepsilon} = \boldsymbol{\varepsilon}_V + \boldsymbol{\varepsilon}_D. \quad (4.15)$$

Introducing Eq. (4.11) and Eq. (4.14), $\boldsymbol{\varepsilon}_V$ and $\boldsymbol{\varepsilon}_D$ yields

$$\boldsymbol{\varepsilon}_V = \mathbf{I}_V : \boldsymbol{\varepsilon} = \frac{1}{3} \boldsymbol{\varepsilon}_V \mathbf{1}, \quad (4.16)$$

$$\boldsymbol{\varepsilon}_D = \mathbf{I}_D : \boldsymbol{\varepsilon}, \quad (4.17)$$

where $\text{tr}(\boldsymbol{\varepsilon}_D) = 0$. Evidently, the Eq. (4.15) can be recast as

$$\boldsymbol{\varepsilon} = \frac{1}{3}\varepsilon_V \mathbf{1} + \boldsymbol{\varepsilon}_D. \quad (4.18)$$

Considering Eq. (4.10), the strain energy density v can be written in the form

$$2v = \boldsymbol{\varepsilon} : (3K\mathbf{I}_V + 2G\mathbf{I}_D) : \boldsymbol{\varepsilon}. \quad (4.19)$$

Introducing Eq. (4.18) into Eq. (4.19) and taking into account the fact that $\mathbf{I}_V : \mathbf{1} = \mathbf{1}$, $\mathbf{I}_D : \mathbf{1} = 0$ and $\mathbf{I}_D : \boldsymbol{\varepsilon}_D = 0$ yields

$$2v = \left(\frac{1}{3}\varepsilon_V \mathbf{1} + \boldsymbol{\varepsilon}_D\right) : (K\varepsilon_V \mathbf{1} + 2G\boldsymbol{\varepsilon}_D). \quad (4.20)$$

Furthermore, acknowledging $\boldsymbol{\varepsilon}_D : \mathbf{1} = 0$ gives

$$2v = K\varepsilon_V^2 \frac{1}{3} \mathbf{1} : \mathbf{1} + 2G\boldsymbol{\varepsilon}_D : \boldsymbol{\varepsilon}_D. \quad (4.21)$$

Hence the elastic energy Υ stored in a homogeneous isotropic linear elastic body reads as

$$\Upsilon = \int_{\Omega} \frac{1}{2} K\varepsilon_V^2 + G\boldsymbol{\varepsilon}_D : \boldsymbol{\varepsilon}_D \, d\Omega. \quad (4.22)$$

4.2.3 Numerical implementation

Assume that the finite element model consisting of beams representing the geometry of analysed material (e.g. foam ligaments) has been generated using Wang tiling and that the algebraic representation in terms of the global stiffness matrix has been constructed. All displacements at the boundary Γ are prescribed, i.e. $\Gamma = \Gamma_u$. In particular, in the case of kinematic uniform boundary conditions (KUBC), the boundary displacements are prescribed as

$$\mathbf{u}(\mathbf{x}) = \mathbf{x} \cdot \mathbf{E}, \quad \mathbf{x} \in \Gamma. \quad (4.23)$$

The volume average of the strain field over the domain Ω is then by definition equal to prescribed macroscopic strain tensor \mathbf{E}

$$\langle \boldsymbol{\varepsilon}(\mathbf{x}) \rangle = \mathbf{E}. \quad (4.24)$$

Furthermore, for any prescribed \mathbf{E} the strain energy Υ within the Ω can be computed by employing Eq. (4.8).

To obtain the effective bulk modulus K the macroscopic strain tensor \mathbf{E} can be prescribed in such a form that $\varepsilon_V = 1$ and $\boldsymbol{\varepsilon}_D = \mathbf{0}$. This can be achieved with tensors \mathbf{E} in the form

$$\mathbf{E}_V = \begin{bmatrix} E_{11} & 0 \\ 0 & E_{22} \end{bmatrix}, \quad \text{such that } E_{11} + E_{22} = 1, \text{ e.g. } \mathbf{E}_V = \begin{bmatrix} \frac{1}{2} & 0 \\ 0 & \frac{1}{2} \end{bmatrix}. \quad (4.25)$$

The expression for the macroscopic strain energy in Eq. (4.22) then reduces to

$$\Upsilon = \int_{\Omega} \frac{1}{2} K E_V^2 d\Omega = \frac{1}{2} K E_V^2 \int_{\Omega} d\Omega = \frac{1}{2} K |\Omega|, \quad (4.26)$$

and provides the formula for the effective bulk modulus K in the form

$$K = \frac{2\Upsilon}{|\Omega|}. \quad (4.27)$$

By analogy to the previous derivation, the overall shear modulus G can be obtained with the macroscopic strain prescribed in such a form that fullfills $\boldsymbol{\varepsilon}_D : \boldsymbol{\varepsilon}_D = 1$, e.g.

$$\mathbf{E}_D = \begin{bmatrix} 0 & \frac{1}{\sqrt{2}} \\ \frac{1}{\sqrt{2}} & 0 \end{bmatrix}. \quad (4.28)$$

Introducing the latter equation into Eq. (4.22) yields

$$\Upsilon = \int_{\Omega} G \mathbf{E}_D : \mathbf{E}_D d\Omega = G \int_{\Omega} d\Omega = G |\Omega|, \quad (4.29)$$

which gives

$$G = \frac{\Upsilon}{|\Omega|}. \quad (4.30)$$

In summary, the presented homogenization procedure gives the overall isotropic constants K and G in two steps. A limitation of this approach is that the homogeneous material is a priori assumed isotropic. An insight of the correctness of the isotropy assumption can be achieved by prescribing unequal strain components E_{ii} in multiple steps and monitoring the sensitivity of K for individual choices.

4.3 Homogenization based on the concept of macroscopic degrees of freedom

In the previous homogenization approach the boundary displacements were prescribed along the entire Γ , the local strains and inner forces were computed and the sum of the strain energy within elements delivered the effective elastic constants. A natural question arises whether those mid-steps could be omitted and a straightforward way to homogenized properties applied.

It turned out [6] that the effective properties can be extracted directly from the global stiffness matrix of the FE model by adding certain degrees of freedom. This approach is well known among scientists, one of the first papers summarizing this procedure was due to Michel et al. [51].

4.3.1 Central idea

The main idea of the approach is to decompose the displacement field $\mathbf{u}(\mathbf{x})$ in two parts, the displacement field $\mathbf{u}^E(\mathbf{x})$ related to the homogeneous macroscopic strain

tensor \mathbf{E} and the field $\mathbf{u}^*(\mathbf{x})$ representing its perturbation (so called fluctuation part), so that

$$\mathbf{u}(\mathbf{x}) = \mathbf{u}^E(\mathbf{x}) + \mathbf{u}^*(\mathbf{x}), \quad (4.31)$$

where

$$\mathbf{u}^E(\mathbf{x}) = \mathbf{E} \cdot \mathbf{x}. \quad (4.32)$$

Substituting equations (4.31) and (4.32) into the geometric strain definition

$$\boldsymbol{\varepsilon}(\mathbf{x}) = \nabla^s \mathbf{u}(\mathbf{x}), \quad (4.33)$$

where ∇^s denotes the symmetric gradient operator defined as

$$\nabla^s = \frac{1}{2} (\nabla + \nabla^T), \quad (4.34)$$

with $\nabla_i = \frac{\partial}{\partial x_i}$.

Eq. (4.33) along with the decomposition (4.31) yields

$$\boldsymbol{\varepsilon}(\mathbf{x}) = \mathbf{E} + \nabla^s \mathbf{u}^*(\mathbf{x}). \quad (4.35)$$

A traditional expression for the elastic strain energy Υ in terms of the symmetric gradient of the displacement field $\mathbf{u}(\mathbf{x})$ reads as

$$\Upsilon(\mathbf{u}(\mathbf{x})) = \frac{1}{2} \int_{\Omega} (\nabla^s \mathbf{u}(\mathbf{x}) : \mathbf{D} : \nabla^s \mathbf{u}(\mathbf{x})) \, d\mathbf{x}, \quad (4.36)$$

which can be recast by introducing Eq. (4.35) to

$$\Upsilon(\mathbf{E}, \mathbf{u}^*(\mathbf{x})) = \frac{1}{2} \int_{\Omega} (\mathbf{E} + \nabla^s \mathbf{u}^*(\mathbf{x})) : \mathbf{D} : (\mathbf{E} + \nabla^s \mathbf{u}^*(\mathbf{x})) \, d\mathbf{x}. \quad (4.37)$$

The previous equation is valid for all kinematically admissible fields $\tilde{\mathbf{u}}(\mathbf{x})$. From the Lagrange principle of minimum potential energy the actual state $\mathbf{u}^*(\mathbf{x})$ can be identified by minimizing (4.37) with respect to $\tilde{\mathbf{u}}(\mathbf{x})$ as

$$\frac{\partial}{\partial \tilde{\mathbf{u}}} \Upsilon(\mathbf{E}, \tilde{\mathbf{u}}(\mathbf{x}))|_{\tilde{\mathbf{u}}=\mathbf{u}^*} = 0. \quad (4.38)$$

Note, that all following derivatives are in sense of Gâteaux derivative. Since the strain energy is a quadratic form in both \mathbf{E} and $\tilde{\mathbf{u}}(\mathbf{x})$, the first derivative with respect to $\tilde{\mathbf{u}}(\mathbf{x})$ also consist of both terms, thus the condition (4.38) yields a relation between \mathbf{E} and $\mathbf{u}^*(\mathbf{x})$. The potential energy can be expressed in terms of \mathbf{E} as $\Upsilon(\mathbf{E})$.

Recall the definition of elastic strain energy density v

$$v(\boldsymbol{\varepsilon}(\mathbf{x})) = \frac{1}{2} \boldsymbol{\sigma}(\boldsymbol{\varepsilon}(\mathbf{x})) : \boldsymbol{\varepsilon}(\mathbf{x}). \quad (4.39)$$

The total energy potential then reads as

$$\Upsilon(\boldsymbol{\varepsilon}(\mathbf{x})) = \int_{\Omega} v(\boldsymbol{\varepsilon}(\mathbf{x})) \, d\mathbf{x}. \quad (4.40)$$

The volume average of v thus yields

$$\langle v \rangle = \frac{1}{|\Omega|} \int_{\Omega} v(\boldsymbol{\varepsilon}(\mathbf{x})) \, d\mathbf{x} = \frac{1}{|\Omega|} \Upsilon(\boldsymbol{\varepsilon}(\mathbf{x})). \quad (4.41)$$

By making use of Hill's lemma [6, 49]

$$2\langle v \rangle = \langle \boldsymbol{\varepsilon}(\mathbf{x}) : \boldsymbol{\sigma}(\mathbf{x}) \rangle = \langle \boldsymbol{\varepsilon}(\mathbf{x}) \rangle : \langle \boldsymbol{\sigma}(\mathbf{x}) \rangle = \mathbf{E} : \boldsymbol{\Sigma}, \quad (4.42)$$

we arrive at the relation between the potential energy expressed as a function of the local strain and stress fields and their macroscopic counterparts \mathbf{E} and $\boldsymbol{\Sigma}$ as

$$2\langle v \rangle = \frac{2}{|\Omega|} \Upsilon(\mathbf{E}) = \langle \boldsymbol{\varepsilon}(\mathbf{x}) \rangle : \langle \boldsymbol{\sigma}(\mathbf{x}) \rangle = \mathbf{E} : \boldsymbol{\Sigma}. \quad (4.43)$$

From Eq. (4.43) the macroscopic stress tensor yields the first derivative of the average density of the total potential energy

$$\boldsymbol{\Sigma} = \frac{2}{|\Omega|} \frac{\partial \Upsilon(\mathbf{E})}{\partial \mathbf{E}}. \quad (4.44)$$

Substituting $\boldsymbol{\Sigma}$ from the following definition

$$\boldsymbol{\Sigma} = \mathbf{D}_{hom} : \mathbf{E} \quad (4.45)$$

results in the explicit formula for the homogeneous stiffness tensor as

$$\mathbf{D}_{hom} = \frac{2}{|\Omega|} \frac{\partial^2 \Upsilon(\mathbf{E})}{\partial \mathbf{E}^2}. \quad (4.46)$$

Recall that the above procedure assumes prescribed kinematic uniform boundary conditions (KUBC) in the form of Eq. (4.32) on $\Gamma = \Gamma_u$, thus $\mathbf{u}^*(\mathbf{x}) = 0$, $\forall \mathbf{x} \in \Gamma$. As a consequence, the volume average of a strain perturbation field vanishes

$$\langle \boldsymbol{\varepsilon}^*(\mathbf{x}) \rangle = \langle \nabla^s \mathbf{u}^*(\mathbf{x}) \rangle = \frac{1}{|\Omega|} \int_{\Omega} \nabla^s \mathbf{u}^*(\mathbf{x}) \, d\mathbf{x} = \frac{1}{|\Omega|} \oint_{\Gamma} \mathbf{n} \otimes \mathbf{u}^*(\mathbf{x}) \, d\mathbf{x} = 0. \quad (4.47)$$

This also implies that the work done by $\langle \boldsymbol{\sigma} \rangle$ on $\langle \boldsymbol{\varepsilon}^*(\mathbf{x}) \rangle$ is zero which will arise later in the special form of the set of linear equations.

It can be shown that in the case of the periodic boundary conditions the volume average $\langle \mathbf{u}^*(\mathbf{x}) \rangle$ also vanishes, hence the same statement considering zero work done by the stress volume average holds as well [51].

4.3.2 Direct Stiffness method

The Stiffness method is an approach to solve the kinematics of beam structures. From a certain point of view, this approach can be seen as a special case of the finite element method with a specific choice of approximation functions. In a local coordinate system the transversal displacements are approximated with fourth-order polynomials which arise from the solution of differential equation of the Deflection Curve based on the Timoshenko hypothesis. The Bernouli-Navier hypothesis could be assumed as well, but in order to remain energy-consistent the contribution of shear forces to the total potential energy in Eq. (4.8) would be then neglected.

In the Direct Stiffness method the elements' nodal forces are related to the end points' degrees of freedom (DOFs) as (assuming no loading is applied within the beam)

$$\mathbf{f}_e = \mathbf{K}_e \mathbf{u}_e, \quad (4.48)$$

where

$$\mathbf{u}_e = \{u_1, v_1, \phi_1, u_2, v_2, \phi_2\}^T, \quad \mathbf{f}_e = \{N_1, V_1, M_1, N_2, V_2, M_2\}^T \quad (4.49)$$

and

$$\mathbf{K}_e = \mathbf{T}^T \mathbf{K}_e^\ell \mathbf{T}. \quad (4.50)$$

The local stiffness matrix \mathbf{K}_e^ℓ arising from the Timoshenko theory has the form [52]

$$\mathbf{K}_e^\ell = \begin{bmatrix} \frac{EA}{L} & 0 & 0 & -\frac{EA}{L} & 0 & 0 \\ 0 & \frac{12}{1+\Phi} \frac{EI}{L^3} & -\frac{6}{1+\Phi} \frac{EI}{L^2} & 0 & -\frac{12}{1+\Phi} \frac{EI}{L^3} & -\frac{6}{1+\Phi} \frac{EI}{L^2} \\ 0 & -\frac{6}{1+\Phi} \frac{EI}{L^2} & \frac{4+\Phi}{1+\Phi} \frac{EI}{L} & 0 & \frac{6}{1+\Phi} \frac{EI}{L^2} & \frac{2-\Phi}{1+\Phi} \frac{EI}{L} \\ -\frac{EA}{L} & 0 & 0 & \frac{EA}{L} & 0 & 0 \\ 0 & -\frac{12}{1+\Phi} \frac{EI}{L^3} & \frac{6}{1+\Phi} \frac{EI}{L^2} & 0 & \frac{12}{1+\Phi} \frac{EI}{L^3} & \frac{6}{1+\Phi} \frac{EI}{L^2} \\ 0 & -\frac{6}{1+\Phi} \frac{EI}{L^2} & \frac{2-\Phi}{1+\Phi} \frac{EI}{L} & 0 & \frac{6}{1+\Phi} \frac{EI}{L^2} & \frac{4+\Phi}{1+\Phi} \frac{EI}{L} \end{bmatrix}, \quad (4.51)$$

with $\Phi = \frac{12EI}{GkAL^2}$. Note that the local stiffness matrix for the Bernoulli-Navier hypothesis can be obtained with $\Phi = 0$. The transformation matrix \mathbf{T} reads as

$$\mathbf{K}_e^\ell = \begin{bmatrix} \cos(\varphi) & \sin(\varphi) & 0 & 0 & 0 & 0 \\ -\sin(\varphi) & \cos(\varphi) & 0 & 0 & 0 & 0 \\ 0 & 0 & 1 & 0 & 0 & 0 \\ 0 & 0 & 0 & \cos(\varphi) & \sin(\varphi) & 0 \\ 0 & 0 & 0 & -\sin(\varphi) & \cos(\varphi) & 0 \\ 0 & 0 & 0 & 0 & 0 & 1 \end{bmatrix}, \quad (4.52)$$

where φ is an angle between the global x axis and a beam axis.

The strain energy Υ_e stored within a deformed beam (let's call it an element as in the case of conventional FEM) reads as

$$\Upsilon_e(\mathbf{u}_e, \mathbf{f}_e) = \frac{1}{2} \mathbf{f}_e^T \mathbf{u}_e. \quad (4.53)$$

Considering Eq. (4.48) the latter equation can be expressed in the form

$$\Upsilon_e(\mathbf{u}_e) = \frac{1}{2} \mathbf{u}_e^T \mathbf{K}_e \mathbf{u}_e, \quad (4.54)$$

that leads to the total energy of the entire structure as

$$\Upsilon = \frac{1}{2} \sum_{e=1}^N \mathbf{u}_e^T \mathbf{K}_e \mathbf{u}_e. \quad (4.55)$$

Adopting the displacement decomposition (4.31) gives

$$\mathbf{u} = \begin{bmatrix} \mathbf{I} & \mathbf{A}_e \end{bmatrix} \begin{Bmatrix} \mathbf{u}_e^* \\ \mathbf{E} \end{Bmatrix}, \quad (4.56)$$

where \mathbf{I} is a unit matrix of 6×6 entries and

$$\mathbf{A}_e = \begin{bmatrix} x_1 & 0 & \frac{1}{2}y_1 \\ 0 & y_1 & \frac{1}{2}x_1 \\ 0 & 0 & 0 \\ x_2 & 0 & \frac{1}{2}y_2 \\ 0 & y_2 & \frac{1}{2}x_2 \\ 0 & 0 & 0 \end{bmatrix}. \quad (4.57)$$

\mathbf{A} is the matrix coupling the nodal DOFs with the macroscopic deformation $\mathbf{E} = \{\varepsilon_x, \varepsilon_y, \gamma_{xy}\}$.

Introducing Eq. (4.56) to the local strain energy expression in (4.54) results in

$$\Upsilon_e = \frac{1}{2} \begin{Bmatrix} \mathbf{u}_e^* \\ \mathbf{E} \end{Bmatrix}^T \underbrace{\begin{bmatrix} \mathbf{I} & \mathbf{A}_e \end{bmatrix}^T \mathbf{K}_e \begin{bmatrix} \mathbf{I} & \mathbf{A}_e \end{bmatrix}}_{\mathbf{K}_e^{ex}} \begin{Bmatrix} \mathbf{u}_e^* \\ \mathbf{E} \end{Bmatrix}, \quad (4.58)$$

where

$$\mathbf{K}_e^{ex} = \begin{bmatrix} \mathbf{K}_e & \mathbf{K}_e \mathbf{A}_e \\ \mathbf{A}_e^T \mathbf{K}_e & \mathbf{A}_e^T \mathbf{K}_e \mathbf{A}_e \end{bmatrix} \quad (4.59)$$

stands for the extended stiffness matrix of an element.

Unknown global perturbation DOFs \mathbf{u}^* can be assembled to a vector of unknowns \mathbf{r} with respect to fixed/prescribed boundary values as

$$\mathbf{r} = \mathbf{A} \begin{Bmatrix} \mathbf{u}_e^* \end{Bmatrix}, \quad (4.60)$$

where \mathbf{A} denotes the assembly operator [6].

The expression for the extended global stiffness matrix \mathbf{K}^{ex} takes the form

$$\mathbf{K}^{ex} = \begin{bmatrix} \mathbf{K}_{11} & \mathbf{K}_{12} \\ \mathbf{K}_{21} & \mathbf{K}_{22} \end{bmatrix}, \quad (4.61)$$

where

$$\mathbf{K}_{11} = \mathop{\text{A}}_{e=1}^N (\mathbf{K}_e) , \quad (4.62)$$

$$\mathbf{K}_{12} = \mathop{\text{A}}_{e=1}^N (\mathbf{K}_e \mathbf{A}_e) , \quad (4.63)$$

$$\mathbf{K}_{21} = \mathop{\text{A}}_{e=1}^N (\mathbf{A}_e^T \mathbf{K}_e) , \quad (4.64)$$

$$\mathbf{K}_{22} = \mathop{\text{A}}_{e=1}^N (\mathbf{A}_e^T \mathbf{K}_e \mathbf{A}_e) . \quad (4.65)$$

Equation (4.55) can be expanded for the sake of clarity as

$$\Upsilon(\mathbf{r}, \mathbf{E}) = \frac{1}{2} \left(\mathbf{r}^T \mathbf{K}_{11} \mathbf{r} + \mathbf{r}^T \mathbf{K}_{12} \mathbf{E} + \mathbf{E}^T \mathbf{K}_{21} \mathbf{r} + \mathbf{E}^T \mathbf{K}_{22} \mathbf{E} \right) . \quad (4.66)$$

At this point the procedure introduced in the previous section can be performed. From all kinematically admissible DOFs $\tilde{\mathbf{r}}$, only such a state will take place that minimizes the potential energy (4.66)

$$\frac{\partial}{\partial \tilde{\mathbf{r}}} \Upsilon(\tilde{\mathbf{r}}, \mathbf{E})|_{\tilde{\mathbf{r}}=\mathbf{r}} = 0 . \quad (4.67)$$

Noting the symmetry of resulting matrix and the fact that $\mathbf{K}_{12} = \mathbf{K}_{21}^T$, the aforementioned minimization yields the condition

$$0 = \mathbf{K}_{11} \mathbf{r} + \mathbf{K}_{12} \mathbf{E} . \quad (4.68)$$

Hence the true state of \mathbf{u} is related to \mathbf{E} via

$$\mathbf{r} = -\mathbf{K}_{11}^{-1} \mathbf{K}_{12} \mathbf{E} . \quad (4.69)$$

Introducing Eq. (4.69) into Eq. (4.66) and differentiating with respect to \mathbf{E} leads to

$$\Sigma = \frac{1}{|\Omega|} \left(\mathbf{K}_{22} - \mathbf{K}_{21}^T \mathbf{K}_{11}^{-1} \mathbf{K}_{12} \right) \mathbf{E} , \quad (4.70)$$

which finally gives

$$\mathbf{D}_{hom} = \frac{1}{|\Omega|} \left(\mathbf{K}_{22} - \mathbf{K}_{21}^T \mathbf{K}_{11}^{-1} \mathbf{K}_{12} \right) . \quad (4.71)$$

An alternative approach is to avoid the above substitution and consider Eq. (4.68) as an additional condition, which can be understood as the Lagrange Multiplier. Then the expression of the macroscopic stress as the first derivative of Eq. (4.66) with respect to \mathbf{E} reads as

$$\Sigma = \frac{1}{|\Omega|} \left(\mathbf{K}_{21} \tilde{\mathbf{r}} + \mathbf{K}_{22} \mathbf{E} \right) . \quad (4.72)$$

Coupling the latter term with Eq. (4.68) then gives

$$\begin{Bmatrix} \mathbf{0} \\ \Sigma \end{Bmatrix} = \frac{1}{|\Omega|} \begin{bmatrix} \mathbf{K}_{11} & \mathbf{K}_{12} \\ \mathbf{K}_{21} & \mathbf{K}_{22} \end{bmatrix} \begin{Bmatrix} \tilde{\mathbf{r}} \\ \mathbf{E} \end{Bmatrix}. \quad (4.73)$$

Homogeneous stiffness matrix can be thus derived as the Schur complement of global stiffness matrix \mathbf{K}^{ex} divided by $\frac{1}{|\Omega|}$, which is equal to the solution of the second derivative of $\Upsilon(\mathbf{E})$ with respect to \mathbf{E} . The zero vector $\mathbf{0}$ on the left hand side of Eq. (4.73) can be related to the zero work done by the volume average of the perturbation DOFs.

4.3.3 Standard Finite Element method

In the case of the finite element method the procedure is similar as above. However, FEM differs in a different choice of basis functions. In the stiffness method, bases fulfil both the governing differential equation and the boundary conditions in an entire element and are zero only in a finite number of points. Basically, these represent the analytical solution to a particular quantity for unitary nodal impulses. It means that the basis functions can have larger supports than the standard finite element bases, thereby making the Stiffness method a special kind of the Ritz approximation with very special approximation functions specific to strong solutions for applied loads.

Now, assume a finite element approximation of displacement DOFs in the form

$$\mathbf{u}(\mathbf{x}) = \mathbf{N}(\mathbf{x})\mathbf{r}. \quad (4.74)$$

The displacement gradient then reads

$$\boldsymbol{\varepsilon}(\mathbf{x}) = \mathbf{B}(\mathbf{x})\mathbf{r}. \quad (4.75)$$

Considering the above approximations, the strain decomposition yields

$$\boldsymbol{\varepsilon}(\mathbf{x}) = \begin{bmatrix} \mathbf{B}(\mathbf{x}) & \mathbf{I} \end{bmatrix} \begin{Bmatrix} \mathbf{r}^* \\ \mathbf{E} \end{Bmatrix}. \quad (4.76)$$

The strain energy of the element can be computed as

$$\Upsilon_e = \frac{1}{2} \int_{\Omega_e} \begin{Bmatrix} \mathbf{r}^* \\ \mathbf{E} \end{Bmatrix}^T \begin{bmatrix} \mathbf{B}^T \mathbf{D}_e \mathbf{B} & \mathbf{B}^T \mathbf{D}_e \\ \mathbf{D}_e \mathbf{B} & \mathbf{D}_e \end{bmatrix} \begin{Bmatrix} \mathbf{r}^* \\ \mathbf{E} \end{Bmatrix} d\Omega_e. \quad (4.77)$$

Performing the very same localization as in the case of the direct stiffness approach along with the homogenization process in Eqs. (4.67-4.71) results in

$$\begin{Bmatrix} \mathbf{0} \\ \Sigma \end{Bmatrix} = \frac{1}{|\Omega|} \begin{bmatrix} \mathbf{K}_{11} & \mathbf{K}_{12} \\ \mathbf{K}_{21} & \mathbf{K}_{22} \end{bmatrix} \begin{Bmatrix} \tilde{\mathbf{r}} \\ \mathbf{E} \end{Bmatrix}. \quad (4.78)$$

Note, that the member K_{22} is equal to the so called Voight upper bound of the homogenized properties, while the remaining members can be understood as a correction [6].

4.3.4 Extracting isotropic elastic parameters from homogenized matrices

Unlike the first homogenization procedure described in Section 4.2 the latter approach yields the homogenized material stiffness matrix. If a degree of anisotropy is small, it is convenient to describe the constitutive behaviour of a homogenized material with scalar quantities such as Young's, bulk and shear moduli. This simplification leads to a priori assumption of isotropy. Although we demonstrate the intended procedure for planar problems, it is applicable with a minor extension to a general three-dimensional isotropy.

Energy based extraction

The first method arises from the homogenization approach adopted in Section 4.2. Assume homogeneous stiffness matrix of 3×3 elements for a planar problem (e.g. plane strain) and the Hooke's law in the form

$$\begin{Bmatrix} \sigma_x \\ \sigma_y \\ \tau_{xy} \end{Bmatrix} = \begin{bmatrix} D_{11} & D_{12} & D_{13} \\ D_{21} & D_{22} & D_{23} \\ D_{31} & D_{32} & D_{33} \end{bmatrix} \begin{Bmatrix} \varepsilon_x \\ \varepsilon_y \\ \gamma_{xy} \end{Bmatrix}. \quad (4.79)$$

The elastic strain energy density v of a homogenized RVE Ω , understood as an infinitesimal macroscopic material point loaded by an arbitrary strain vector ε , reads as

$$v = \frac{1}{2} \varepsilon^T \mathbf{D}_{hom} \varepsilon. \quad (4.80)$$

Considering the Ω isotropic (4.22), the above equation equals v of an isotropic material in the form

$$v = \frac{1}{2} K \varepsilon_V^2 + G \varepsilon_D^T \varepsilon_D. \quad (4.81)$$

Assuming a unitary deviatoric strain $\varepsilon = \{0, 0, 1\}^T$ substituted to Eq. (4.80) and comparing the two latter equations directly gives

$$G = D_{33}. \quad (4.82)$$

On the other hand, if the strain vector is assumed such that it yields a unitary volumetric strains, for instance $\varepsilon = \{\frac{1}{2}, \frac{1}{2}, 0\}^T$, it results in

$$K = \frac{1}{4} (D_{11} + D_{12} + D_{21} + D_{22}). \quad (4.83)$$

Engineering parameters such as Young's modulus E and Poisson's ratio ν can be calculated [53] as

$$\nu = \frac{3K - 2G}{6K + 2G}, \quad E = \frac{9KG}{3K + G}. \quad (4.84)$$

Least square method extraction

The previous approach explicitly assumes isotropic material so that it neglects members D_{i3} and D_{3i} even if they are non-zero. In order to account for these components the spectral analysis of the stiffness matrix can be performed and effective parameters determined from the eigenvalues. For a comprehensive discussion on this topic, see Appendix A.

Considering the plane strain conditions, the material stiffness matrix takes the following form

$$\mathbf{D}_{hom}^{(K,G)} = \begin{bmatrix} K + \frac{4}{3}G & K - \frac{2}{3}G & 0 \\ K - \frac{2}{3}G & K + \frac{4}{3}G & 0 \\ 0 & 0 & G \end{bmatrix}. \quad (4.85)$$

Eigenvalues of the above stiffness matrix are

$$\lambda^{(K,G)} = \left\{ \begin{array}{c} G \\ 2G \\ \frac{2}{3}G + 2K \end{array} \right\}. \quad (4.86)$$

Regarding the overall stiffness matrix obtained from the macroscopic degrees of freedom's homogenization approach does not exactly obey the form of Eq. (4.85), nor the calculated eigenvalues λ_{cal} are in relations (4.86). Therefore the Least square method was employed to adjust the effective elastic properties given by the latter equation.

As the stiffness matrix $\mathbf{D}_{hom}^{(K,G)}$ takes relatively simple algebraic form, unlike if we would assume the stiffness matrix expressed in terms of E and ν , the eigenvalues $\lambda^{(K,G)}$ can be written as the linear combination of parameters K and G

$$\lambda^{(K,G)} = \begin{bmatrix} 1 & 0 \\ 2 & 0 \\ \frac{2}{3} & 2 \end{bmatrix} \begin{Bmatrix} G \\ K \end{Bmatrix}. \quad (4.87)$$

For the sake of clarity we abbreviate the expression (4.87) as

$$\lambda^{(K,G)} = \mathbf{A} \mathbf{d}. \quad (4.88)$$

The least square method applied to Eq. (4.87) results in minimizing the Euclidean L^2 -norm $\|\lambda^{(K,G)} - \lambda_{cal}^{(K,G)}\|$. It can be rewritten as

$$\|\lambda^{(K,G)} - \lambda_{cal}^{(K,G)}\| = \left(\lambda^{(K,G)} - \lambda_{cal}^{(K,G)} \right)^T \left(\lambda^{(K,G)} - \lambda_{cal}^{(K,G)} \right). \quad (4.89)$$

Substituting Eq. (4.87) into Eq. (4.89) yields

$$\|\mathbf{Ad} - \lambda_{cal}^{(K,G)}\| = \left(\mathbf{Ad} - \lambda_{cal}^{(K,G)}\right)^T \left(\mathbf{Ad} - \lambda_{cal}^{(K,G)}\right). \quad (4.90)$$

Minimizing Eq. (4.90) with respect to \mathbf{d}

$$\min_{\mathbf{d}} \|\mathbf{Ad} - \lambda_{cal}^{(K,G)}\|, \quad (4.91)$$

is equal to solving the equation

$$\frac{\partial}{\partial \mathbf{d}} \left(\mathbf{Ad} - \lambda_{cal}^{(K,G)}\right)^T \left(\mathbf{Ad} - \lambda_{cal}^{(K,G)}\right) = 0, \quad (4.92)$$

which yields the criterion (objective function)

$$2\mathbf{A}^T \mathbf{Ad} - 2\mathbf{A}^T \lambda_{cal}^{(K,G)} = 0. \quad (4.93)$$

Albeit the matrix \mathbf{A} is non-square, $\mathbf{A}^T \mathbf{A}$ gives the square matrix, for which the inverse exists. Thus the parameters K and G can be approximated with the Least square method as

$$\mathbf{d} = \begin{Bmatrix} G \\ K \end{Bmatrix} = \left(\mathbf{A}^T \mathbf{A}\right)^{-1} \mathbf{A}^T \lambda_{cal}^{(K,G)}. \quad (4.94)$$

Evaluating (4.94) gives

$$\begin{Bmatrix} G \\ K \end{Bmatrix} = \begin{bmatrix} \frac{1}{5} & \frac{2}{5} & 0 \\ -\frac{2}{30} & -\frac{4}{30} & \frac{1}{2} \end{bmatrix} \lambda_{cal}^{(K,G)}. \quad (4.95)$$

It is worthwhile to note, that when performing numerical computation of eigenvalues of a given stiffness matrix, the result is a sorted sequence of numbers. Therefore it should be ensured that the largest eigenvalue corresponds to $\frac{2}{3}G + 2K$ and not to $2G$. This requirement leads to the condition of positive Poisson's ratio, thereby making the above procedure valid for non-auxetic materials only. If $\nu < 0$ the last two rows of \mathbf{A} has to be swaped.

Applying the above procedure in plane stress conditions we arrive at

$$\mathbf{D}_{hom}^{(K,G)} = \begin{bmatrix} \frac{4G(G+3K)}{4G+3K} G & \frac{-2G(2G-3K)}{4G+3K} & 0 \\ \frac{-2G(2G-3K)}{4G+3K} & \frac{4G(G+3K)}{4G+3K} G & 0 \\ 0 & 0 & G \end{bmatrix}, \quad (4.96)$$

with the eigenvalues

$$\lambda^{(K,G)} = \begin{Bmatrix} G \\ 2G \\ \frac{18KG}{4G+3K} \end{Bmatrix}. \quad (4.97)$$

Since the relation between the eigenvalues and the elastic parameters is non-linear, the non-linear variant of the least squares method has to be applied resulting in an iterative process.

Chapter 5

Homogenization of Alporas[®] closed-cell foam

Porous metals represent a branch of materials with overall properties, which are highly influenced by the microstructure composition [54]. A proper microstructure design can thus render materials with properties specific to their application. Cellular metals feature very attractive combination of relatively high stiffness with respect to low weight and ability of high energy absorption. In the case of open-cell microstructure, metal foams can serve as filters, heat conductors or exchangers, while in the case of its closed-cell counterpart, vibration, sound absorption or fire protection govern another applications [55, 56].

A great interest arises from the car and aircraft industries, where cellular metals seem to be a hoped-for way to reduce weight mirrored in less fuel consumption while preserving stiffness of structural members and improving energy absorption of safety zones or heat dissipation ability of engine blocks [55]. Microporous metals could replace commonly used and expensive honeycomb structures. However, possible applications are not limited to Mechanical Engineering. In Civil Engineering, cellular metals can serve as self-supported sound barriers in noisy areas, fire resistance allows the materials to be used as tunnel lining insulators, etc. [55, 56].

From the perspective of Materials Engineering porous materials represent an extreme case of a composite with an infinite contrast of phases' properties. That is why the classical asymptotic homogenization bounds are far apart and the influence of inner structure is maximized [54]. Characterization of the material behaviour based on porosity and properties of solid phase is insufficient.

As was mentioned, cellular metals can be divided into two distinct categories, namely open-cell and closed-cell variant [56]. Both cases are usually referred to as foams, but as Banhart pointed out [55] only the closed-cell porous metals should be denoted as foams. For the open-cell variant a sponge would be the correct denomination. The inner composition is determined by manufacturing process, alternatively post-processing (Alporas foams can be rolled in order to collapse cell walls and increase frequency range of sound absorption). The complex description of these processes can be found in [55, 56].

There is a consensus on the behaviour (or at least its approximation) models,

open-cell sponges are usually modelled as spatial wired models consisting of beams, while closed-cell foam might require the addition of membrane elements among the beams acting as the cell walls [57]. Nevertheless, in the case of very thin walls even the behaviour of closed-cell foams can be approximated with beam models [55, 54, 56, 58]. Based on this assumption, Ashby and Gibson presented the spatial unit cell model [57] and derived equations relating porosity with various thermo-mechanical parameters.

The idea of porous materials is not purely artificial. Microcellular compositions are ubiquitous in nature (e.g. bones and wood [55]), thus verified by thousands of years in operation. Some of the current metal foams can mimic wood and substitute wood material prone to biodegradation [56]. The production of cellular metals was preceded by polymers which are easier to manufacture. Interestingly, life cycle of industrial use of cellular metal follows the curve introduced by Ashby [56]. The industrial take-up followed the main research interest with a delay of more than twenty years. According to [55], first porous metal samples were manufacture in 60's and 70's but the mass production started in mid 80's.

The current chapter of the thesis was motivated by the paper of Němeček et al. [59]. In the paper, nanoindentation and macroscopic experiments were compared with the two-scale numerical homogenization results. The coarse-scale homogenization was performed on a Voronoi mesh arising from an optical scan image of a material cross-section. The RVE size was therefore limited by the size of the image. The aim is to compress the microstructural information within the set of Wang tiles and reconstruct computational models of arbitrary sizes in order to arrive at homogenized properties independent of the RVE size.

5.1 Alporas[®] foam

The material to be homogenized is the closed-cell aluminium foam Alporas[®] manufactured by Shinko Wire Company, Ltd.[60]. Alporas[®] can be characterised as a highly porous microcellular metal with the average size of cells (pores) 4.5 mm [60]. The main field of application of Alporas[®] foam lies in sound absorption, e.g. sound absorption panels coating the bottom side of motorway bridges as has been reported in [56] and references therein. Ashby, in her Design guide [56], declares properties of Alporas[®] foam stated in Tab. 5.1.

Table 5.1: Properties of Alporas[®] foam

| | |
|-----------------|----------------|
| porosity | 90 - 92 % |
| Young's modulus | 0,4 - 1,0 GPa |
| Shear modulus | 0,3 - 0,35 GPa |
| Bulk modulus | 0,9 - 1,2 GPa |
| Poisson's ratio | 0,31 - 0,32 |

Alporas[®] foam is manufactured by a batch casting process with an addition of a blowing agent into the aluminium molten. When the blowing agent, in particular

the titanium dihydrate TiH_2 , is heated up, it releases hydrogen, thereby creating bubbles within the molten. To prevent the bubbles from popping up to the surface the viscosity of molten is increased with the calcium thickening agent in amount of approximately 1,5 % of molten weight. With a precise control of time, pressure, temperature, amount of the added blowing agent and the calcium thickener the foam characteristics can be controlled [60].

As a consequence of high porosity, Alporas[®] loses the sphere shape of pores, the pores turn into polyhedra with the bulk material concentrated to the vertices, cell walls then exhibit a plateau in the middle [60].

5.2 Numerical homogenization

The bulk material of the Alporas[®] foam is also non-homogeneous, namely due to the agent additives. Based on Environmental Scanning Electron Microscope (ESEM) images and nanoindentation Němeček et al. reported two distinct phases within the ligaments [59], the aluminium rich phase, and the phase consisting of a significant amount of titanium and calcium. Homogenization at this level was performed by Němeček et al. and values of effective Young's modulus $E = 70.083$ GPa and Poisson's ratio $\nu = 0,35$ were determined by means of analytical micromechanics (Mori-Tanaka method). For further details be referred to [59].

Those values were taken as inputs for the upper-scale homogenization process, in which the microstructure was represented by a wired model consisting of straight beams. The geometry of the wired model was obtained by Voronoi tessellation. The centres of gravity of individual pores were taken as seeds for the Voronoi diagram. As mentioned above, the size of the wired model was limited with the size of the scanned image, which was the initial motivation to employ the tiling concept, which, once again, allows computational domains of arbitrary sizes to be generated.

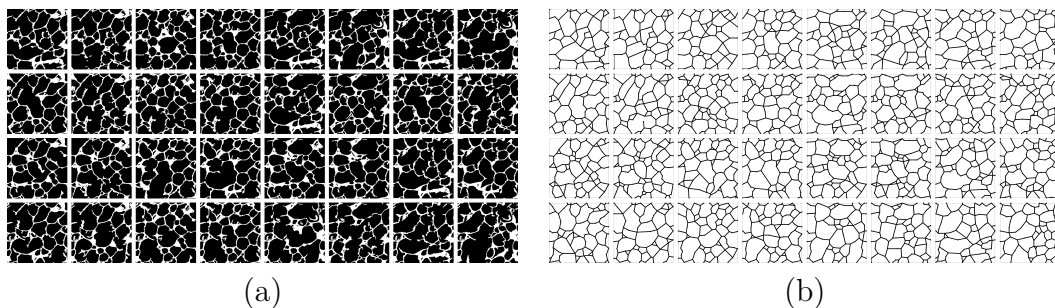


Figure 5.1: Compressed Alporas[®] microstructure W32/4-4: (a) graphical representation, (b) corresponding wired model

The same reference microstructure as was used in [59], see Fig. 5.4(a), was subjected to the homogenization procedures introduced above. Making use of the sensitivity analysis presented in Section 3.4 the microstructural information was compressed within the set of W32/4-4.

The volume fraction of the bulk material obtained from the weighing test of the real specimen does not correspond to fraction of the area of ligaments in the

reference image. The discrepancy can be particularly attributed to the preparation procedure, in which the saw cut was not perpendicular to most of the pore walls. Therefore the apparent ligament fraction is higher than the measured one. For this reason a wired model was preferred to the planar finite element analysis as the latter would have required a topological modification in order to achieve the measured volume fraction. Moreover, the fact that the spatial beam model has been reported many times, e.g. [57, 56, 58], was convincing as well.

The geometry of each tile was manually meshed employing a specifically designed, Graphical User Interface (GUI) tool, which was programmed in Matlab environment. The graphical interface of the tool is shown in Fig. 5.3. The tool enables to maintain the mesh compatibility across the adjacent edges. Despite the fact, that the manual meshing is a tedious work, it allows for correcting faults, such as disrupted ligaments, which inevitably result from the automatic tile design of such complex microstructure or may be inherited from the preparation of the reference sample that involved saw cutting and polishing. The compressed microstructure and the corresponding wired model are depicted in Fig. 5.1.

Computational domains are generated from meshes defined in tiles. The parametric local coordinates of the tile mesh nodes are transformed to the global coordinates by translation and linear scaling. Subsequently, the coincident points of adjacent tiles are identified on congruent edges and merged. Finally, all nodes are renumbered. This procedure is illustrated in Fig. 5.2.

The same procedure as in [59] was adopted for determining the cross-section parameters. The beams are assumed straight and prismatic with a rectangular cross-section of unitary width. The total length of beams is given by the mesh geometry, hence the height of the cross-section is governed by the experimentally obtained volume fraction of the ligament phase. Thus the relation for the height reads as

$$H = \frac{\rho|\Omega|}{L_{\Sigma}}, \quad (5.1)$$

where ρ stands for the measured volume fraction, $|\Omega|$ denotes the size of the tile domains and L_{Σ} is the total length of beams.

As the width is assumed unity, the expressions for the cross-section area A and the moment of inertia I yields

$$A = H, \quad (5.2)$$

$$I = \frac{1}{12}H^3. \quad (5.3)$$

The reported value 8.6% of the ligament fraction [59] resulted in cross-section characteristics denoted in Tab. 5.2.

In order to analyse the effect of the geometry, the microstructure has been represented also with the Voronoi mesh and the mesh that has been manually created in the GUI tool by making use of the reference image in Fig. 5.4(a). The visual appearance of various geometries can be compared in Fig. 5.4. The beam characteristics for these representations were derived in the same manner as for the tiling-based geometry. The obtained values are stated in Tab. 5.2. The height of beams is

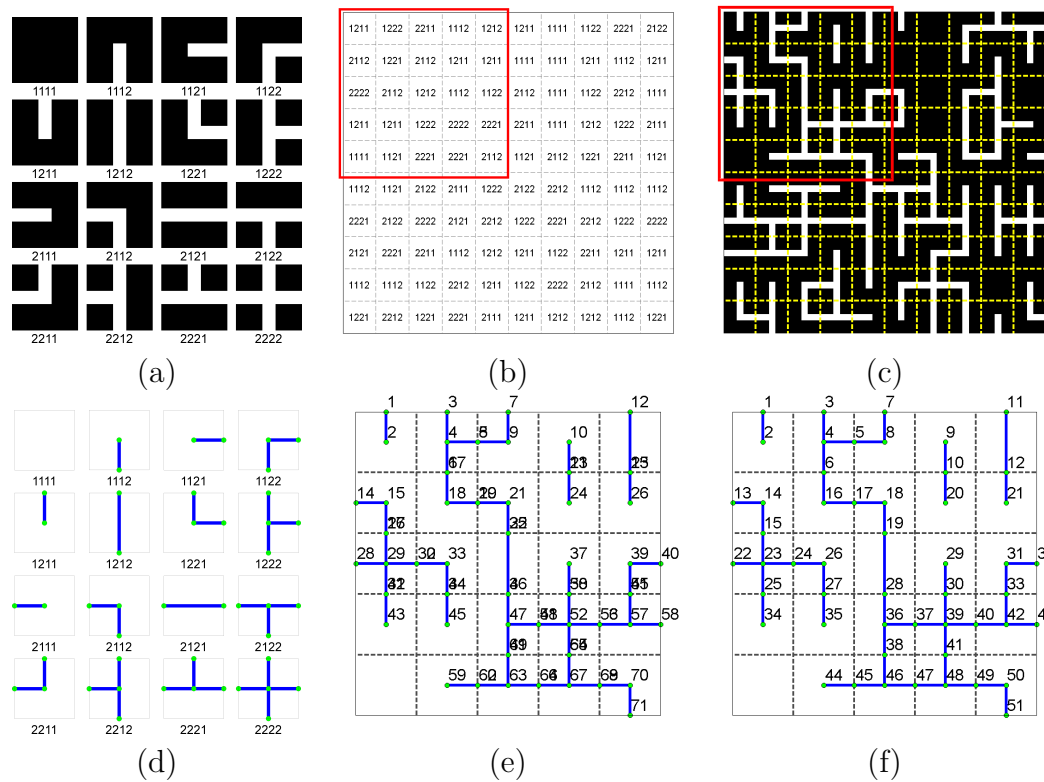


Figure 5.2: Illustration of domain generation: (a) example of compressed system W16/2-2, (b) tiling map consisting of 10×10 tiles, (c) reconstructed system according to (a) and (b), (d) FE mesh in compressed system W16/2-2, (e) corresponding FE mesh in highlighted portion of tiling map (b), (f) FE mesh in highlighted portion (merged and renumbered nodes)

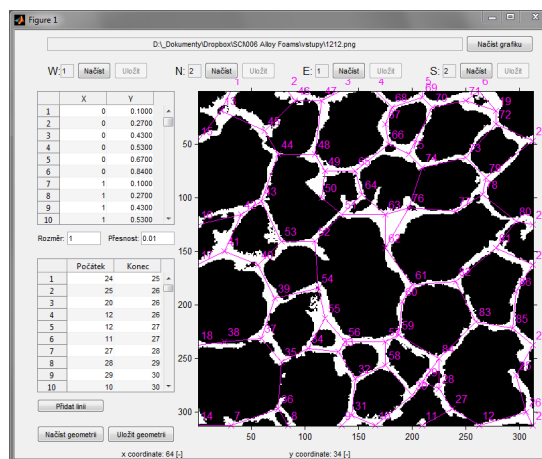


Figure 5.3: In-house designed tool to aid manual meshing of Wang tiles

approximately 10% less for the tiling-based geometry than for the remaining two. This can be attributed to the automatic tile design and corrections that were made during the manual meshing resulting in a greater total length of beams and hence lower height.

Table 5.2: Beam cross-section characteristics

| | | Voronoi mesh | Real geometry mesh | Tiling-based mesh |
|---|-------------------|--------------|--------------------|-------------------|
| A | [m ²] | 1.431e-04 | 1.469e-04 | 1.3170e-04 |
| I | [m ⁴] | 2.443e-13 | 2.643e-13 | 1.9038e-13 |

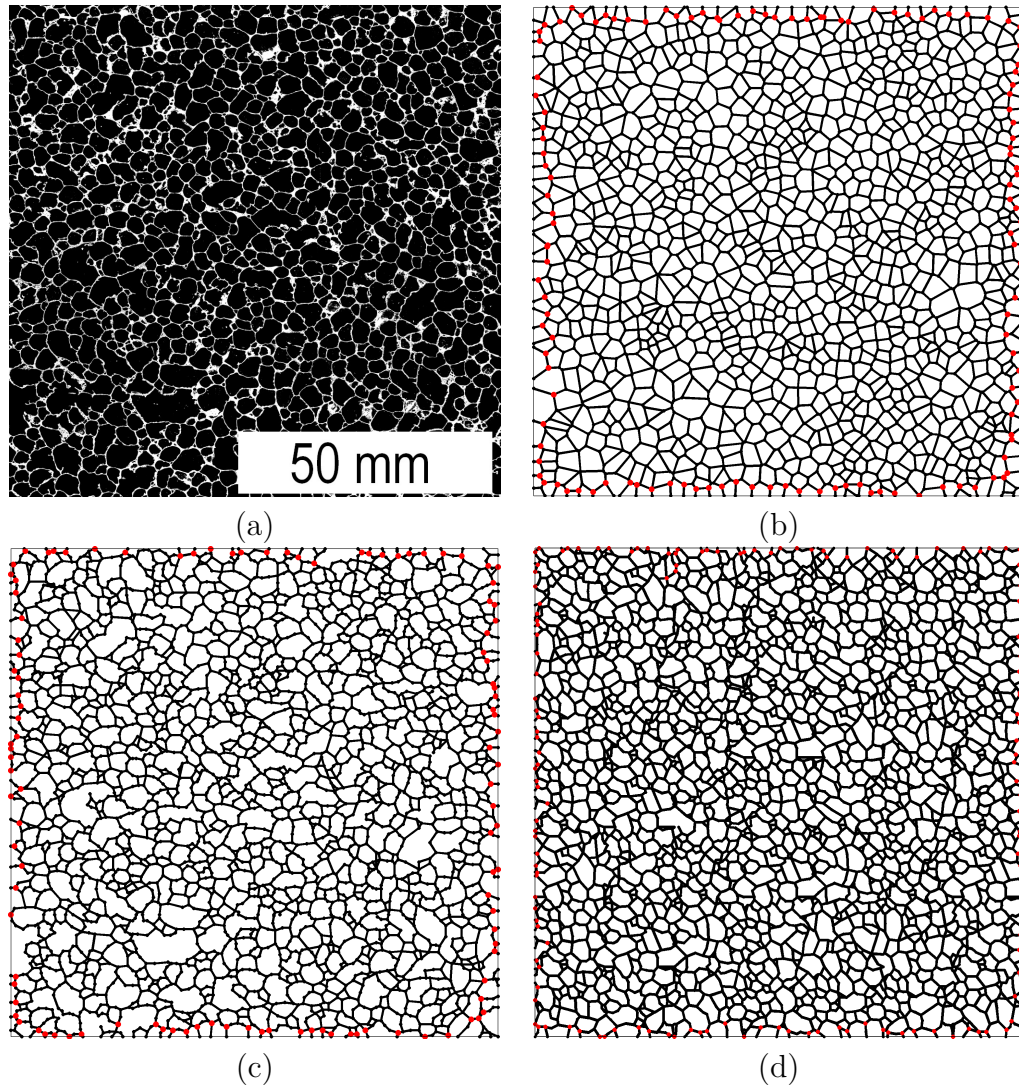


Figure 5.4: Comparison of geometrical representation with reference microstructure: (a) scanned image of cross-section of Fig. 1.1(b), courtesy of Jiří Němeček [59], (b) Voronoi mesh, (c) real geometry, (d) tiling-based representation (scale does not exactly corresponds to (a) due to fixed tile dimensions)

For the numerical homogenization the data of the real-shaped geometry were chosen as the representation which resembles the reference microstructure the most. This should result in a stiffer response of the microstructure, nevertheless due to the linear behaviour of the model the results are expected to differ only by the factor of the input parameters ratio.

Prescribed displacements were imposed at the support nodes. Considering the boundary nodes as supports leads to unrealistic excessive deformations of adjacent beams. For this reason a script performing topological survey was programmed. The algorithm identifies nodes at the boundary of the computational domain and follows the adjacent beams until it reaches a node that belongs to more than two beams. The procedure is illustrated in Fig. 5.5. The support nodes are marked in red in Fig. 5.4.

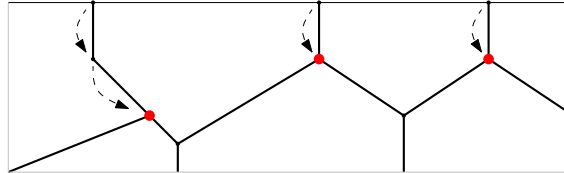


Figure 5.5: Illustration of support search algorithm

All the calculations were implemented in Matlab environment. It turned out that large computational domains are necessary to capture the convergence of the overall elastic constants. Therefore, the code was optimized by making use of the sparsity and the symmetry of the stiffness matrix and by reducing all repetitive processes.

5.3 Results

The two homogenization strategies outlined in Chapter 4 were employed. The homogenized properties of all three geometric representation are given in Tab. 5.3. The size of the tiling-based domains varied from 5×5 to 55×55 tiles. For each tiling size, ten realizations were generated. The relation between values of the homogenized elastic parameters and the size of the computational domain is depicted in Fig. 5.6.

As the kinematic uniform boundary conditions (KUBC) were prescribed, the computed values should represent upper bounds [61]. This complies with the convergence character of the graphs in Fig. 5.6. Note that the homogenization procedure based on energetic reasoning and the approach involving the macroscopic degrees of freedom along with the isotropy assumption coincide as expected. From Tab. 5.3, the tiling representation seems to be stiffer than the real-shaped geometry despite the fact that the real-shaped geometry domain is significantly smaller. This is because the stiffer cross-section parameters of the real-shaped geometry were assumed also for the tiling representation. If the characteristics from Tab. 5.2 were used, the homogenized properties would be $K \approx 100\text{MPa}$, $E \approx 40\text{MPa}$ and $G \approx 14\text{MPa}$, hence the real-shaped geometry response would be stiffer as expected.

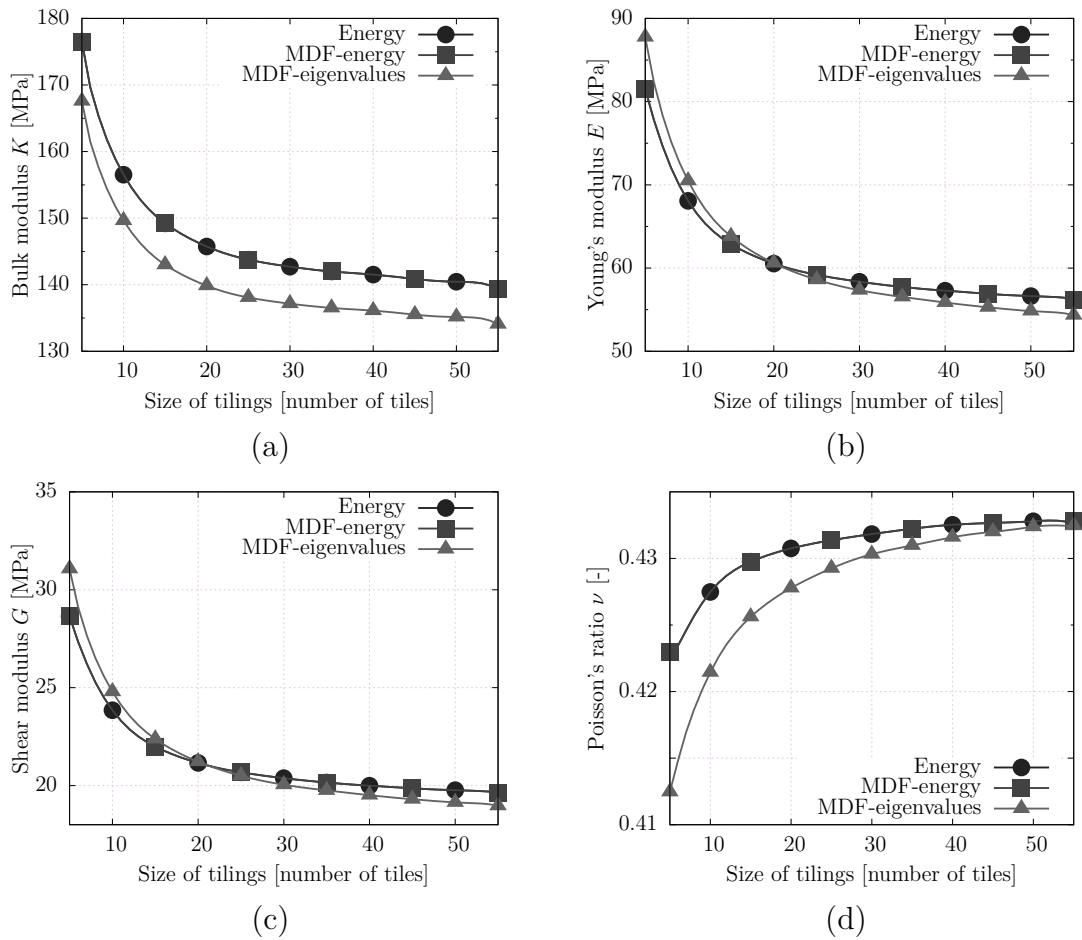


Figure 5.6: Relationship between homogenized elastic parameters and dimensions of computational domains: (a) Bulk modulus K , (b) Young's modulus E , (c) Shear modulus G , (d) Poisson's ratio ν

5.4 Discussion and conclusions

Based on Fig. 5.6, it seems that RVE should be about hundreds of the characteristic pore diameter length in dimensions. This finding corresponds with [15] regarding the minimal size of RVE in the case of infinite contrast of phase properties. On the other hand, it contradicts the recommendation of Ashby et al. [56] that proposes RVE size of approximately seven times the mean of pore diameters. However, this recommendation is given for three-dimensional samples and thus it does not need to be valid for the planar case.

Comparing the homogenized results with the reference values reported by Ashby et al. [56], see Tab. 5.1 and Tab. 5.3, leads to an unambiguous conclusion. Despite the fact, that the aptness of the spatial wired model has been reported several times [56, 57, 58], it can be conjectured that planar beam representation due to Němeček et al. [59] has a limited capability in predicting the complex behaviour of Alporas[®] foam. Possibly, it lacks the stiffness contribution from the out-of-plane beams and membranes of cell walls parallel to the investigated plane. However,

Table 5.3: Homogenization results

| | | K | E | G | ν |
|---------|---------------------|----------|--------|--------|--------|
| | | [MPa] | [MPa] | [MPa] | [-] |
| Voronoi | Energy | 1291.647 | 86.840 | 29.165 | 0.489 |
| | MDF-Energy | 1291.647 | 86.840 | 29.165 | 0.489 |
| | MDF-LSQ | 1280.910 | 95.839 | 32.214 | 0.488 |
| Real | Energy | 92.066 | 48.193 | 17.056 | 0.413 |
| | MDF-Energy | 92.066 | 48.193 | 17.056 | 0.413 |
| | MDF-LSQ | 87.048 | 55.349 | 19.852 | 0.394 |
| Tiling | Energy μ | 140.099 | 56.657 | 19.774 | 0.433 |
| | Energy σ | 0.879 | 0.238 | 0.087 | 0.0005 |
| | MDF-Energy μ | 140.099 | 56.657 | 19.774 | 0.433 |
| | MDF-Energy σ | 0.879 | 0.238 | 0.087 | 0.0005 |
| | MDF-LSQ μ | 134.843 | 54.498 | 19.020 | 0.433 |
| | MDF-LSQ σ | 0.848 | 0.222 | 0.079 | 0.0004 |

the membrane contribution of cell walls was reported negligible in the case of high- porosity foams [58].

The analysis of the geometry influence clearly shows that the Voronoi mesh leads to the overestimated value of the bulk modulus. Assuming only volumetric deformation the axial stiffness of beams is dominant contribution in the case of Voronoi mesh whereas in the case of real geometry axial and bending stiffness contribute equally. This explains the result of Němeček et al. [59] as they considered only the volumetric load case. They assumed near zero Poisson's ratio (based on their experimental observations) which allowed them to declare the apparent oedometric moduls to be the homogenized Young's modulus. However, if the whole homogenization procedure was performed they would arrive at similar results as in Tab. 5.3. Moreover, the zero Poisson's ratio is in contradiction with the characteristics reported in [56], see Tab. 5.1. The above mentioned facts along with the limited size of the Voronoi mesh, which corresponds to a 4×4 tiling in Fig. 5.6, rise a question of validity of the computational model proposed in [59] for predicting the effective elastic properties of Alporas[®] foam.

Summary

The topic of microstructure representation along with the common two-point spatial statistics have been presented in Chapter 1. This chapter also contains a procedure for computing $C_2(\mathbf{x})$ statistics based on the flood-fill algorithm and the Fourier transform. A Matlab tool with GUI was programmed to compute microstructure characteristics, Fig. 1.4. Some observations regarding interpretation of higher order descriptors are stated in Section 1.1.5.

The motivation behind the original idea of Wang tiles is outlined in the second chapter. A historical development of the aperiodic tile sets is presented and the construction of the smallest aperiodic sets of Culik and Kari is described. A description of tiling a plane with those sets is provided. The concept of stochastic tile sets and its extension to the third dimension by means of Wang cubes is presented.

The third chapter investigates the potential of the automatic tile morphology design. Modified Image Quilting and Labyrinth algorithm, an alternative to the original Image Quilting algorithm, are proposed and investigated. The enhancement of the periodicity reduction by adopting the concept of tile patches is quantified by means of secondary extremes in $S_2(\mathbf{x})$ and reported in Section 3.2. A sensitivity analysis of the automatic design was performed, the objective of the analysis was to determine the optimal values of the design inputs such that the compressed microstructure arising from those inputs would contain maximum microstructural information of the reference microstructure and yet be small enough to be practical for further utilization. The comparison of the compressed and the reference microstructures was quantified by means of the spatial statistics presented in the first chapter, namely the volume fraction ϕ , the two-point probability $S_2(\mathbf{x})$ and the normalized two-point cluster $\hat{C}_2(\mathbf{x})$ functions.

From the analysis we can conclude that the width of the overlapping region equal to approximately six times the mean inclusion size was suitable for all four investigated microstructures. No other general rule regarding the input values was observed, thus an analogous sensitivity study is recommended if compression based on Wang tilings is desired. From the results it seems that the Labyrinth algorithm performs better only for the case of microstructure with loosely packed identical inclusions.

Two distinct homogenization strategies are presented in Chapter 4. The first approach is based on energetic assumptions comparing the strain energy density of homogeneous media and strain energy of the discrete beam model. The second approach is based on the idea of macroscopic degrees of freedom resulting in formulation of extended global stiffness matrix of the FE problem. The homogenized

stiffness matrix is then computed directly as the Schur complement of the extended global stiffness matrix.

An application of the tiling concept is illustrated in Chapter 5 with homogenization of elastic properties of Alporas[®] foam. The microstructure was compressed within the set of Wang tiles making use of the outcomes from the sensitivity analysis, Section 3.4. The microstructure was represented with wired model consisting of uniform beams with cross-section characteristics obtained in the same manner as in [59]. The tiling concept allowed the study of the necessary RVE size. Both homogenization methods introduced in Chapter 4 were applied and compared. The results of the homogenization contradict the conclusions of [59], the size of RVE was found to be about hundreds multiples of the mean inclusion diameter, values of homogenized elastic properties differ from the reported values by two-orders of magnitude. Therefore the model proposed in [59] seems to be incapable to represent the Alporas[®] foam.

Despite the latter, rather, negative conclusion Wang tiling proved to be very efficient tool for microstructure compression. The potential of the tiling is not limited to effective computational domain generation and investigation of the appropriate size of RVE. As was mentioned, domain decomposition strategies benefiting from the repetitive nature of a tiling may enhance computational performance of analyses based on tiled domains. Moreover, microstructure-informed enrichment functions can be formulated on a similar basis as well [8].

Appendix A

Isotropic stiffness matrices

For the sake of keeping the thesis self-contained the spectral properties of stiffness matrices for a linear isotropic material are stated in this section. Relations between characteristic vectors and eigenvalues are derived. If not stated otherwise engineering notation is denoted by curly brackets for vectors (stress and strain vectors) and square brackets for matrices (stiffness or compliance matrix). Tensors are written in bold face font and individual components are denoted with lower case indices.

Starting with the Hooke's law for one dimensional problem

$$\sigma = E\varepsilon, \quad (\text{A.1})$$

where E is Young's modulus, we write for its inverse

$$\varepsilon = \frac{1}{E}\sigma. \quad (\text{A.2})$$

Contrary to (A.2), in multiple dimensions the strain in a principal direction is constrained by transversal stresses, which yields

$$\varepsilon_{ii} = \frac{1}{E}\sigma_{ii} - \nu\frac{1}{E}\sigma_{jj} - \nu\frac{1}{E}\sigma_{kk}. \quad (\text{A.3})$$

Furthemore, for a linear isotropic material the relation coupling shear stress and strain reads as

$$\tau_{ij} = G\gamma_{ij}, \quad (\text{A.4})$$

where G stands for the shear modulus.

Thus the inverse of the Hooke's law for three dimensions reads as

$$\begin{bmatrix} \varepsilon_x \\ \varepsilon_y \\ \varepsilon_z \\ \gamma_{yz} \\ \gamma_{xz} \\ \gamma_{xy} \end{bmatrix} = \frac{1}{E} \begin{bmatrix} 1 & -\nu & -\nu & 0 & 0 & 0 \\ -\nu & 1 & -\nu & 0 & 0 & 0 \\ -\nu & -\nu & 1 & 0 & 0 & 0 \\ 0 & 0 & 0 & 2(1+\nu) & 0 & 0 \\ 0 & 0 & 0 & 0 & 2(1+\nu) & 0 \\ 0 & 0 & 0 & 0 & 0 & 2(1+\nu) \end{bmatrix} \begin{bmatrix} \sigma_x \\ \sigma_y \\ \sigma_z \\ \tau_{yz} \\ \tau_{xz} \\ \tau_{xy} \end{bmatrix}, \quad (\text{A.5})$$

which can be recast to compact

$$\{\varepsilon\} = [\mathbf{C}] \{\sigma\}, \quad (\text{A.6})$$

where $[\mathbf{C}]$ is the compliance matrix.

Inverting Eq. (A.6) results in the classical form of the Hooke's law

$$\{\sigma\} = [\mathbf{D}] \{\varepsilon\}, \quad (\text{A.7})$$

where stiffness matrix $[\mathbf{D}]$ has the following form

$$[\mathbf{D}] = \frac{E}{(1-2\nu)(1+\nu)} \begin{bmatrix} 1-\nu & \nu & \nu & 0 & 0 & 0 \\ \nu & 1-\nu & \nu & 0 & 0 & 0 \\ \nu & \nu & 1-\nu & 0 & 0 & 0 \\ 0 & 0 & 0 & \frac{1-2\nu}{2} & 0 & 0 \\ 0 & 0 & 0 & 0 & \frac{1-2\nu}{2} & 0 \\ 0 & 0 & 0 & 0 & 0 & \frac{1-2\nu}{2} \end{bmatrix}. \quad (\text{A.8})$$

Spectral analysis of the stiffness matrix Eq. (A.8) gives the following eigenvalues λ^i and the related eigenvectors $\{v^i\}$

$$\begin{aligned} \lambda^1 &= \frac{E}{1-2\nu} = 3K, & \{v^1\} &= \{1 \ 1 \ 1 \ 0 \ 0 \ 0\}^T, \\ \lambda^2 &= \frac{E}{\nu+1} = 2G, & \{v^2\} &= \{-1 \ 1 \ 0 \ 0 \ 0 \ 0\}^T, \\ \lambda^3 &= \frac{E}{\nu+1} = 2G, & \{v^3\} &= \{-1 \ 0 \ 1 \ 0 \ 0 \ 0\}^T, \\ \lambda^4 &= \frac{E}{2(\nu+1)} = G, & \{v^4\} &= \{0 \ 0 \ 0 \ 1 \ 0 \ 0\}^T, \\ \lambda^5 &= \frac{E}{2(\nu+1)} = G, & \{v^5\} &= \{0 \ 0 \ 0 \ 0 \ 1 \ 0\}^T, \\ \lambda^6 &= \frac{E}{2(\nu+1)} = G, & \{v^6\} &= \{0 \ 0 \ 0 \ 0 \ 0 \ 1\}^T. \end{aligned} \quad (\text{A.9})$$

Sometimes, it is more convenient to work with stiffness matrices expressed in terms of bulk modulus K and shear modulus G . It results in a more conceivable form of stiffness matrix and straightforward interpretation of eigenvalues. Recall the strain decomposition into the volumetric and the deviatoric part

$$\varepsilon = \frac{1}{3}\varepsilon_V \mathbf{1} + \varepsilon_D \quad (\text{A.10})$$

and related stress decomposition by means of the mean stress σ_m and deviatoric stress tensor σ_D

$$\sigma = \sigma_m \mathbf{1} + \sigma_D. \quad (\text{A.11})$$

It holds

$$\sigma_m = K\varepsilon_V, \quad (\text{A.12})$$

and

$$\boldsymbol{\sigma}_D = 2G\boldsymbol{\varepsilon}_D. \quad (\text{A.13})$$

The Hooke's law then reads as

$$\boldsymbol{\sigma} = K\varepsilon_V\mathbf{1} + 2G\boldsymbol{\varepsilon}_D. \quad (\text{A.14})$$

Using the latter expression recast to maintain Eq. (A.7) gives the stiffness matrix [D] as

$$[\mathbf{D}] = \begin{bmatrix} K + \frac{4}{3}G & K - \frac{2}{3}G & K - \frac{2}{3}G & 0 & 0 & 0 \\ K - \frac{2}{3}G & K + \frac{4}{3}G & K - \frac{2}{3}G & 0 & 0 & 0 \\ K - \frac{2}{3}G & K - \frac{2}{3}G & K + \frac{4}{3}G & 0 & 0 & 0 \\ 0 & 0 & 0 & G & 0 & 0 \\ 0 & 0 & 0 & 0 & G & 0 \\ 0 & 0 & 0 & 0 & 0 & G \end{bmatrix}. \quad (\text{A.15})$$

Note that the meaning of the eigenvalues (stated in the second column in (A.9)) of the latter matrix are the same as for the matrix (A.8), it only appears to be more evident. The first eigenvector represents the three times the unitary volumetric deformation and is related to the largest eigenvalue of $3K$. The following two eigenvectors $\{\mathbf{v}^2\}$ and $\{\mathbf{v}^3\}$ represent the bi-axial excitation, one in pressure, other in tension, which results in the zero volumetric strain and yields twice the unitary deviatoric strain, see Fig. A.2(b). Therefore the corresponding eigenvalues are $2G$. The last three eigenvectors representing a consecutive unitary shear deformation in three perpendicular planes are connected with shear modulus G .

The relation between Young's and shear moduli. Relation between Young's modulus E and shear modulus G can be derived from the following example. Let assume an infinitesimal material point subjected to the stress load $\{\boldsymbol{\sigma}\} = \{-\hat{\sigma}, \hat{\sigma}, 0\}$ in the x - y coordinate system. The same load case can be described in the x' - y' coordinate system rotated by $\pi/4$ with the stress vector $\{\boldsymbol{\sigma}'\} = \{0, 0, \hat{\sigma}\}$, see Fig. A.1. This yields from the transformation rule, which can be visualized with the Mohr's circle, Fig. A.2(a). Since only the description of the stress state has changed, the strain energy density

$$v = \{\boldsymbol{\sigma}\}\{\boldsymbol{\varepsilon}\}^T \quad (\text{A.16})$$

must be the same for both cases, i.e. $v = v'$. Considering Eq. (A.3) and (A.4) along with the stress vector gives

$$v = \sigma_x\varepsilon_x + \sigma_y\varepsilon_y = -\hat{\sigma}(1 + \nu)\frac{-\hat{\sigma}}{E} + \hat{\sigma}(1 + \nu)\frac{\hat{\sigma}}{E} = 2(1 + \nu)\frac{\hat{\sigma}^2}{E}, \quad (\text{A.17})$$

and

$$v' = \tau_{xy}\gamma_{xy} = \frac{\hat{\sigma}^2}{G}. \quad (\text{A.18})$$

Eqs. (A.17, A.18) finally yield the formula

$$2(1 + \nu) \frac{\hat{\sigma}^2}{E} = \frac{\hat{\sigma}^2}{G}, \quad (\text{A.19})$$

$$G = \frac{E}{2(1 + \nu)}. \quad (\text{A.20})$$

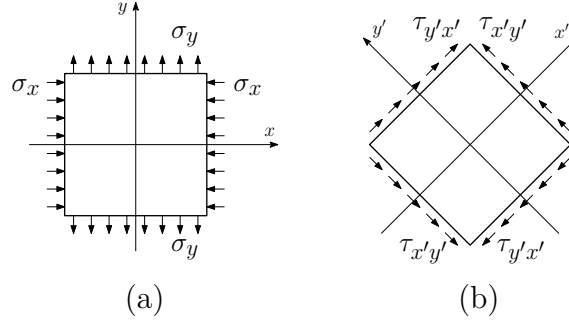


Figure A.1: Transform of principal normal stresses to maximum shear stress in order to derive shear modulus

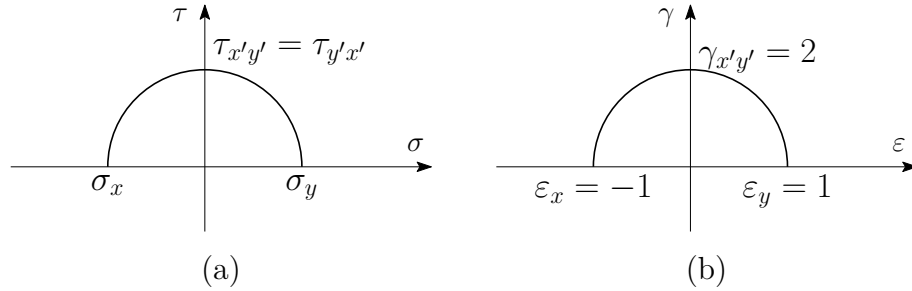


Figure A.2: Mohr's circles for (a) stress vector and (b) strain vector (due to discrepancy between tensorial and vector representation y -axis scale is twice x -axis scale)

Plane strain. For the two dimensional analysis some hypothesis regarding the stress/strain state of a material point has to be adopted. In the plane strain hypothesis all deformations realize only in the x - y plane, the out-of-plane deformations are a priori zero, i.e. ϵ_z and $\gamma_{xz} = \gamma_{yz} = 0$. This assumption is valid especially for structures such as long pipes, reservoir dams or retaining walls [50]. Introducing this assumption into Eq. (A.8) gives

$$[D] = \frac{E}{(1 - 2\nu)(1 + \nu)} \begin{bmatrix} 1 - \nu & \nu & 0 \\ \nu & 1 - \nu & 0 \\ 0 & 0 & \frac{1 - 2\nu}{2} \end{bmatrix}. \quad (\text{A.21})$$

It remains to add that, unlike the tangential out-of-plane stresses τ_{xz} and τ_{yz} , the out-of-plane normal stress σ_z is in general non-zero and can be determined as

$$\sigma_z = \frac{2E\nu}{(1-2\nu)(1+\nu)}(\varepsilon_x + \varepsilon_y). \quad (\text{A.22})$$

The eigenvalues, expressed in terms of E , ν , K and G , and the eigenvectors of the latter matrix are

$$\begin{aligned} \lambda^1 &= -\frac{E}{2\nu^2 + \nu - 1} = 2\left(\frac{G}{3} + K\right), & \{v^1\} &= \{1 \ 1 \ 0\}^T, \\ \lambda^2 &= \frac{E}{\nu + 1} = 2G, & \{v^2\} &= \{-1 \ 1 \ 0\}^T, \\ \lambda^3 &= \frac{E}{2(\nu + 1)} = G, & \{v^3\} &= \{0 \ 0 \ 1\}^T. \end{aligned} \quad (\text{A.23})$$

Plane stress. Conversely, the plane stress hypothesis presumes that only the in-plane stresses are non-zero. That is $\sigma_z = 0$ and $\tau_{xz} = \tau_{yz} = 0$. Adopting these assumptions in Eq. (A.6) and inverting the relation yields

$$[\mathbf{D}] = \frac{E}{1-\nu^2} \begin{bmatrix} 1 & \nu & 0 \\ \nu & 1 & 0 \\ 0 & 0 & \frac{1-\nu}{2} \end{bmatrix}. \quad (\text{A.24})$$

The spectral analysis of the matrix (A.24) provides the following characteristics:

$$\begin{aligned} \lambda^1 &= \frac{E}{1-\nu} = 2\frac{9GK}{4G+3K}, & \{v^1\} &= \{1 \ 1 \ 0\}^T, \\ \lambda^2 &= \frac{E}{\nu+1} = 2G, & \{v^2\} &= \{-1 \ 1 \ 0\}^T, \\ \lambda^3 &= \frac{E}{2(\nu+1)} = G, & \{v^3\} &= \{0 \ 0 \ 1\}^T. \end{aligned} \quad (\text{A.25})$$

The remaining shear strains τ_{xz} and τ_{yz} are zero since the vanishing shear stress, the relation for the out-of-plane strain ε_z reads as

$$\varepsilon_z = -\frac{\nu}{E}(\sigma_x + \sigma_y). \quad (\text{A.26})$$

Dimensionless definition of the stiffness tensor. A general form [17] of the isotropic stiffness tensor disregarding any a priori assumptions on dimension d of the problem reads

$$\mathbf{D} = dK^{(d)}\mathbf{I}_V^{(d)} + 2G^{(d)}\mathbf{I}_D^{(d)}. \quad (\text{A.27})$$

This formulation requires the dimension dependant elastic parameters $K^{(d)}$ and $G^{(d)}$ and the projection tensors

$$\mathbf{I}_V^{(d)} = \frac{1}{d} \mathbf{1} \otimes \mathbf{1}, \quad (\text{A.28})$$

$$\mathbf{I}_D^{(d)} = \mathbf{I}_S - \mathbf{I}_V^{(d)}. \quad (\text{A.29})$$

The relation between the two-dimensional and three-dimensional elastic parameters can be with advantage read from the spectral analysis. For the two dimensional case $d = 2$, regardless the plane strain or plane stress assumption, the general stiffness tensor in matrix form reads as

$$[\mathbf{D}] = \begin{bmatrix} K^{(2)} + G^{(2)} & K^{(2)} - G^{(2)} & 0 \\ K^{(2)} - G^{(2)} & K^{(2)} + G^{(2)} & 0 \\ 0 & 0 & G^{(2)} \end{bmatrix} \quad (\text{A.30})$$

and the connected spectral parameters are

$$\begin{aligned} \lambda^1 &= 2K^{(2)}, & \{v^1\} &= \{1 \ 1 \ 0\}^T, \\ \lambda^2 &= 2G^{(2)}, & \{v^2\} &= \{-1 \ 1 \ 0\}^T, \\ \lambda^3 &= G^{(2)}, & \{v^3\} &= \{0 \ 0 \ 1\}^T. \end{aligned} \quad (\text{A.31})$$

Comparing (A.31) either with (A.23) for the plane strain or with (A.25) for the plane stress assumptions directly yields the relationship between the parameters. For the plane strain case it gives

$$K^{(2)} = \frac{G}{3} + K, \quad G^{(2)} = G, \quad (\text{A.32})$$

while for the plane stress state the following formulae hold

$$K^{(2)} = \frac{9GK}{4G + 3K}, \quad G^{(2)} = G. \quad (\text{A.33})$$

Correspondingly, the dimension-dependant definition of the Young's modulus and the Poison's ratio can be found in [17].

Bibliography

- [1] M. Šejnoha, J. Zeman, Micromechanical analysis of random composites 6 (1).
- [2] D. Fullwood, S. Niezgodá, B. Adams, S. Kalidindi, Microstructure sensitive design for performance optimization, *Progress in Materials Science* 55 (6) (2010) 477–562.
- [3] J. T. Oden, T. Belytschko, J. Fish, T. J. R. Hughes, C. Johnson, D. Keyes, A. Laub, L. Petzold, D. Srolovitz, S. Yip, Simulation-based engineering science: Revolutionizing engineering science through simulation, Report of the National Science Foundation blue ribbon panel on simulation-based engineering science, National Science Foundation, Arlington, VA, 2006, [online, accessed on 5th September 2013, available at http://www.nsf.gov/pubs/reports/sbes_final_report.pdf].
- [4] The Nobel Prize in Chemistry 2013 - Advanced Informations, Nobelprize.org, Nobel Media AB 2013, 2013, [online; accessed on 16th October 2013, available at http://www.nobelprize.org/nobel_prizes/chemistry/laureates/2013/advanced.html].
- [5] The Nobel Prize in Chemistry 2013 - Popular Informations, Nobelprize.org, Nobel Media AB 2013, 2013, [online, accessed on 16th October 2013, available at http://www.nobelprize.org/nobel_prizes/chemistry/laureates/2013/popular.html].
- [6] J. Zeman, Analysis of composite materials with random microstructure, *CTU Reports* 7 (5), 177 pp.
- [7] J. Novák, A. Kučerová, J. Zeman, Compressing random microstructures via stochastic wang tilings, *Physical Review E* 86 (4) (2012) 040104.
- [8] J. Novák, A. Kučerová, J. Zeman, Microstructural enrichment functions based on stochastic Wang tilings, *Modelling and Simulation in Materials Science and Engineering* 21 (2) (2013) 025014. doi:10.1088/0965-0393/21/2/025014.
- [9] M. Cohen, J. Shade, S. Hiller, O. Deussen, Wang tiles for image and texture generation, *ACM Transactions on Graphics* 22 (3) (2003) 287–294.
- [10] P. Somol, M. Haindl, Novel path search algorithm for image stitching and advanced texture tiling, in: *WSCG'2005 Full Papers Conference Proceedings*, Science Press, UNION Agency, Plzeň, 2005, pp. 155–162.

-
- [11] A. Efros, W. Freeman, Image quilting for texture synthesis and transfer, Proceedings of the 28th annual conference on Computer graphics and interactive techniques (2001) 341–346.
- [12] I. Gitman, H. Askes, L. Sluys, Representative volume: existence and size determination, Engineering Fracture Mechanics 74 (16) (2007) 2518–2534.
- [13] T. Kanit, S. Forest, I. Galliet, V. Mounoury, D. Jeulin, Determination of the size of the representative volume element for random composites: statistical and numerical approach, International Journal of Solids and Structures 40 (13) (2003) 3647–3679.
- [14] J. Dirrenberger, S. Forest, D. Jeulin, Towards gigantic rve sizes for 3d stochastic fibrous networks, International Journal of Solids and Structures 51 (2) (2014) 359–376.
- [15] S. R. Niezgoda, D. M. Turner, D. T. Fullwood, S. R. Kalidindi, Optimized structure based representative volume element sets reflecting the ensemble-averaged 2-point statistics, Acta Materialia 58 (13) (2010) 4432–4445.
- [16] S. Torquato, J. Beasley, Y. Chiew, Two-point cluster function for continuum percolation, The Journal of chemical physics 88 (1988) 6540.
- [17] S. Torquato, Random heterogeneous materials: microstructure and macroscopic properties, Vol. 16 of Interdisciplinary Applied Mathematics, Springer, 2001, 703 pp.
- [18] Y. Jiao, F. Stillinger, S. Torquato, A superior descriptor of random textures and its predictive capacity, Proceedings of the National Academy of Sciences 106 (42) (2009) 17634–17639.
- [19] A. Sufian, A. R. Russell, Microstructural pore changes and energy dissipation in Gosford sandstone during pre-failure loading using X-ray CT, International Journal of Rock Mechanics and Mining Sciences 57 (5) (2012) 119–131.
- [20] O. Jiroušek, T. Doktor, D. Kytýř, P. Zlámal, T. Fíla, P. Koudelka, I. Jandajsek, D. Vavřík, X-ray and finite element analysis of deformation response of closed-cell metal foam subjected to compressive loading, Journal of Instrumentation 8 (02) (2013) C02012.
- [21] B. Lu, S. Torquato, Lineal-path function for random heterogeneous materials, Physical Review A 45 (2) (1992) 922.
- [22] J. Havelka, Efficient algorithms for evaluation of statistical descriptors, Bachelor’s Thesis, In Czech (2012).
- [23] MathWorks, Documentation Center- Image Processing Toolbox, [Online; accessed 13th December 2013, available at <http://www.mathworks.com/help/images/ref/bwconncomp.html>] (2013).

-
- [24] B. Grunbaum, G. C. Shephard, Tilings and patterns, W.H. Freeman & Company, 1986.
- [25] D. Aristoff, C. Radin, First order phase transition in a model of quasicrystals, *Journal of Physics A: Mathematical and Theoretical* 44 (25) (2011) 255001.
- [26] D. Levine, P. J. Steinhardt, Quasicrystals: a new class of ordered structures, *Physical review letters* 53 (26) (1984) 2477.
- [27] E. Winfree, F. Liu, L. A. Wenzler, N. C. Seeman, Design and self-assembly of two-dimensional dna crystals, *Nature* 394 (6693) (1998) 539–544.
- [28] H. Yan, S. H. Park, G. Finkelstein, J. H. Reif, T. H. LaBean, Dna-templated self-assembly of protein arrays and highly conductive nanowires, *Science* 301 (5641) (2003) 1882–1884.
- [29] J. Stam, Aperiodic texture mapping, European Research Consortium for Informatics and Mathematics, 1997.
- [30] D. Molho, Wang tiles and the undecidability of the domino problem, 20th Annual Hudson River Undergraduate Mathematics Conference, [Online; accessed 10th November 2013, available at http://web.williams.edu/Mathematics/sjmillier/public_html/hudson/Molho%20-%20Wang%20Tiles.pdf] (2013).
- [31] A. M. Turing, On computable numbers, with an application to the entscheidungsproblem, *Proceedings of the London mathematical society* 42 (2) (1936) 230–265.
- [32] A. M. Turing, On computable numbers, with an application to the Entscheidungsproblem: A correction, CF Hodgson & Son, 1937.
- [33] H. Wang, Games, logic and computers, *Scientific American* 213 (5) (1965) 98–106.
- [34] H. Wang, Proving theorems by pattern recognition-II, *Bell Systems Technical Journal* 40 (1) (1961) 1–42.
- [35] R. Berger, Undecidability of the domino problem, Vol. 66, *Memoirs of the American Mathematical Society*, 1966.
- [36] R. Ammann, B. Grünbaum, G. Shephard, Aperiodic tiles, *Discrete & Computational Geometry* 8 (1) (1992) 1–25.
- [37] G. H. Mealy, A method for synthesizing sequential circuits, *Bell System Technical Journal* 34 (5) (1955) 1045–1079.
- [38] K. Culik II, An aperiodic set of 13 Wang tiles, *Discrete Mathematics* 160 (1) (1996) 245–251.
- [39] K. Culik II, J. Kari, On aperiodic sets of Wang tiles, in: *Foundations of Computer Science*, Springer, 1997, pp. 153–162.

- [40] E. D. Demaine, M. L. Demaine, S. P. Fekete, M. J. Patitz, R. T. Schweller, A. Winslow, D. Woods, One tile to rule them all: Simulating any turing machine, tile assembly system, or tiling system with a single puzzle piece, arXiv preprint arXiv:1212.4756.
- [41] J. Kari, A small aperiodic set of Wang tiles, *Discrete Mathematics* 160 (1) (1996) 259–264.
- [42] S. Beatty, Problem 3173, *The American Mathematical Monthly* 33 (3) (1926) 159. doi:10.2307/2300153.
- [43] S. Beatty, A. Ostrowski, J. Hyslop, A. C. Aitken, Problem 3173, *The American Mathematical Monthly* 34 (3) (1927) 159–160. doi:10.2307/2298716.
- [44] K. Culik II, J. Kari, An aperiodic set of Wang cubes, *Journal of Universal Computer Science* 1 (10) (1995) 675–686.
- [45] A. Lu, D. S. Ebert, W. Qiao, M. Kraus, B. Mora, Volume illustration using wang cubes, *ACM Transactions on Graphics (TOG)* 26 (2) (2007) 11.
- [46] P. G. Sibley, P. Montgomery, G. E. Marai, Wang cubes for video synthesis and geometry placement, in: *ACM SIGGRAPH 2004 Posters*, ACM, 2004, p. 20.
- [47] V. Kwatra, A. Schödl, I. Essa, G. Turk, A. Bobick, Graphcut textures: image and video synthesis using graph cuts, in: *ACM Transactions on Graphics (TOG)*, Vol. 22, ACM, 2003, pp. 277–286.
- [48] M. Doškář, Geometrical modelling of heterogeneous materials based on wang tilings, Bachelor’s Thesis, In Czech (2012).
- [49] R. Hill, Elastic properties of reinforced solids: some theoretical principles, *Journal of the Mechanics and Physics of Solids* 11 (5) (1963) 357–372.
- [50] Z. Bittnar, J. Šejnoha, *Numerické metody mechaniky 1*, ČVUT, 1992.
- [51] J. C. Michel, H. Moulinec, P. Suquet, Effective properties of composite materials with periodic microstructure: a computational approach, *Computer methods in applied mechanics and engineering* 172 (1) (1999) 109–143.
- [52] H. P. Gavin, Structural element stiffness matrices and mass matrices, lecture notes, [Online; accessed 4th December 2013, available at <http://people.duke.edu/~hpgavin/cee541/StructuralElements.pdf>] (2012).
- [53] M. Brdička, L. Samek, B. Sopko, *Mechanika kontinua*, Academia, Praha, 2005, 799 pp.
- [54] J.-F. Despois, R. Mueller, A. Mortensen, Uniaxial deformation of microcellular metals, *Acta materialia* 54 (16) (2006) 4129–4142.
- [55] J. Banhart, Manufacture, characterisation and application of cellular metals and metal foams, *Progress in materials Science* 46 (6) (2001) 559–632.

-
- [56] M. F. Ashby, A. Evans, N. A. Fleck, L. J. Gibson, J. W. Hutchinson, H. N. Wadley, *Metal foams: a design guide*, Butterworth-Heinemann, Oxford, UK, 2000, 251 pp.
- [57] L. J. Gibson, M. Ashby, The mechanics of three-dimensional cellular materials, *Proceedings of the Royal Society of London. A. Mathematical and Physical Sciences* 382 (1782) (1982) 43–59.
- [58] P. Koudelka, P. Zlámal, D. Kytýř, T. Doktor, T. Fíla, O. Jiroušek, On the modeling of the compressive behaviour of metal foams: A comparison of discretization schemes, in: B. H. V. Topping, P. Iványi (Eds.), *Proceedings of the Fourteenth International Conference on Civil, Structural and Environmental Engineering Computing*, Civil-Comp Press, Stirlingshire, United Kingdom, 2013, paper 106.
- [59] J. Němeček, V. Králík, J. Vondřejc, A two-scale micromechanical model for aluminium foam based on results from nanoindentation, *Computers & Structures* 128 (2013) 136–145.
- [60] T. Miyoshi, M. Itoh, S. Akiyama, A. Kitahara, Alporas aluminum foam: Production process, properties, and applications, *Advanced Engineering Materials* 2 (4) (2000) 179–183. doi:10.1002/(SICI)1527-2648(200004)2:4<179::AID-ADEM179>3.0.CO;2-G.
- [61] C. Huet, Application of variational concepts to size effects in elastic heterogeneous bodies, *Journal of the Mechanics and Physics of Solids* 38 (6) (1990) 813–841.

List of Symbols

| | |
|------------------------------|--|
| $\bar{\cdot}$ | Ensemble average |
| $\langle \cdot \rangle$ | Spatial average |
| α | Realisation in ensemble |
| \mathcal{D}_i | Domain occupied with i-th phase |
| Ω | Computational domain |
| Γ | Domain boundary |
| $ \cdot $ | Measure |
| $\chi(\mathbf{x})$ | Characteristic function |
| $S_2(\mathbf{x})$ | Two-point probability function |
| $C_2(\mathbf{x})$ | Two-point cluster function |
| $L_2(\mathbf{x})$ | Lineal path function |
| $A(\cdot)$ | Beatty sequence |
| $B(\cdot)$ | Balanced representation |
| M_q | Meally machine performing multiplication by q |
| $Wn^t/n_1^c - n_2^c$ | Stochastic set of Wang tiles with n^t tiles and n_i^c edge codes |
| $Wn^t/n_1^c - n_2^c - n_3^c$ | Stochastic set of Wang cubes with n^t cubes and n_i^c face codes |
| $\lfloor \cdot \rfloor$ | Round towards the nearest smaller integer |
| $\lceil \cdot \rceil$ | Round towards the nearest larger integer |
| $e(i, j)$ | Pixel value error |
| $E(i, j)$ | Cummulative error |
| \hat{S}_2 | Secondary extreme in the $S_2(\mathbf{x})$ statistic |
| \hat{S}_2^P | Predicted value of secondary extremes in the $S_2(\mathbf{x})$ statistic |
| $\widehat{C}_2(\mathbf{x})$ | Normalized variant of the two-point cluster function $S_2(\mathbf{x})$ |
| $E^{\widehat{C}_2}$ | Error in the $\widehat{C}_2(\mathbf{x})$ statistic |
| E^ϕ | Error in the volume fraction ϕ |
| h | Length of microstructure sample edge |
| h_o | Optimal length of microstructure sample edge |
| h_p | Length of microstructure patch sample edge |
| l | Length of edge of tile |
| l_o | Optimal length of edge of tile |
| p | Width of overlap region |
| p_o | Optimal width of overlap region |
| a | Scalar |
| \mathbf{a} | First-order tensor a_i |
| \mathbf{A} | Second-order tensor A_{ij} |
| \mathbf{A} | Fourth-order tensor A_{ijkl} |

| | |
|--------------------------------|---|
| \mathbf{A} | Tensorial or matrix representation of tensor |
| \mathbf{I}_S | Symmetric projection tensor |
| \mathbf{I}_V | Volumetric projection tensor |
| \mathbf{I}_D | Deviatoric projection tensor |
| δ_{ij} | Kronecker's delta |
| ∇^s | Symmetric part of gradient |
| \cdot | Symbol of single contraction |
| $:$ | Symbol of double contraction |
| \mathbf{x} | Position tensor |
| \mathbf{u} | Displacement tensor |
| \mathbf{u}^* | Fluctuation part of displacement tensor |
| $\boldsymbol{\varepsilon}$ | Strain tensor |
| $\boldsymbol{\varepsilon}^*$ | Fluctuation part of strain tensor |
| ε_V | Volumetric strain |
| $\boldsymbol{\varepsilon}_D$ | Deviatoric strain tensor |
| \mathbf{E} | Macroscopic strain tensor |
| $\boldsymbol{\sigma}$ | Stress tensor |
| σ_m | Means stress |
| $\boldsymbol{\sigma}_D$ | Deviatoric stress tensor |
| $\boldsymbol{\Sigma}$ | Macroscopic stress tensor |
| $\mathbf{D}(\mathbf{x})$ | Elastic stiffness tensor |
| \mathbf{D}_{hom} | Homogenized stiffness tensor |
| K | Bulk modulus |
| G | Shear modulus |
| E | Young's modulus |
| ν | Poisson's ratio |
| Υ | Elastic strain energy |
| v | Elastic strain energy density |
| A | Area of cross-section |
| I | Moment of inertia of cross-section |
| L | Length of beam |
| H | Height of cross-section |
| \mathbf{K}_e^ℓ | Local stiffness matrix of element |
| \mathbf{K} | Global stiffness matrix |
| \mathbf{K}^{ex} | Extended global stiffness matrix |
| \mathbf{r} | Vector of unknowns in Direct stiffness method |
| \mathbf{r}^* | Vector of unknowns related to fluctuational part |
| \mathbf{I} | Identity matrix |
| \mathbf{A} | Matrix coupling nodal DOFs with macroscopic deformation |
| $\{\boldsymbol{\varepsilon}\}$ | Strain vector in Voigt notation |
| ε_a | Normal strain parallel with a axis |
| γ_{ab} | Shear deformation in a - b plane |
| $\{\boldsymbol{\sigma}\}$ | Stress vector in Voigt notation |
| σ_a | Normal stress parallel with a axis |
| τ_{ab} | Shear stress in a - b plane |

List of Figures

| | | |
|------|--|----|
| 1.1 | Visualization of raw CT-scan data and corresponding $S_2(\mathbf{x})$ statistics | 6 |
| 1.2 | Reference microstructures | 9 |
| 1.3 | Spatial statistics of the reference microstructures | 9 |
| 1.4 | Matlab GUI program for spatial statistics computations | 10 |
| 1.5 | Comparison of $S_2(\mathbf{x})$ and $C_2(\mathbf{x})$ graphs | 11 |
| 2.1 | Illustration of Mealy machine transition and Wang tile | 16 |
| 2.2 | Illustration of Kari's set of 14 tiles | 17 |
| 2.3 | Illustration of Culik's set of 13 tiles | 18 |
| 2.4 | Stochastic Wang tile nomenclature | 19 |
| 2.5 | Stochastic tiling algorithm | 20 |
| 2.6 | Stochastic Wang cube nomenclature | 21 |
| 2.7 | Example of Wang cubes set and spatial tiling | 22 |
| 3.1 | Automatic tile design | 24 |
| 3.2 | Example of Automatic tile design outputs | 25 |
| 3.3 | Effect of modified Quilting algorithm | 26 |
| 3.4 | Comparison of image fusion algorithms | 27 |
| 3.5 | Tile patching procedure | 28 |
| 3.6 | Comparison of secondary extremes with prediction | 29 |
| 3.7 | Reference microstructures for sensitivity analysis | 30 |
| 3.8 | Scheme of input variables | 31 |
| 3.9 | Overlap error | 32 |
| 3.10 | Probability of Labyrinth algorithm success | 32 |
| 3.11 | Deviation of inclusion phase volume fraction | 33 |
| 3.12 | Overlap shape error | 35 |
| 3.13 | Relative error of inclusion phase volume fraction | 36 |
| 3.14 | Comparison of secondary extremes \widehat{S}_2 with prediction | 37 |
| 3.15 | Shape error | 37 |
| 3.16 | Examples of reconstructed microstructures | 38 |
| 5.1 | Compressed Alporas [®] microstructure | 55 |
| 5.2 | Illustration of domain generation | 57 |
| 5.3 | In-house designed tool to aid manual meshing of Wang tiles | 57 |
| 5.4 | Comparison of geometrical representation with reference microstructure | 58 |
| 5.5 | Support search algorithm | 59 |

| | | |
|-----|--|----|
| 5.6 | Relationship between homogenized elastic parameters and dimensions of computational domains | 60 |
| A.1 | Derivation of shear modulus | d |
| A.2 | Mohr's circle | d |

List of Tables

| | | |
|-----|--|----|
| 1.1 | Relation among two-point correlation function for binary media . . . | 5 |
| 3.1 | Morphometrics of Target Systems | 31 |
| 3.2 | Optimal values of overlap width p and tile dimension l | 34 |
| 5.1 | Properties of Alporas [®] foam | 54 |
| 5.2 | Beam cross-section characteristics | 58 |
| 5.3 | Homogenization results | 61 |

List of Algorithms

| | | |
|-----|------------------------------------|----|
| 1.1 | Flood-fill algorithm | 10 |
| 3.1 | Image Quilting algorithm | 25 |